Preprints are preliminary reports that have not undergone peer review.
They should not be considered conclusive, used to inform clinical practice,
or referenced by the media as validated information.

Immune phenotypes that predict COVID-19 severity

Thomas Liechti
National Institutes of Health https://orcid.org/0000-0001-8738-6679
Yaser Iftikhar
National Institutes of Health
Massimo Mangino
King's College London https://orcid.org/0000-0002-2167-7470
Margaret Beddall
National Institutes of Health
Charles Goss
Washington University in St.Louis
Jane O'Halloran
Washington University School of Medicine https://orcid.org/0000-0001-8265-9471
Philip Mudd
Washington University School of Medicine https://orcid.org/0000-0002-3860-5473
Mario Roederer (marior@mail.nih.gov)
National Institutes of Health

Article

Keywords: SARS-CoV2, COVID-19, Immunophenotyping, Chemokine Receptors, High-dimensional flow cytometry

Posted Date: March 10th, 2022

DOI: https://doi.org/10.21203/rs.3.rs-1378671/v1

License: This work is licensed under a Creative Commons Attribution 4.0 International License.
Read Full License

Title: Immune phenotypes that predict COVID-19 severity

Thomas Liechti[1], Yaser Iftikhar[1], Massimo Mangino[2,3], Margaret Beddall[1], Charles W. Goss[4], Jane A. O'Halloran[5], Philip Mudd[6], Mario Roederer[1]

[1]ImmunoTechnology Section, Vaccine Research Center, NIAID, NIH, USA, 20892
[2]Department of Twin Research & Genetic Epidemiology, King's College of London, London, UK
[3] NIHR Biomedical Research Centre at Guy's and St Thomas' Foundation Trust, London SE1 9RT, UK
[4]Division of Biostatistics, Washington University School of Medicine, St. Louis, MO, USA,
[5]Division of Infectious Diseases, Department of Internal Medicine, Washington University School of Medicine, St. Louis, MO, USA
[6]Department of Emergency Medicine, Washington University School of Medicine, St. Louis, MO, USA, 63110

Keywords

SARS-CoV2, COVID-19, Immunophenotyping, Chemokine Receptors, High-dimensional flow cytometry

Abstract

Severe COVID-19 causes profound immune perturbations, but pre-infection immune signatures contributing to severe COVID-19 remain unknown. Genome-wide association studies (GWAS) identified strong associations between severe disease and several chemokine receptors and molecules from the type I interferon pathway. Here, we define immune signatures associated with severe COVID-19 using high-dimensional flow cytometry. We measured the peripheral immune system from individuals who recovered from mild, moderate, severe or critical COVID-19 and focused only on those immune signatures returning to steady-state. Individuals that suffered from severe COVID-19 showed reduced frequencies of T cell, MAIT cell and dendritic cell (DCs) subsets and altered chemokine receptor expression on several subsets, such as reduced levels of CCR1 and CCR2 on monocyte subsets. Furthermore, we found reduced frequencies of type I interferon-producing plasmacytoid DCs and altered IFNAR2 expression on several myeloid cells in individuals recovered from severe COVID-19. Thus, these data identify potential immune mechanisms contributing to severe COVID-19.

Introduction

The recent COVID-19 pandemic caused an unprecedented global health crisis. Demographic and socioeconomical factors affect disease severity and mortality (*1*). Underlying health conditions such obesity and diabetes or gender with higher risk for males have been associated with disease severity (*1*). Additionally, genetic predisposition contributes to the development of severe COVID-19 (*2, 3*). GWAS identified several genes encoding for pro-inflammatory chemokine receptors and molecules from the type I interferon pathway, such as OAS1, DPP9, TYK2 and IFNAR2, that associate with the development of severe COVID-19 (*2, 3*). Thus, tissue distribution of immune cells and the responsiveness of innate immunity to infection may be key factors to prevent severe outcome in COVID-19. While GWAS enable the identification of associations between genetic variants and disease severity, such studies fall short of providing insights into the mechanisms by which these genetic traits manifest disease susceptibility. Nearly all of the SNPs identified in GWAS are regulatory and not coding in nature; the altered regulation could be expressed on subsets of immune cells rather than organism-wide. Thus, immunological studies such as immunophenotyping at the single cell level are necessary to gain mechanistic understanding of how genetics affect immune responses (*4*).

Chemokine receptors are crucial in regulating leukocyte trafficking and thereby orchestrating immune responses (*5, 6*). Thus, chemokine receptors are critical in all aspects of immune responses including adaptive immunity in lymphoid organs (*6*), early influx of innate immune cells (*7*) and migration of cells in inflamed tissues (*8*). Their expression is tightly regulated and depends on the immune milieu (*5*). Imbalance or perturbations in the homeostasis of chemokine and chemokine receptor expression are associated with inflammatory and autoimmune diseases (*8*).

The innate immune system ensures rapid and effective immune responses against viruses and is impaired in severe COVID-19 (*9-11*). IFNAR2 is critical for type I interferon mediated immunity; homozygous mutations, which abrogate IFNAR2 expression, are associated with fatal outcome in viral infections (*12*). The role of type 1 interferon remains controversial in SARS-CoV2 (*13*). Severe COVID-19 is associated with low serum levels of type I interferon (*14*). In contrast, robust type I interferon response occurs in lung tissues from severe but not mild COVID-19 cases (*15*). Furthermore, neutralizing autoantibodies against type I interferon (*16*) or loss-of-function mutations in type I interferon pathway (*17*) occur more frequently within severe COVID-19 cases. Thus, while excessive type I interferon response may exacerbate inflammation and severity of COVID-19, it is likely that the lack thereof is also detrimental.

Based on the GWAS data (*2, 3*) we hypothesized that immune signatures at steady-state (i.e. prior to infection and following recovery) impact the outcome of COVID-19 severity. This may manifest as a variety of phenotypes: altered level of expression or altered regulation of certain subsets of immune cells. Here we tested this hypothesis using high-dimensional, comprehensive immunophenotyping in peripheral blood mononuclear cells (PBMC) of individuals that recovered or substantially improved from mild, moderate, severe and critical COVID-19 (Extended Data Figs. 1-2). Particularly, we focused on the expression of chemokine receptors and IFNAR2 identified by GWAS (*2, 3*). We identified several immune signatures at steady-state which differed between individuals recovered from non-severe and severe COVID-19. This included altered expression of various chemokine receptors on NK and MAIT cells as well as altered abundance of innate immune subsets. In addition, our data revealed reduced levels of type I interferon producing pDCs (*18*) and increased expression of IFNAR2 on several myeloid cell subsets at steady-state in individuals recovered from severe COVID-19, pointing towards impaired type I interferon responsiveness. Thus, these data define predictable immune signatures associated with severe COVID-19 outcome and improve our understanding of pathogenesis of COVID-19.

Results

Expression profile of chemokine receptors, IFNAR2 and functional receptors

We assessed the immune profile in PBMC from 173 healthy individuals using 28-color flow cytometry (Fig. 1a and Supplementary Tables 1-2). We measured immune cell subsets with two backbone panels focusing on either B cells and myeloid cells or innate-like and conventional T cells as well as NK cells (referred to as BDC and TNK panels, respectively; Table S1). We used each backbone panel with two sets of chemokine receptors (CR1 and CR2). Thus, for each sample, we measured a total of 4 unique sets of markers. Manual definition of immune subsets and functional marker expression profile on these subsets are shown in supplementary material (Supplementary Data 2-7).

Immune subsets showed heterogenous expression of various chemokine receptors, the Ecto-NTPDase CD39, co-stimulatory receptors CD40 and CD86, Interferon-alpha receptor 2 (IFNAR2) and co-inhibitory molecule TIGIT (Fig. 1a). We focused our subsequent analysis on immune traits for which the lineage showed discernible expression. For instance, XCR1 and CCR3 were only expressed on cDC1s and Basophils, respectively, while B cells did not express CCR1, CCR2, CCR3, CCR4, CCR8, CXCR6 and CX3CR1. The remaining 1758 out of 3787 immune traits consisted of frequency of immune cell subsets (N = 349), cells expressing functional markers (N = 620) or the mean fluorescence intensity (MFI; N = 789) of functional markers.

Prolonged immune perturbations after recovery from COVID-19

We aimed to identify immune signatures at steady-state which contribute to severe COVID-19. However, cohorts with baseline PBMC samples from patients who had not yet been infected with COVID-19 are not available. Thus, we looked for traits post-recovery and selected those traits for analysis which might be most informative based on GWAS. COVID-19 induced immune perturbations can persist after viral clearance and recovery (*19, 20*). We hypothesized that immune cells could experience different fates during acute COVID-19 including i) not affected and remaining at baseline, ii) affected and deviating from healthy individuals only during active viral disease or iii) persistently affected even after viral clearance. The latter results in delayed normalization back to baseline levels. We first aimed to identify these persisting immune perturbations which may contribute to long-lasting COVID19-related symptoms known as long COVID (*19*). To this end, we analyzed PBMC collected after recovery from mild, moderate, severe and critical COVID-19 (Extended Data Fig. 1 and 2). We focused on the moderate and severe COVID-19 group as these groups showed the largest time range between symptom onset and sample collection (Extended Data Fig. 1a; Moderate, 24-129 days; Severe, 16-184 days). We applied two strategies to identify persistently affected immune traits. These included i) linear regression of immune traits and time between symptom onset and sample collection, and ii) comparison of samples collected before and after 60 days of symptom onset using a Wilcoxon test. We opted to abstain from multiple testing correction in order to avoid the inclusion of marginally significant true positive immune traits (i.e. immune traits which truly change over time) in our analysis of stable immune traits. The two strategies showed similar results (Fig. 1b). We assessed the top hits from both analyses ($p<0.001$ in at least one analysis, $N = 24$) to further delineate persistent immune perturbations in COVID-19 (Fig. 2a).

The most prominent persisting perturbations occurred within switched (containing memory B cells and plasmablasts) and memory $CD20^{+}IgD^{-}CD38^{-/+}CD27^{-/+}$ B cells (Fig. 2a). Switched and naïve B cells did not change in moderate COVID-19 over time but significantly decreased and increased, respectively, in severe cases (Spearman's rank correlation; Naïve: $R^2 = 0.36$, $P = 0.002$; Switched: $R^2 = 0.44$, $P = 4*10^{-4}$) to levels observed in healthy individuals (Fig. 2b). Both naïve and switched B cells did not differ between study groups (Fig. 2b). Similar dynamics occurred for $CD38^{+}HLA\text{-}DR^{-}$ and $CD38^{-}HLA\text{-}DR^{-}$ CD4 naïve T cells which showed an increase and decrease, respectively, over time in the severe COVID-19 group (Spearman's rank correlation; $CD38^{+}HLA\text{-}DR^{-}$ CD4 naïve: $R^2 = 0.42$, $P = 5.8*10^{-4}$; $CD38^{-}HLA\text{-}DR^{-}$ CD4 naïve: $R^2 = 0.42$, $P < 6.5*10^{-4}$) with later timepoints reaching levels observed in healthy individuals (Fig. 2c). In addition, decreased $CD38^{+}HLA\text{-}DR^{-}$ and increased $CD38^{-}HLA\text{-}DR^{-}$ CD4 naïve T cells occurred in individuals recovered from severe and critical COVID-19 (Bonferroni-adjusted P-value range $0.02 – 1.46*10^{-4}$) (Fig. 2c).

Cross-presenting cDC1s induce potent CD8 T cell responses. Timepoints early after onset of symptoms had reduced levels of cDC1s in severe COVID-19 cases, but these increased later to levels observed in healthy individuals, suggesting perturbations of cDC1s during active COVID-19 (Spearman's rank correlation; $R^2 = 0.29$, $P = 0.0069$) (Fig. 2d). We also observed changes in the expression levels of receptors over time (Figs. 2a, e and f). Basophils expressed reduced levels of CCR3 early after symptom onset while levels were closer to healthy individuals at later timepoints within the severe COVID-19 group (Spearman's rank correlation; $R^2 = 0.46$, $P = 2.8*10^{-4}$) (Fig. 2e). CCR3 expression was reduced in basophils from severe and critical COVID-19 cases (Bonferroni-adjusted P-value range $0.01 – 2.11*10^{-7}$). Furthermore, CD95 expression decreased over time in early NK (Spearman's rank correlation; $R^2 = 0.26$, $P = 0.011$) and NK2 cells (Spearman's rank correlation; $R^2 = 0.37$, $P = 0.002$) in severe COVID-19 (Fig. 2f). CD95 expression was significantly elevated in both subsets from critical COVID-19 compared to all other groups (Bonferroni-adjusted P-value range $0.00965 – 1.43*10^{-7}$). In conclusion several immune traits in severe COVID-19 required prolonged time - up to 100 days after symptom onset - to reach baseline levels which can be several months which agrees with previous studies (*19, 20*).

Predictive potential of lymphocyte immune traits

Next, we hypothesized that stable immune traits (N = 1365) between symptom onset and sample collection remained at or returned early to pre-infection baseline. We aimed to identify differences in these traits between individuals recovered from mild (N = 19) and moderate (N = 24) COVID-19 (combined and referred to as non-severe group, N = 43) and severe (N = 25) and critical (N = 30) COVID-19 cases (combined and referred to as severe group, N = 55). Such differences may give clues about pre-infection immune signatures which favor the development of severe COVID-19. We identified distinctive immune features between these two groups using logistic regression (N = 150, FDR-adjusted P-value cut-off < 0.01) as described in the Online methods (Extended Data Fig. 3). Despite substantial improvement, some patients from the severe (N = 6) and critical (N = 21) COVID-19 group were still hospitalized at sample collection (Extended Data Figs. 1d and e). These samples may bias the analysis due to persistent immune perturbations or pathologies; we therefore repeated the analysis and only included individuals which were discharged prior to or at the day of sample collection (Extended Data Figs. 4a and b). We obtained similar results with this smaller sample set (Non-severe, N = 43; Severe, N = 28, FDR-adjusted P-value cut-off < 0.012), compared to all individuals, with highly correlated P-values between both analyses (Spearman's rank correlation, R = 0.88, $P < 2*10^{-16}$) (Extended Data Fig. 4c). In fact, 65 significant hits (FDR-adjusted $P_{ALL} < 0.01$, FDR-adjusted $P_{Non\text{-}hospitalized} < 0.012$) were shared between these two analyses using either all patients or only non-hospitalized patients at the time of sample collection (Extended Data Fig. 4d). Only 6 new immune traits were discovered with the non-hospitalized sample set (FDR-adjusted P < 0.012). However, 85 significant immune traits (FDR-adjusted P < 0.0017) were only discovered when all patients were analyzed. This may be due to the lower statistical power with the smaller sample set as suggested by the strong correlation of P-values (Extended Data Fig. 4c).

We primarily focused our analysis on traits which significantly differed between non-severe and severe COVID-19 cases in both sample sets (all vs. non-hospitalized, N = 65, FDR-adjusted $P_{ALL} < 0.01$, FDR-adjusted $P_{Non\text{-}hospitalized} < 0.012$) (Extended Data Figs. 3b and 4b). NK cells are critical for antiviral defense (*21*) and impaired in severe COVID-19 (*22*). We discovered several chemokine receptor signatures on NK cells (N = 8) associated with the development of severe COVID-19, including up-regulated CX3CR1 expression on early NK cells (Fig. 3a) and increased levels of CCR4, CCR9 and CXCR3 on terminal NK cells (Fig. 3b). However, the expression of these molecules by other cell types were not associated with severity, underscoring the need to perform multiparameter analysis at the single cell level.

We also identified several potentially predictive traits (N = 75) within conventional T cells. Naïve and transitional memory (TM) $CD8^+$ T cells from individuals suffered from severe and critical COVID-19 expressed higher levels of CCR4 (Bonferroni-adjusted P-value range 0.03 - $7*10^{-5}$). This pattern did not occur on naïve and TM $CD4^+$ T cells (Fig. 3c). Furthermore, stem cell-like memory (TSCM), central memory (CM) and terminal effector* (TE*) $CD8^+$ T cells exhibited reduced TIGIT expression in individuals recovered from severe and critical COVID-19 (Bonferroni-adjusted P-value range 0.01 - $7.21*10^{-6}$) (Fig. 3d). In contrast, naïve $CD8^+$ T cells and MAIT cells expressed similar levels between study groups or elevated levels of TIGIT in individuals suffered from severe and critical COVID-19, respectively (Bonferroni-adjusted P-value range 0.04 - 0.004).

The frequency of MAIT cells was decreased in severe and critical COVID-19 (Extended Data Fig. 4e) (Bonferroni-adjusted P-value range $3.99*10^{-4}$ - $2.96*10^{-6}$). Furthermore, more individuals recovered from severe and critical COVID-19 showed reduced frequencies of central memory (CM) $CD4^+$ and $CD8^+$ T cells (defined as $CD45RA^-CCR7^+CD27^+$) (Bonferroni-adjusted P-value range 0.02 - $7.61*10^{-6}$) (Extended Data Fig. 4f). In addition, individuals recovered from critical COVID-19 had elevated levels of activated (defined as $CD38^+HLA\text{-}DR^+$) $CD8^+$ effector and terminal memory T cells (Bonferroni-adjusted P-value range $5.46*10^{-4}$ - $1.04*10^{-6}$) (Fig. 3e).

We did not identify many B cell traits predictive for COVID-19 severity. However, patients with severe COVID-19 had lower baseline frequencies of marginal zone (MZ) B cells, which produce natural IgM mostly targeting bacterial glycans and are considered an early wave of immune defense (Fig. 3f) (Bonferroni-adjusted P-value range 0.00192 - $1.84*10^{-4}$) (*23*).

Predictive potential of myeloid immune traits

Innate immune signatures determine the trajectories of disease severity early during active COVID-19 (*24*). We assessed several innate immune subsets such as monocytes and dendritic cells (DCs) in the periphery (*25, 26*) as well as several critical markers for stimulation of adaptive immune responses including CD40 and CD86. Individuals recovered from severe and critical COVID-19 had reduced frequencies of plasmacytoid DCs (pDCs) and $CD14^+$ DC3s (Bonferroni-adjusted P-value range 0.00226 - $3.71*10^{-7}$) (Fig. 4a).

The chemokine receptor profile on dendritic cells did not differ substantially between individuals recovered from non-severe and severe COVID-19. We observed increased expression of CX3CR1 on pDCs and cross-presenting cDC1s associated with disease severity (Bonferroni-adjusted P-value range 0.00301 - $1.83*10^{-5}$) (Fig. 4b). Frequency of monocyte subsets did not differ between groups. However, classical and intermediate monocytes from individuals recovered from severe COVID-19 had reduced expression of pro-inflammatory chemokine receptors CCR1 and CCR2 (Bonferroni-adjusted P-value range 0.04 – $2.07*10^{-9}$) (Fig. 4c). In contrast, non-classical pro-inflammatory monocytes showed no differences of CCR1 and CCR2 expression between COVID-19 severity groups (Fig. 4c).

Genome-wide association studies identified IFNAR2 as a risk factor for severe COVID-19 (*2, 3*). Furthermore, type I interferon response is critical for effective immune responses against COVID-19 (*10, 11, 13, 14*). We measured expression of IFNAR2 on monocytes, dendritic cells and B cells. IFNAR2 expression was lowest on naïve B cells and highest on pDCs and cDC1s, but expression could be detected on most subsets including cDC2s, DC3s and monocyte subsets (Fig. 1a). We found increased expression of IFNAR2 on monocyte and dendritic cell subsets, except for cDC1s and pDCs, in individuals recovered from severe and critical COVID-19 (Bonferroni-adjusted P-value range 0.04 - $4.95*10^{-5}$) (Figs. 4d and e). In non-myeloid cells, IFNAR2 expression was elevated in basophils but no substantial change in expression of IFNAR2 occurred in other non-myeloid cells with disease severity (Figs. 4d and e). IFNAR2 was slightly reduced in several $CD38^{low}$ memory B cell populations severe and critical COVID-19 (Fig. 4d). However, these $CD38^{low}$ memory B cell subsets were not significantly different between non-severe and severe COVID-19 group (Extended Data Fig. 3b).

Unsupervised cluster analysis

Next, we used unsupervised clustering to extend our analysis and identify potential immune signatures not revealed by our manual gating analysis. We split cells from both chemokine receptor panels into main lineages based on manual gating and defined 388 clusters using FlowSOM as described in the Online methods (Supplementary Data 8-13 and Supplementary Tables 3 and 4). Subsequently, we excluded persistently perturbed immune clusters (N = 97) as described for manually defined traits in Figure 1b (Extended

Data Fig. 5a). Next, we identified distinct immune traits between non-severe and severe COVID-19 after recovery using logistic regression (Figs. 5a and b). Results with all samples and with only the non-hospitalized individuals strongly correlated (Spearman's rank correlation, R = 0.9, P < 2.2e-16) confirming that hospitalization was not a major driver (Extended Data Figs. 5b and c).

We focused on 42 significant clusters ($p_{FDR} < 0.01$) across all lineages (Figs. 5a and b). From each chemokine receptor panel (CR1 and CR2) 5 and 6 significant clusters ($p_{FDR} < 0.01$) resembled innate-like T cells, respectively. Four clusters (clusters 34, 35, 37 and 38) from CR1 and one (cluster 3) from CR2 panel were MAIT cells as defined by T cell receptor (TCR) $V\alpha7.2$ and CD161 (Fig. 5c). These clusters were reduced in severe COVID-19 (Bonferroni-adjusted P-value range 0.04 – $3.71*10^{-7}$) (Fig. 5d) matching the overall decreased frequency of MAIT cells (Extended Data Fig. 4e). $V\delta2V\gamma9$ T cell clusters 20 and 25 from CR2 panel were expanded in severe and critical COVID-19 (Bonferroni-adjusted P-value range 0.00564 – $6.39*10^{-8}$) and characterized by CCR9, CXCR3 and TIGIT expression (Fig. 5d). In contrast $V\delta2V\gamma9$ T cell cluster 24 expressed higher levels of CCR4 and CCR8 but lacked CXCR3 and TIGIT (Fig. 5d).

Within myeloid cells, $CD123^{+}CD5^{-}$ pDCs (CR1: 24, CR2: 28) and $CD123^{+}CD5^{+}$ pre-DCs (CR1: 28, CR2: 29) were significantly reduced (Bonferroni-adjusted P-value range 0.04 – $4.11*10^{-6}$) in individuals recovered from severe and critical COVID-19. These cells were characterized by expression of CD38, CCR5 and high levels of CXCR3. CCR1, CCR2 and IFNAR2 were expressed at higher levels on pDCs while co-stimulatory CD86 was lower and CD40 expression was lacking on both. $CD14^{-}$ DC3s (CR1: 22; CR2: 21) and $CD14^{+}$ DC3s (CR1: 11) differ between individuals recovered from non-severe and severe COVID-19 (Figs. 6a and b) in agreement with our manual analysis (Fig. 4a and Extended Data Fig. 3).

We further examined myeloid cells from mild and severe COVID-19 cases using tSNE. Clusters shown in Figure 6a exhibited reduced density on the tSNE map in severe cases (Fig. 6c and Supplementary Data 9). We analyzed the relationship between the subsets identified in panels CR1 and CR2 which showed high overlap suggesting the identification of similar populations with both panels (Fig. 6d).

Overall, unsupervised analysis reveals similar immune subsets which differ between individuals recovered from non-severe and severe COVID-19 compared to the manually defined subsets. However, the unsupervised analysis enabled more detailed insights into the unique expression patterns of chemokine receptors and other functional molecules on these subsets.

Discussion

We lack mechanistic insights into how pre-infection immune signatures contribute to the development of life-threatening COVID-19. GWAS identified several genes associated with COVID-19 severity (*2, 3*). The most predictive genes encode for pro-inflammatory chemokines such as CCR2, CCR3, CXCR6 and XCR1 and molecules from the type I interferon pathway including IFNAR2 (*2, 3*). However, these GWAS associations do not indicate potential mechanisms (e.g., altered expression of CCRs on subsets of leukocytes). Thus, immunological studies such as immunophenotyping are needed to better understand the mechanisms by which these immune traits impact disease severity. In addition, most studies focused on finding distinctive immune signatures during active severe COVID-19 (*14, 15, 22, 24, 27, 28*). Here, we hypothesized that pre-infection immune signatures determine the trajectories of COVID-19 severity. Thus, we measured the immune composition using high-dimensional flow cytometry in peripheral blood of individuals recovered from mild, moderate, severe and critical COVID-19 to identify immune signatures associated with COVID-19 severity. After pathogen clearance the human immune system rapidly reverts to steady-state with a composition comparable prior to infection (*29*). Therefore, samples taken after recovery from COVID-19 reflect the immune system at steady-state and are comparable to pre-infection. Thus, our study provides potential immune mechanisms at the earliest events of COVID-19 which determine the trajectory of disease severity.

Our study identifies several distinct chemokine receptor signatures between individuals recovered from non-severe (mild/moderate) and severe (severe/critical) COVID-19. Chemokine receptors are important for protective immune responses against viral infections such as West Nile Virus and Influenza (*30, 31*) and their expression is altered in severe COVID-19 (*24, 27*). In our study, individuals recovered from severe COVID-19 had increased expression of lung-homing chemokine receptors CCR4, CXCR3 and CX3CR1 on NK cell subsets (Figs. 3a and b). These receptors result in exacerbated lung inflammation and impaired immune responses against viruses (*32-34*). In addition, NK cells can facilitate inflammation during viral infections (*35*). Thus, increased baseline expression of lung-homing chemokine receptors on NK cells may facilitate NK cell migration and exacerbate lung inflammation in COVID-19. We also identified elevated CCR4 levels on transitional memory CD4$^+$ and CD8$^+$ T cells in these individuals (Fig. 3c) highlighting that enhanced homing of T cells to the lung might exacerbate COVID-19.

In contrast, individuals recovered from mild and moderate COVID-19 expressed higher levels of TIGIT (Fig. 3d). TIGIT expression prevents immune pathologies of viral infections in mice and reduces lung damage in influenza infection (*36*). Thus, increased levels of TIGIT might play a protective role against severe lung damage and consequently the development of life-threatening COVID-19.

Furthermore, we observed reduced expression of CCR1 and CCR2 on monocyte subsets from individuals recovered from severe COVID-19 (Fig. 4c). CCR2 can play a protective role in the early phase of mouse-adapted SARS-CoV2 infection (*37*). Similarly, CCR1 and CCR2 knock-out mice exhibited exacerbated immune pathologies in SARS-CoV (*38*). These studies and our results suggest a protective role of CCR1 and CCR2 in early immune responses against coronaviruses. Both CCR1 and CCR2 interact with pro-inflammatory chemokines which are upregulated in the lungs of severe COVID-19 patients (*27*). Thus, altered expression of CCR1 and CCR2 at steady state might influence the severity of COVID-19.

Type I interferon is crucial for antiviral immune responses and orchestrates the induction of chemokines and pro-inflammatory cytokines (*10, 13*). We observed reduced levels of pDCs, the main source of type I interferon during viral infections (*18*). Thus, reduced frequencies of pDCs at baseline may contribute to the impaired or delayed type I interferon response in severe COVID-19 (*14, 15*). Similar delayed type I interferon responses occur in SARS and MERS and are associated with worse disease outcome (*39-41*). Therefore, dysregulated and delayed type I interferon response can be detrimental for the host in coronavirus infections.

On the contrary, we observed increased expression of IFNAR2 on basophils and myeloid cells but not on B cells and pDCs in individuals recovered from severe COVID-19 (Fig. 5d). This is in contradiction with inferences from a recent study which combined GWAS and bulk transcriptomics and identified reduced expression of IFNAR2 in lung and whole blood as a risk factor for severe COVID-19 (*2*). In contrast to bulk transcriptomics, we show at the single-cell level that IFNAR2 is only affected on certain blood immune cell populations in individuals recovered from severe COVID-19. Notably, we measured IFNAR2 only on B cells, basophils and myeloid cells and can therefore not determine whether its expression is downregulated in other blood cell types. The dichotomy between reduced pDC frequencies and elevated IFNAR2 expression on myeloid cells is puzzling. However, interaction between type I interferon and its receptor results in endocytosis (*42*) and it is therefore possible that constitutively expressed type I interferon might regulate IFNAR2 expression at steady-state (*43*). Nevertheless, the increased levels of IFNAR2 might potentiate the responsiveness of myeloid cells to type I interferon and thus drive exacerbated inflammation.

Most immune perturbations caused by COVID-19 disappear within 60 days post-infection, but some immune perturbations persist for weeks after viral clearance (*19, 20*). In our study, the majority of immune traits were at baseline in recovered patients (Fig. 1b). Nonetheless, we identified several immune traits which did not fully return to baseline even weeks after symptom onset (Figs. 1b and 2). Most of these long-term perturbations occurred in severe COVID-19, likely due to increased immune activation (*24*), and affected mainly B and T cells (Fig 2). The half-life of peripheral lymphocytes is longer compared to myeloid cells. Models suggest that peripheral dendritic cells and monocytes are replenished every few days (*44-46*) while turnover of memory and naïve T cells can be in the order of several weeks (*47*) and years (*48*), respectively. Thus, the prolonged immune cell half-life might interfere with the replacement of impaired lymphocytes after COVID-19 infection. Furthermore, naïve T cells are maintained by homeostatic proliferation while thymic output declines in aging (*48*) which might contribute to sustained immune perturbations.

In summary, we identified several single cell-based immune signatures associated with the development of severe COVID-19 outcome. We specifically identified components of innate immunity, NK cells and innate-like T cells which are important for the earliest events in orchestrating efficient immune responses and in the clearance of other pathogens potentially worsening the disease outcome. Our data support current clinical efforts to modulate immune cell trafficking using chemokine receptor inhibitors or administration of interferon to treat severe COVID-19 patients (*27, 49-51*).

Online Methods

Detailed information of buffers and cell culture media is listed in Supplementary Table 5 and staining reagents are listed in Supplementary Table 2.

Samples

PBMC samples from 173 healthy individuals enrolled as part of the VRC clinical trial program served as control group. Convalescent samples from individuals recovered from mild and moderate COVID-19 were collected at the NIH (Mild, N = 14; Moderate, N = 10) and Evergreen in Washington State (Mild, N = 5; Moderate, N = 14). In addition, PBMCs from individuals recovered from severe (N = 25) and critical (N = 30) COVID-19 were obtained from Washington University. Distinction between severe and critical cases was based on required ventilation. All individuals from the mild and moderate group resolved symptoms by the time of sample collection while all individuals from the severe and critical groups showed at least substantial improvement of symptoms. Information about time between symptom onset and sample collection was unavailable for two samples from the mild COVID-19 group. Detailed demographics are shown in Extended Data Figs. 1 and 2. Informed consent was obtained from individuals in compliance with IRB procedures. Peripheral blood mononuclear cells (PBMCs) were purified using density gradient centrifugation and cryopreserved in 10% DMSO in liquid nitrogen.

Flow cytometry

Staining reagent cocktails were prepared in staining buffer (RPMI without phenol red and 4% HINCS) containing Brilliant Buffer Plus (1:5 diluted) and TrueStain Monocyte Blocker (5μl/100μl). Antibody cocktails were tested on irrelevant PBMC sample to validate completeness prior to sample processing. After successful validation of staining reagent cocktails, PBMCs were thawed in RPMI containing 10% fetal bovine serum, 100 IU/ml Penicillin, 100μg/ml Streptomycin and 292μg/ml L-Glutamine (referred to as R10) containing 50U/ml Benzonase using a tube adaptor to facilitate and standardize the thawing process as described (*52*). Cells were washed once with 5ml R10 and transferred to a V-bottom, 96-well plate (Corning). After two washes with 200μl PBS, cells were stained in 100μl fixable Live/Dead Blue viability dye containing human BD Fc receptor block (5μl/100μl) for 20 minutes at room temperature protected from light. Afterwards, cells were distributed into two 96-V bottom plates and stained with 50μl of either B cell/myeloid cell (BDC) or T cell/NK cell (TNK) backbone staining mix for 30 minutes at room temperature. Samples were subsequently distributed into two wells and stained with either chemokine receptor panel 1 (CR1) or 2 (CR2) for 30 minutes at room temperature. Subsequently, we washed cells three times with 250ul staining buffer followed by fixation with 0.5% paraformaldehyde in PBS overnight at 4C. Cells were acquired the next day with a FACSymphony (BD Biosciences) cytometer. Detailed instrument configuration is described elsewhere (*53*). Initial centrifugation for thawing was performed at 700g for 5min and all subsequent centrifugation steps were done at 860g for 3min.

Samples were processed in two batches and samples from the different cohorts/study groups were equally distributed across the two experiments to mitigate potential issues with batch effects. PBMCs from the same blood draw and batch from a healthy individual was measured in both experiments to assess reproducibility.

Data analysis

Irregular events and outliers in the raw data were determined and excluded using R-implemented (R version 4.0.0) FlowAI (version 1.18.5) (*54*). Subsequently, correction for spectral overlap (compensation) was performed in FlowJo 10.1.7 (BD Biosciences) using single-stained beads. A new set of fcs files only containing viable, high-quality (based on FlowAI) cells was generated for subsequent analysis of immune cell traits with FlowJo 10.1.7. For the BDC-CR1 panel, gates from two donors required adjustments due to slight signal shifts caused by irregularities in data acquisition which were not detected by FlowAI. Otherwise, identical gates were used across all samples and batches. Markers were divided in two groups based on their purpose to either define immune cell subsets or functional markers/characteristics (Supplementary Table 1). Three different parameters were extracted for subsequent analysis, namely frequency of immune cell populations, frequency of cells expressing functional markers and mean fluorescence signal. Biologically relevant expression was assessed and immune traits with insufficient frequencies or irrelevant expression patterns were manually excluded which resulted in 1758 out of 3787 manually defined immune traits.

For tSNE and FlowSOM analysis, CD4$^+$ T cells and CD8$^+$ T cells (both gated from CD3$^+$CD4$^+$Vγ9$^-$Vδ1$^-$Vδ2$^-$CD1d:PBS57$^-$ conventional T cells), B cells (HLA-DR$^+$CD20$^+$), myeloid cells (HLA-DR$^+$CD20$^-$), innate-like T cells (NKT cells, MAIT cells and cells positive for TCR-γ or -δ reagents) and NK cells/innate lymphoid cells (CD3$^-$HLA-DR$^-$) were separately concatenated from the two chemokine receptor panels CR1 and CR2. The same individuals were included as described for the manual gating analysis, with the exception that we excluded the two samples from the BDC-CR1 panel data which had slight signal shifts as described above. Subsequently, dye aggregates were removed by manual gating to avoid artefacts. The cleaned events were exported as new fcs files and used for R-implemented tSNE (version 0.15) and FlowSOM (version 1.20.0). For FlowSOM, 40 clusters were defined for CD4$^+$ and CD8$^+$ T cells and 30 clusters for all other immune subsets. For clustering, markers used to initially define and extract these immune subsets were excluded from the clustering analysis (Supplementary Table 3). We excluded these markers to avoid parsing of background signal or uniform expression into artificial subpopulations (*55*). Clusters with unusual expression pattern occurred likely because of residual immune cell contaminations and were removed from downstream analysis (Supplementary Table 4). Raw data output from FlowSOM and tSNE analysis are visualized in Supplementary Data 8-13. Subsequent analysis was performed with remaining 388 FlowSOM clusters (B cells, N=60; myeloid cells, N=60; innate-like T cells, N=78; conventional CD4 T cells, N=76; conventional CD8 T cells, N=76; and NK cells, N=38). For tSNE, 50000 cells (27583 cells for innate-like T cells and 25000 for NK cells) from each severity group were concatenated prior to tSNE analysis (perplexity = 30, theta = 0.5, 5000 iterations) in order to maintain priority for tSNE computation equal among patient groups. Fewer cells were used for TSNE in the case of innate-like T cells due to limited numbers of cells in the critical COVID-19 group (total 27583 cells from all patients). We expected lower diversity of NK cell subsets and therefore used 25000 cells per study group for tSNE.

Statistical analysis

Exclusion of individuals

Samples with considerable number of missing manually defined immune trait values were excluded using the missCompare (version 1.0.3) package in R. A cut-off of 10% was applied (i.e. samples with more than 10% missing values were excluded). Two individuals were excluded based on missingness of values for immune traits. None of the immune traits were excluded based on missingness (Cut-off of 80% missing values). For FlowSOM analysis, same samples were used according to the missingness analysis on manually defined traits. Of note, the FlowSOM model was trained on all samples irrespective of missingness to ensure maximum number of cells per study group to train the FlowSOM model.

Assessment of long-term immune perturbations

We distinguished immune traits which were affected by long-term immune perturbations or at steady-state within moderate and severe COVID-19 group. We focused on these two study groups because they span across the longest period between symptom onset and sample collection enabling the most precise analysis of long-term immune trajectories after symptom onset (Extended Data Fig. 1a). Of note, age correlated with hospitalization length in severe but not critical cases and was significantly shorter in severe COVID-19 cases (Extended Data Figs. 1b and c). We used linear regression between rank-normalized immune traits derived from both unsupervised clustering and manual analysis and length of time in days between symptom onset and sample collection. In addition, we compared immune traits in samples with less or more than 60 days between symptom onset and sample collection using Wilcoxon signed-rank test. Long-term perturbated traits were defined as manually defined immune traits with unadjusted $P < 0.001$ in at least one of the analyses ($N = 24$).

Identification of immune traits predictive for COVID-19 severity

Immune traits and FlowSOM clusters with unadjusted P > 0.05 in both analyses described above (linear regression and Wilcoxon signed-rank test) were defined as stable immune traits at steady-state (1365 manually defined immune traits and 291 FlowSOM clusters) and were used to predict immune signatures associated with the development of severe COVID-19. We rank-normalized the data and used logistic regression between mild/moderate (group non-severe) and severe/critical (group severe) cases and corrected for age and experiment (batch). P-values were adjusted using Benjamini-Hochberg false discovery rate (*56*) and adjusted P-values < 0.05 were considered statistically significant.

Acknowledgements

This work was supported by the intramural research program of the Vaccine Research Center (NIAID. NIH). We thank the Flow Cytometry Facility at the Vaccine Research Center including Erica Smit, Esther Thang, Richard Nguyen and Steve Perfetto. In addition, we thank Ingelise Gordon, Charla Andrews, Maria Burgos Florez, Laura Novik, Britta Flach, Emily Coates, Nina Berkowitz and Martin Gaudinski from the VRC Clinical Trials Program and Obrimpong Amoa-Awua and Adrian McDermott from the Vaccine Immunology Program for their support regarding PBMC samples from the NIH and Evergreen cohort. Furthermore, we thank all donors from the VRC and the Washington University cohorts.

Funding

Intramural Research Program of the VRC, NIAID, NIH. This study utilized samples obtained from the Washington University School of Medicine's COVID-19 biorepository, which is supported by: the Barnes-Jewish Hospital Foundation; the Siteman Cancer Center grant P30 CA091842 from the National Cancer Institute of the National Institutes of Health; and the Washington University Institute of Clinical and Translational Sciences grant UL1TR002345 from the National Center for Advancing Translational Sciences of the National Institutes of Health. The content is solely the responsibility of the authors and does not necessarily represent the view of the NIH. M.M. is supported by the National Institute for Health Research (NIHR)-funded BioResource, Clinical Research Facility and Biomedical Research Centre based at Guy's and St Thomas' NHS Foundation Trust in partnership with King's College London.

Author contribution

Conceptualization: T.L and M.R.
Experiments: T.L and Y.I.
Data curation: T.L, M.M. and M.R.
Formal analysis: T.L, M.M. and M.R.
Funding acquisition: M.R.

Methodology: T.L and M.R.

Project administration: T.L and M.R.

Resources: All other

Supervision: T.L and M.R.

Validation: T.L, M.M. and M.R.

Visualization: T.L and M.R.

Writing—original draft: T.L and M.R.

Competing interests

None

Data and materials availability

All data are available in the main text or the supplementary materials. Flow cytometry data corrected for spectral overlap (compensated) are available on FlowRepository (LINK) and contains pre-gated viable cells.

References

1. M. Karmakar, P. M. Lantz, R. Tipirneni, Association of Social and Demographic Factors With COVID-19 Incidence and Death Rates in the US. *JAMA Netw Open* **4**, e2036462 (2021).
2. E. Pairo-Castineira, S. Clohisey, L. Klaric, A. D. Bretherick, K. Rawlik, D. Pasko, S. Walker, N. Parkinson, M. H. Fourman, C. D. Russell, J. Furniss, A. Richmond, E. Gountouna, N. Wrobel, D. Harrison, B. Wang, Y. Wu, A. Meynert, F. Griffiths, W. Oosthuyzen, A. Kousathanas, L. Moutsianas, Z. Yang, R. Zhai, C. Zheng, G. Grimes, R. Beale, J. Millar, B. Shih, S. Keating, M. Zechner, C. Haley, D. J. Porteous, C. Hayward, J. Yang, J. Knight, C. Summers, M. Shankar-Hari, P. Klenerman, L. Turtle, A. Ho, S. C. Moore, C. Hinds, P. Horby, A. Nichol, D. Maslove, L. Ling, D. McAuley, H. Montgomery, T. Walsh, A. C. Pereira, A. Renieri, O. I. Gen, I. C. Investigators, C.-H. G. Initiative, I. andMe, B. Investigators, C. I. Gen, X. Shen, C. P. Ponting, A. Fawkes, A. Tenesa, M. Caulfield, R. Scott, K. Rowan, L. Murphy, P. J. M. Openshaw, M. G. Semple, A. Law, V. Vitart, J. F. Wilson, J. K. Baillie, Genetic mechanisms of critical illness in COVID-19. *Nature* **591**, 92-98 (2021).
3. C.-H. G. Initiative, Mapping the human genetic architecture of COVID-19. *Nature*, (2021).
4. M. Roederer, L. Quaye, M. Mangino, M. H. Beddall, Y. Mahnke, P. Chattopadhyay, I. Tosi, L. Napolitano, M. Terranova Barberio, C. Menni, F. Villanova, P. Di Meglio, T. D. Spector, F. O. Nestle, The genetic architecture of the human immune system: a bioresource for autoimmunity and disease pathogenesis. *Cell* **161**, 387-403 (2015).
5. D. P. Dyer, Understanding the mechanisms that facilitate specificity, not redundancy, of chemokine-mediated leukocyte recruitment. *Immunology* **160**, 336-344 (2020).
6. J. W. Griffith, C. L. Sokol, A. D. Luster, Chemokines and chemokine receptors: positioning cells for host defense and immunity. *Annu Rev Immunol* **32**, 659-702 (2014).
7. C. L. Sokol, A. D. Luster, The chemokine system in innate immunity. *Cold Spring Harb Perspect Biol* **7**, (2015).
8. I. F. Charo, R. M. Ransohoff, The many roles of chemokines and chemokine receptors in inflammation. *N Engl J Med* **354**, 610-621 (2006).
9. A. Iwasaki, P. S. Pillai, Innate immunity to influenza virus infection. *Nat Rev Immunol* **14**, 315-328 (2014).
10. J. L. Schultze, A. C. Aschenbrenner, COVID-19 and the human innate immune system. *Cell* **184**, 1671-1692 (2021).
11. M. Merad, J. C. Martin, Pathological inflammation in patients with COVID-19: a key role for monocytes and macrophages. *Nat Rev Immunol* **20**, 355-362 (2020).
12. C. J. Duncan, S. M. Mohamad, D. F. Young, A. J. Skelton, T. R. Leahy, D. C. Munday, K. M. Butler, S. Morfopoulou, J. R. Brown, M. Hubank, J. Connell, P. J. Gavin, C. McMahon, E. Dempsey, N. E. Lynch, T. S. Jacques, M. Valappil, A. J.

Cant, J. Breuer, K. R. Engelhardt, R. E. Randall, S. Hambleton, Human IFNAR2 deficiency: Lessons for antiviral immunity. *Sci Transl Med* **7**, 307ra154 (2015).

13. A. Park, A. Iwasaki, Type I and Type III Interferons - Induction, Signaling, Evasion, and Application to Combat COVID-19. *Cell Host Microbe* **27**, 870-878 (2020).
14. J. Hadjadj, N. Yatim, L. Barnabei, A. Corneau, J. Boussier, N. Smith, H. Pere, B. Charbit, V. Bondet, C. Chenevier-Gobeaux, P. Breillat, N. Carlier, R. Gauzit, C. Morbieu, F. Pene, N. Marin, N. Roche, T. A. Szwebel, S. H. Merkling, J. M. Treluyer, D. Veyer, L. Mouthon, C. Blanc, P. L. Tharaux, F. Rozenberg, A. Fischer, D. Duffy, F. Rieux-Laucat, S. Kerneis, B. Terrier, Impaired type I interferon activity and inflammatory responses in severe COVID-19 patients. *Science* **369**, 718-724 (2020).
15. B. Sposito, A. Broggi, L. Pandolfi, S. Crotta, N. Clementi, R. Ferrarese, S. Sisti, E. Criscuolo, R. Spreafico, J. M. Long, A. Ambrosi, E. Liu, V. Frangipane, L. Saracino, S. Bozzini, L. Marongiu, F. A. Facchini, A. Bottazzi, T. Fossali, R. Colombo, M. Clementi, E. Tagliabue, J. Chou, A. E. Pontiroli, F. Meloni, A. Wack, N. Mancini, I. Zanoni, The interferon landscape along the respiratory tract impacts the severity of COVID-19. *Cell* **184**, 4953-4968 e4916 (2021).
16. P. Bastard, L. B. Rosen, Q. Zhang, E. Michailidis, H. H. Hoffmann, Y. Zhang, K. Dorgham, Q. Philippot, J. Rosain, V. Beziat, J. Manry, E. Shaw, L. Haljasmagi, P. Peterson, L. Lorenzo, L. Bizien, S. Trouillet-Assant, K. Dobbs, A. A. de Jesus, A. Belot, A. Kallaste, E. Catherinot, Y. Tandjaoui-Lambiotte, J. Le Pen, G. Kerner, B. Bigio, Y. Seeleuthner, R. Yang, A. Bolze, A. N. Spaan, O. M. Delmonte, M. S. Abers, A. Aiuti, G. Casari, V. Lampasona, L. Piemonti, F. Ciceri, K. Bilguvar, R. P. Lifton, M. Vasse, D. M. Smadja, M. Migaud, J. Hadjadj, B. Terrier, D. Duffy, L. Quintana-Murci, D. van de Beek, L. Roussel, D. C. Vinh, S. G. Tangye, F. Haerynck, D. Dalmau, J. Martinez-Picado, P. Brodin, M. C. Nussenzweig, S. Boisson-Dupuis, C. Rodriguez-Gallego, G. Vogt, T. H. Mogensen, A. J. Oler, J. Gu, P. D. Burbelo, J. I. Cohen, A. Biondi, L. R. Bettini, M. D'Angio, P. Bonfanti, P. Rossignol, J. Mayaux, F. Rieux-Laucat, E. S. Husebye, F. Fusco, M. V. Ursini, L. Imberti, A. Sottini, S. Paghera, E. Quiros-Roldan, C. Rossi, R. Castagnoli, D. Montagna, A. Licari, G. L. Marseglia, X. Duval, J. Ghosn, H. Lab, N.-U. I. R. t. C. Group, C. Clinicians, C.-S. Clinicians, C. G. Imagine, C. C. S. G. French, C. Milieu Interieur, V. C. C. Co, U. M. C. C.-B. Amsterdam, C. H. G. Effort, J. S. Tsang, R. Goldbach-Mansky, K. Kisand, M. S. Lionakis, A. Puel, S. Y. Zhang, S. M. Holland, G. Gorochov, E. Jouanguy, C. M. Rice, A. Cobat, L. D. Notarangelo, L. Abel, H. C. Su, J. L. Casanova, Autoantibodies against type I IFNs in patients with life-threatening COVID-19. *Science* **370**, (2020).
17. Q. Zhang, P. Bastard, Z. Liu, J. Le Pen, M. Moncada-Velez, J. Chen, M. Ogishi, I. K. D. Sabli, S. Hodeib, C. Korol, J. Rosain, K. Bilguvar, J. Ye, A. Bolze, B. Bigio, R. Yang, A. A. Arias, Q. Zhou, Y. Zhang, F. Onodi, S. Korniotis, L. Karpf, Q. Philippot, M. Chbihi, L. Bonnet-Madin, K. Dorgham, N. Smith, W. M. Schneider, B. S. Razooky, H. H. Hoffmann, E. Michailidis, L. Moens, J. E. Han, L. Lorenzo, L. Bizien, P. Meade, A. L. Neehus, A. C. Ugurbil, A. Corneau, G. Kerner, P. Zhang, F. Rapaport, Y. Seeleuthner, J. Manry, C. Masson, Y. Schmitt, A. Schluter, T. Le Voyer, T. Khan, J. Li, J. Fellay, L. Roussel, M. Shahrooei, M. F. Alosaimi, D. Mansouri, H. Al-Saud, F. Al-Mulla, F. Almourfi, S. Z. Al-Muhsen, F. Alsohime, S.

Al Turki, R. Hasanato, D. van de Beek, A. Biondi, L. R. Bettini, M. D'Angio, P. Bonfanti, L. Imberti, A. Sottini, S. Paghera, E. Quiros-Roldan, C. Rossi, A. J. Oler, M. F. Tompkins, C. Alba, I. Vandernoot, J. C. Goffard, G. Smits, I. Migeotte, F. Haerynck, P. Soler-Palacin, A. Martin-Nalda, R. Colobran, P. E. Morange, S. Keles, F. Colkesen, T. Ozcelik, K. K. Yasar, S. Senoglu, S. N. Karabela, C. Rodriguez-Gallego, G. Novelli, S. Hraiech, Y. Tandjaoui-Lambiotte, X. Duval, C. Laouenan, C.-S. Clinicians, C. Clinicians, C. G. Imagine, C. C. S. G. French, V. C. C. Co, U. M. C. C.-B. Amsterdam, C. H. G. Effort, N.-U. T. C. I. Group, A. L. Snow, C. L. Dalgard, J. D. Milner, D. C. Vinh, T. H. Mogensen, N. Marr, A. N. Spaan, B. Boisson, S. Boisson-Dupuis, J. Bustamante, A. Puel, M. J. Ciancanelli, I. Meyts, T. Maniatis, V. Soumelis, A. Amara, M. Nussenzweig, A. Garcia-Sastre, F. Krammer, A. Pujol, D. Duffy, R. P. Lifton, S. Y. Zhang, G. Gorochov, V. Beziat, E. Jouanguy, V. Sancho-Shimizu, C. M. Rice, L. Abel, L. D. Notarangelo, A. Cobat, H. C. Su, J. L. Casanova, Inborn errors of type I IFN immunity in patients with life-threatening COVID-19. *Science* **370**, (2020).

18. C. Asselin-Paturel, G. Trinchieri, Production of type I interferons: plasmacytoid dendritic cells and beyond. *J Exp Med* **202**, 461-465 (2005).
19. F. J. Ryan, C. M. Hope, M. G. Masavuli, M. A. Lynn, Z. A. Mekonnen, A. E. Lip Yeow, P. Garcia-Valtanen, Z. Al-Delfi, J. Gummow, C. Ferguson, S. O'Connor, B. A. Reddi, D. Shaw, C. Kok-Lim, J. M. Gleadle, M. R. Beard, S. C. Barry, B. Grubor-Bauk, D. J. Lynn, Long-term perturbation of the peripheral immune system months after SARS-CoV-2 infection. *medRxiv*, (2021).
20. L. Bergamaschi, F. Mescia, L. Turner, A. L. Hanson, P. Kotagiri, B. J. Dunmore, H. Ruffieux, A. De Sa, O. Huhn, M. D. Morgan, P. P. Gerber, M. R. Wills, S. Baker, F. J. Calero-Nieto, R. Doffinger, G. Dougan, A. Elmer, I. G. Goodfellow, R. K. Gupta, M. Hosmillo, K. Hunter, N. Kingston, P. J. Lehner, N. J. Matheson, J. K. Nicholson, A. M. Petrunkina, S. Richardson, C. Saunders, J. E. D. Thaventhiran, E. J. M. Toonen, M. P. Weekes, I. Cambridge Institute of Therapeutic, C. B. C. Infectious Disease-National Institute of Health Research, B. Gottgens, M. Toshner, C. Hess, J. R. Bradley, P. A. Lyons, K. G. C. Smith, Longitudinal analysis reveals that delayed bystander CD8+ T cell activation and early immune pathology distinguish severe COVID-19 from mild disease. *Immunity* **54**, 1257-1275 e1258 (2021).
21. S. Jost, M. Altfeld, Control of human viral infections by natural killer cells. *Annu Rev Immunol* **31**, 163-194 (2013).
22. C. Maucourant, I. Filipovic, A. Ponzetta, S. Aleman, M. Cornillet, L. Hertwig, B. Strunz, A. Lentini, B. Reinius, D. Brownlie, A. Cuapio, E. H. Ask, R. M. Hull, A. Haroun-Izquierdo, M. Schaffer, J. Klingstrom, E. Folkesson, M. Buggert, J. K. Sandberg, L. I. Eriksson, O. Rooyackers, H. G. Ljunggren, K. J. Malmberg, J. Michaelsson, N. Marquardt, Q. Hammer, K. Stralin, N. K. Bjorkstrom, C.-S. G. Karolinska, Natural killer cell immunotypes related to COVID-19 disease severity. *Sci Immunol* **5**, (2020).
23. A. Cerutti, M. Cols, I. Puga, Marginal zone B cells: virtues of innate-like antibody-producing lymphocytes. *Nat Rev Immunol* **13**, 118-132 (2013).
24. C. Lucas, P. Wong, J. Klein, T. B. R. Castro, J. Silva, M. Sundaram, M. K. Ellingson, T. Mao, J. E. Oh, B. Israelow, T. Takahashi, M. Tokuyama, P. Lu, A.

Venkataraman, A. Park, S. Mohanty, H. Wang, A. L. Wyllie, C. B. F. Vogels, R. Earnest, S. Lapidus, I. M. Ott, A. J. Moore, M. C. Muenker, J. B. Fournier, M. Campbell, C. D. Odio, A. Casanovas-Massana, I. T. Yale, R. Herbst, A. C. Shaw, R. Medzhitov, W. L. Schulz, N. D. Grubaugh, C. Dela Cruz, S. Farhadian, A. I. Ko, S. B. Omer, A. Iwasaki, Longitudinal analyses reveal immunological misfiring in severe COVID-19. *Nature* **584**, 463-469 (2020).

25. C. A. Dutertre, E. Becht, S. E. Irac, A. Khalilnezhad, V. Narang, S. Khalilnezhad, P. Y. Ng, L. L. van den Hoogen, J. Y. Leong, B. Lee, M. Chevrier, X. M. Zhang, P. J. A. Yong, G. Koh, J. Lum, S. W. Howland, E. Mok, J. Chen, A. Larbi, H. K. K. Tan, T. K. H. Lim, P. Karagianni, A. G. Tzioufas, B. Malleret, J. Brody, S. Albani, J. van Roon, T. Radstake, E. W. Newell, F. Ginhoux, Single-Cell Analysis of Human Mononuclear Phagocytes Reveals Subset-Defining Markers and Identifies Circulating Inflammatory Dendritic Cells. *Immunity* **51**, 573-589 e578 (2019).
26. F. Mair, T. Liechti, Comprehensive Phenotyping of Human Dendritic Cells and Monocytes. *Cytometry A* **99**, 231-242 (2021).
27. R. L. Chua, S. Lukassen, S. Trump, B. P. Hennig, D. Wendisch, F. Pott, O. Debnath, L. Thurmann, F. Kurth, M. T. Volker, J. Kazmierski, B. Timmermann, S. Twardziok, S. Schneider, F. Machleidt, H. Muller-Redetzky, M. Maier, A. Krannich, S. Schmidt, F. Balzer, J. Liebig, J. Loske, N. Suttorp, J. Eils, N. Ishaque, U. G. Liebert, C. von Kalle, A. Hocke, M. Witzenrath, C. Goffinet, C. Drosten, S. Laudi, I. Lehmann, C. Conrad, L. E. Sander, R. Eils, COVID-19 severity correlates with airway epithelium-immune cell interactions identified by single-cell analysis. *Nat Biotechnol* **38**, 970-979 (2020).
28. E. Wauters, P. Van Mol, A. D. Garg, S. Jansen, Y. Van Herck, L. Vanderbeke, A. Bassez, B. Boeckx, B. Malengier-Devlies, A. Timmerman, T. Van Brussel, T. Van Buyten, R. Schepers, E. Heylen, D. Dauwe, C. Dooms, J. Gunst, G. Hermans, P. Meersseman, D. Testelmans, J. Yserbyt, P. Matthys, S. Tejpar, , J. Neyts, J. Wauters, J. Qian, D. Lambrechts, Discriminating Mild from Critical COVID-19 by Innate and Adaptive Immune Single-cell Profiling of Bronchoalveolar Lavages. *bioRxiv*, (2020).
29. P. Brodin, M. M. Davis, Human immune system variation. *Nat Rev Immunol* **17**, 21-29 (2017).
30. W. G. Glass, J. K. Lim, R. Cholera, A. G. Pletnev, J. L. Gao, P. M. Murphy, Chemokine receptor CCR5 promotes leukocyte trafficking to the brain and survival in West Nile virus infection. *J Exp Med* **202**, 1087-1098 (2005).
31. J. E. Kohlmeier, S. C. Miller, J. Smith, B. Lu, C. Gerard, T. Cookenham, A. D. Roberts, D. L. Woodland, The chemokine receptor CCR5 plays a key role in the early memory CD8+ T cell response to respiratory virus infections. *Immunity* **29**, 101-113 (2008).
32. C. Mionnet, V. Buatois, A. Kanda, V. Milcent, S. Fleury, D. Lair, M. Langelot, Y. Lacoeuille, E. Hessel, R. Coffman, A. Magnan, D. Dombrowicz, N. Glaichenhaus, V. Julia, CX3CR1 is required for airway inflammation by promoting T helper cell survival and maintenance in inflamed lung. *Nat Med* **16**, 1305-1312 (2010).
33. S. Chakarov, H. Y. Lim, L. Tan, S. Y. Lim, P. See, J. Lum, X. M. Zhang, S. Foo, S. Nakamizo, K. Duan, W. T. Kong, R. Gentek, A. Balachander, D. Carbajo, C. Bleriot, B. Malleret, J. K. C. Tam, S. Baig, M. Shabeer, S. E. S. Toh, A. Schlitzer,

A. Larbi, T. Marichal, B. Malissen, J. Chen, M. Poidinger, K. Kabashima, M. Bajenoff, L. G. Ng, V. Angeli, F. Ginhoux, Two distinct interstitial macrophage populations coexist across tissues in specific subtissular niches. *Science* **363**, (2019).

34. Z. Mikhak, J. P. Strassner, A. D. Luster, Lung dendritic cells imprint T cell lung homing and promote lung immunity through the chemokine receptor CCR4. *J Exp Med* **210**, 1855-1869 (2013).

35. G. Zhou, S. W. Juang, K. P. Kane, NK cells exacerbate the pathology of influenza virus infection in mice. *Eur J Immunol* **43**, 929-938 (2013).

36. M. Schorer, N. Rakebrandt, K. Lambert, A. Hunziker, K. Pallmer, A. Oxenius, A. Kipar, S. Stertz, N. Joller, TIGIT limits immune pathology during viral infections. *Nat Commun* **11**, 1288 (2020).

37. A. Vanderheiden, J. Thomas, A. L. Soung, M. E. Davis-Gardner, K. Floyd, F. Jin, D. A. Cowan, K. Pellegrini, A. Creanga, A. Pegu, A. Derrien-Colemyn, P. Y. Shi, A. Grakoui, R. S. Klein, S. E. Bosinger, J. E. Kohlmeier, V. D. Menachery, M. S. Suthar, CCR2-dependent monocyte-derived cells restrict SARS-CoV-2 infection. *bioRxiv*, (2021).

38. T. Sheahan, T. E. Morrison, W. Funkhouser, S. Uematsu, S. Akira, R. S. Baric, M. T. Heise, MyD88 is required for protection from lethal infection with a mouse-adapted SARS-CoV. *PLoS Pathog* **4**, e1000240 (2008).

39. M. J. Cameron, L. Ran, L. Xu, A. Danesh, J. F. Bermejo-Martin, C. M. Cameron, M. P. Muller, W. L. Gold, S. E. Richardson, S. M. Poutanen, B. M. Willey, M. E. DeVries, Y. Fang, C. Seneviratne, S. E. Bosinger, D. Persad, P. Wilkinson, L. D. Greller, R. Somogyi, A. Humar, S. Keshavjee, M. Louie, M. B. Loeb, J. Brunton, A. J. McGeer, S. R. N. Canadian, D. J. Kelvin, Interferon-mediated immunopathological events are associated with atypical innate and adaptive immune responses in patients with severe acute respiratory syndrome. *J Virol* **81**, 8692-8706 (2007).

40. R. Channappanavar, A. R. Fehr, R. Vijay, M. Mack, J. Zhao, D. K. Meyerholz, S. Perlman, Dysregulated Type I Interferon and Inflammatory Monocyte-Macrophage Responses Cause Lethal Pneumonia in SARS-CoV-Infected Mice. *Cell Host Microbe* **19**, 181-193 (2016).

41. R. Channappanavar, A. R. Fehr, J. Zheng, C. Wohlford-Lenane, J. E. Abrahante, M. Mack, R. Sompallae, P. B. McCray, Jr., D. K. Meyerholz, S. Perlman, IFN-I response timing relative to virus replication determines MERS coronavirus infection outcomes. *J Clin Invest* **129**, 3625-3639 (2019).

42. N. A. de Weerd, T. Nguyen, The interferons and their receptors--distribution and regulation. *Immunol Cell Biol* **90**, 483-491 (2012).

43. M. C. Abt, L. C. Osborne, L. A. Monticelli, T. A. Doering, T. Alenghat, G. F. Sonnenberg, M. A. Paley, M. Antenus, K. L. Williams, J. Erikson, E. J. Wherry, D. Artis, Commensal bacteria calibrate the activation threshold of innate antiviral immunity. *Immunity* **37**, 158-170 (2012).

44. A. A. Patel, Y. Zhang, J. N. Fullerton, L. Boelen, A. Rongvaux, A. A. Maini, V. Bigley, R. A. Flavell, D. W. Gilroy, B. Asquith, D. Macallan, S. Yona, The fate and lifespan of human monocyte subsets in steady state and systemic inflammation. *J Exp Med* **214**, 1913-1923 (2017).

45. A. A. Patel, F. Ginhoux, S. Yona, Monocytes, macrophages, dendritic cells and neutrophils: an update on lifespan kinetics in health and disease. *Immunology* **163**, 250-261 (2021).

46. K. Liu, C. Waskow, X. Liu, K. Yao, J. Hoh, M. Nussenzweig, Origin of dendritic cells in peripheral lymphoid organs of mice. *Nat Immunol* **8**, 578-583 (2007).

47. L. Westera, J. Drylewicz, I. den Braber, T. Mugwagwa, I. van der Maas, L. Kwast, T. Volman, E. H. van de Weg-Schrijver, I. Bartha, G. Spierenburg, K. Gaiser, M. T. Ackermans, B. Asquith, R. J. de Boer, K. Tesselaar, J. A. Borghans, Closing the gap between T-cell life span estimates from stable isotope-labeling studies in mice and humans. *Blood* **122**, 2205-2212 (2013).

48. J. E. Mold, P. Reu, A. Olin, S. Bernard, J. Michaelsson, S. Rane, A. Yates, A. Khosravi, M. Salehpour, G. Possnert, P. Brodin, J. Frisen, Cell generation dynamics underlying naive T-cell homeostasis in adult humans. *PLoS Biol* **17**, e3000383 (2019).

49. B. K. Patterson, H. Seethamraju, K. Dhody, M. J. Corley, K. Kazempour, J. Lalezari, A. P. S. Pang, C. Sugai, E. Mahyari, E. B. Francisco, A. Pise, H. Rodrigues, H. L. Wu, G. M. Webb, B. S. Park, S. Kelly, N. Pourhassan, A. Lelic, L. Kdouh, M. Herrera, E. Hall, B. N. Bimber, M. Plassmeyer, R. Gupta, O. Alpan, J. A. O'Halloran, P. A. Mudd, E. Akalin, L. C. Ndhlovu, J. B. Sacha, CCR5 Inhibition in Critical COVID-19 Patients Decreases Inflammatory Cytokines, Increases CD8 T-Cells, and Decreases SARS-CoV2 RNA in Plasma by Day 14. *Int J Infect Dis*, (2020).

50. B. Yang, J. A. Fulcher, J. Ahn, M. Berro, D. Goodman-Meza, K. Dhody, J. B. Sacha, A. Naeim, O. O. Yang, Clinical Characteristics and Outcomes of COVID-19 Patients Receiving Compassionate Use Leronlimab. *Clin Infect Dis*, (2020).

51. A. C. Kalil, A. K. Mehta, T. F. Patterson, N. Erdmann, C. A. Gomez, M. K. Jain, C. R. Wolfe, G. M. Ruiz-Palacios, S. Kline, J. Regalado Pineda, A. F. Luetkemeyer, M. S. Harkins, P. E. H. Jackson, N. M. Iovine, V. F. Tapson, M. D. Oh, J. A. Whitaker, R. A. Mularski, C. I. Paules, D. Ince, J. Takasaki, D. A. Sweeney, U. Sandkovsky, D. L. Wyles, E. Hohmann, K. A. Grimes, R. Grossberg, M. Laguio-Vila, A. A. Lambert, D. Lopez de Castilla, E. Kim, L. Larson, C. R. Wan, J. J. Traenkner, P. O. Ponce, J. E. Patterson, P. A. Goepfert, T. A. Sofarelli, S. Mocherla, E. R. Ko, A. Ponce de Leon, S. B. Doernberg, R. L. Atmar, R. C. Maves, F. Dangond, J. Ferreira, M. Green, M. Makowski, T. Bonnett, T. Beresnev, V. Ghazaryan, W. Dempsey, S. U. Nayak, L. Dodd, K. M. Tomashek, J. H. Beigel, A.-s. g. members, Efficacy of interferon beta-1a plus remdesivir compared with remdesivir alone in hospitalised adults with COVID-19: a double-bind, randomised, placebo-controlled, phase 3 trial. *Lancet Respir Med* **9**, 1365-1376 (2021).

52. M. Beddall, P. K. Chattopadhyay, S. F. Kao, K. Foulds, M. Roederer, A simple tube adapter to expedite and automate thawing of viably frozen cells. *J Immunol Methods* **439**, 74-78 (2016).

53. T. Liechti, M. Roederer, OMIP-058: 30-Parameter Flow Cytometry Panel to Characterize iNKT, NK, Unconventional and Conventional T Cells. *Cytometry A* **95**, 946-951 (2019).

54. G. Monaco, H. Chen, M. Poidinger, J. Chen, J. P. de Magalhaes, A. Larbi, flowAI: automatic and interactive anomaly discerning tools for flow cytometry data. *Bioinformatics* **32**, 2473-2480 (2016).

55. T. Liechti, L. M. Weber, T. M. Ashhurst, N. Stanley, M. Prlic, S. Van Gassen, F. Mair, An updated guide for the perplexed: cytometry in the high-dimensional era. *Nat Immunol* **22**, 1190-1197 (2021).

56. Y. Benjamini, Y. Hochberg, Controlling the False Discovery Rate: A Practical and Powerful Approach to Multiple Testing. *Journal of the Royal Statistical Society: Series B (Methodological)* **57**, 289-300 (1995).

Figures

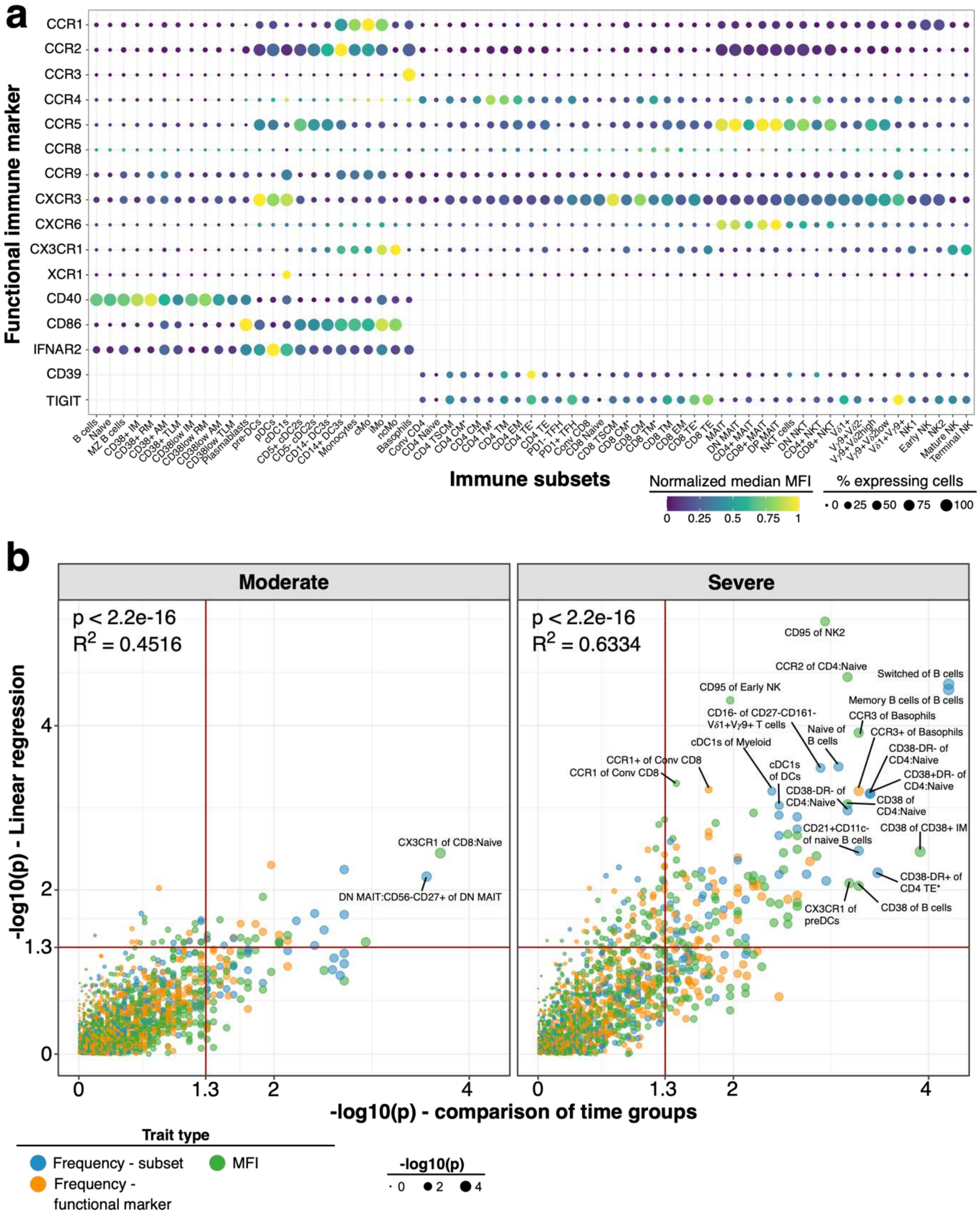
a
Functional immune marker
CCR1
CCR2
CCR3
CCR4
CCR5
CCR8
CCR9
CXCR3
CXCR6
CX3CR1
XCR1
CD40
CD86
IFNAR2
CD39
TIGIT
B cells
Naive
MZ B cells
CD38+ IM
CD38+ RM
CD38+ AM
CD38+ TLM
CD38low IM
CD38low RM
CD38low AM
CD38low TLM
Plasmablasts
pre-DCs
pDCs
cDC1s
CD5+ cDC2s
CD5- cDC2s
CD14- DC3s
CD14+ DC3s
Monocytes
cMo
iMo
ncMo
Basophils
Conv CD4
CD4 Naive
CD4 TSCM
CD4 CM*
CD4 CM
CD4 TM*
CD4 TM
CD4 EM
CD4 TE*
CD4 TE
PD1- TFH
PD1+ TFH
Conv CD8
CD8 Naive
CD8 TSCM
CD8 CM*
CD8 CM
CD8 TM*
CD8 TM
CD8 EM
CD8 TE*
CD8 TE
MAIT
DN MAIT
CD4+ MAIT
CD8+ MAIT
DP MAIT
NKT cells
DN NKT
CD4+ NKT
CD8+ NKT
Vδ1+
Vγ9+Vδ2-
Vγ9+Vδ2high
Vγ9+Vδ2low
Vδ1+Vγ9+
NK1
Early NK
NK2
Mature NK
Terminal NK
Immune subsets
Normalized median MFI
0
0.25
0.5
0.75
1
% expressing cells
0
25
50
75
100
b
Moderate
Severe
p < 2.2e-16
R² = 0.4516
p < 2.2e-16
R² = 0.6334
-log10(p) - Linear regression
-log10(p) - comparison of time groups
0
1.3
2
4
CX3CR1 of CD8:Naive
DN MAIT:CD56-CD27+ of DN MAIT
CD95 of NK2
CCR2 of CD4:Naive
Switched of B cells
CD95 of Early NK
Memory B cells of B cells
CD16- of CD27-CD161-
Vδ1+Vγ9+ T cells
CCR3 of Basophils
cDC1s of Myeloid
Naive of
B cells
CCR3+ of Basophils
CCR1+ of Conv CD8
CD38-DR- of
CD4:Naive
CCR1 of Conv CD8
cDC1s
of DCs
CD38+DR- of
CD4:Naive
CD38-DR- of
CD4:Naive
CD38 of
CD4:Naive
CD21+CD11c-
of naive B cells
CD38 of CD38+ IM
CD38-DR+ of
CD4 TE*
CX3CR1 of
preDCs
CD38 of B cells
Trait type
Frequency - subset
MFI
Frequency -
functional marker
-log10(p)
0
2
4

Figure 1: Expression of functional markers and temporal dynamics of immune traits in COVID-19

a) Expression of chemokine receptors, CD40, CD86, IFNAR2, CD39 and TIGIT (rows) on immune cell populations (columns) is depicted. Median of mean fluorescence intensities (MFI) derived from 173 healthy individuals is visualized by min-max normalized color gradient. Dot size corresponds to median percentage of cells expressing these markers. Missing dots indicate that marker was not measured.

b) Immune traits (N = 1779) at baseline or affected by long-term perturbations were distinguished in individuals recovered from moderate (left) and severe (right) COVID-19 cases. A combination of I) linear regression analysis between immune traits and days between symptom onset and sample collection and II) comparison of samples collected before and after 60 days of symptom onset using a Wilcoxon test was used as described in Online methods. Plot shows unadjusted -log10 P-values from both analyses. Dot size increases with significance from Wilcoxon test. Trait types are colored (Frequency of immune subset in blue, Frequency of expressing functional marker in orange and MFI values in green). Red line highlights threshold for unadjusted significance (P = 0.05).

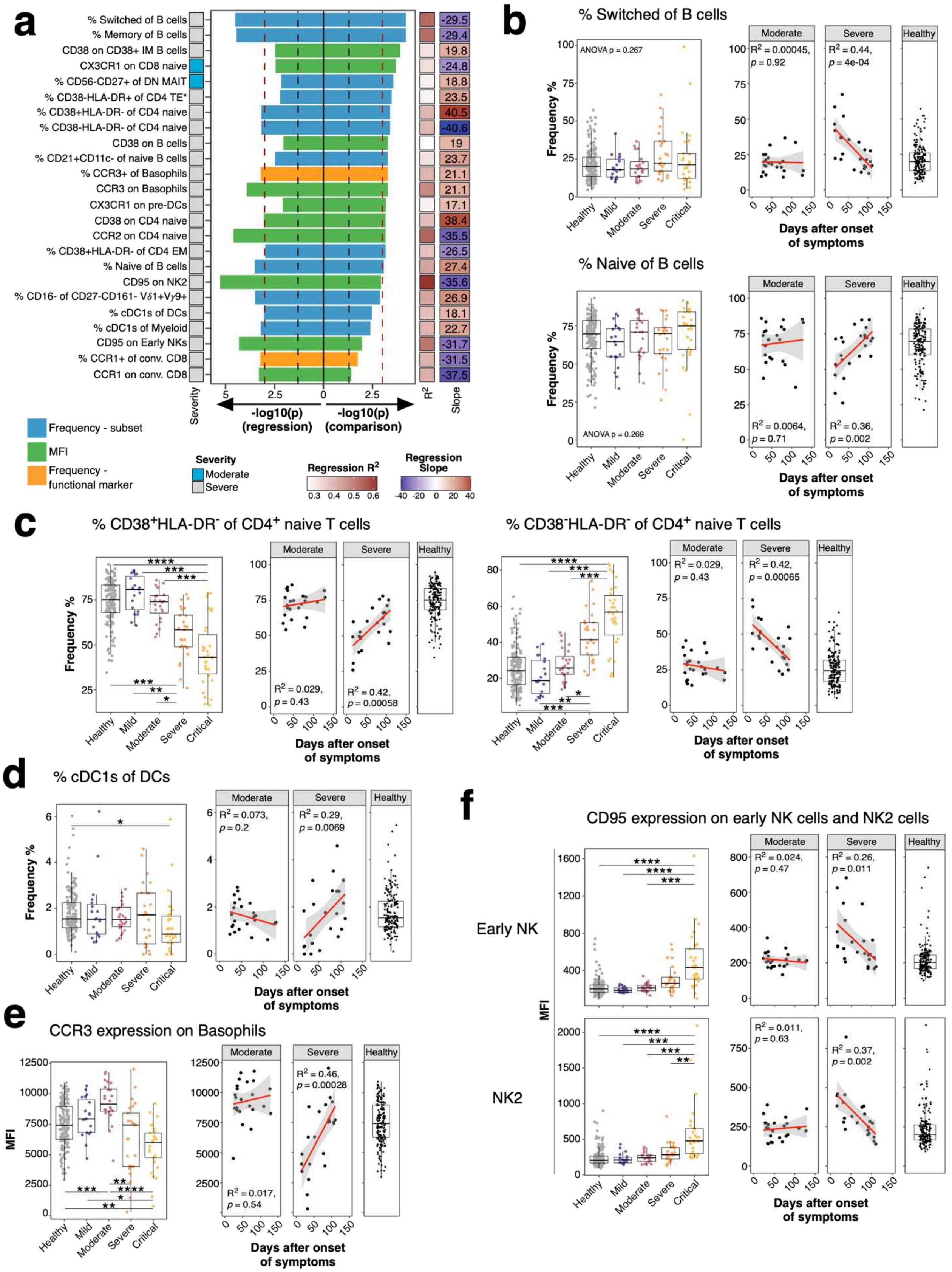
a
% Switched of B cells
% Memory of B cells
CD38 on CD38+ IM B cells
CX3CR1 on CD8 naive
% CD56-CD27+ of DN MAIT
% CD38-HLA-DR+ of CD4 TE*
% CD38+HLA-DR- of CD4 naive
% CD38-HLA-DR- of CD4 naive
CD38 on B cells
% CD21+CD11c- of naive B cells
% CCR3+ of Basophils
CCR3 on Basophils
CX3CR1 on pre-DCs
CD38 on CD4 naive
CCR2 on CD4 naive
% CD38+HLA-DR- of CD4 EM
% Naive of B cells
CD95 on NK2
% CD16- of CD27-CD161- Vδ1+Vγ9+
% cDC1s of DCs
% cDC1s of Myeloid
CD95 on Early NKs
% CCR1+ of conv. CD8
CCR1 on conv. CD8
-29.5
-29.4
19.8
-24.8
18.8
23.5
40.5
-40.6
19
23.7
21.1
21.1
17.1
38.4
-35.5
-26.5
27.4
-35.6
26.9
18.1
22.7
-31.7
-31.5
-37.5
Severity
5
2.5
0
2.5
-log10(p) (regression)
-log10(p) (comparison)
R²
Slope
Frequency - subset
MFI
Frequency - functional marker
Severity
Moderate
Severe
Regression R²
0.3 0.4 0.5 0.6
Regression Slope
-40 -20 0 20 40
b
% Switched of B cells
ANOVA p = 0.267
Frequency %
Healthy
Mild
Moderate
Severe
Critical
Moderate
Severe
Healthy
R² = 0.00045, p = 0.92
R² = 0.44, p = 4e-04
Days after onset of symptoms
% Naive of B cells
ANOVA p = 0.269
R² = 0.0064, p = 0.71
R² = 0.36, p = 0.002
c
% CD38⁺HLA-DR⁻ of CD4⁺ naive T cells
R² = 0.029, p = 0.43
R² = 0.42, p = 0.00058
% CD38⁻HLA-DR⁻ of CD4⁺ naive T cells
R² = 0.029, p = 0.43
R² = 0.42, p = 0.00065
d
% cDC1s of DCs
R² = 0.073, p = 0.2
R² = 0.29, p = 0.0069
e
CCR3 expression on Basophils
MFI
R² = 0.46, p = 0.00028
R² = 0.017, p = 0.54
f
CD95 expression on early NK cells and NK2 cells
Early NK
NK2
R² = 0.024, p = 0.47
R² = 0.26, p = 0.011
R² = 0.011, p = 0.63
R² = 0.37, p = 0.002
Days after onset of symptoms

Figure 2: Long-term perturbations of immune traits in COVID-19

a) Top immune traits affected by long-term perturbations are depicted. Traits are derived from analysis in Figure 1b and selected for P-value <0.001 in one of both analysis (linear regression and/or Wilcoxon test). Bars pointing to the left and right are derived from linear regression and Wilcoxon test, respectively, and are colored based on trait type (Frequency of immune subset in blue, Frequency of expressing functional marker in orange and MFI values in green). Colored bar on the left depicts severity group from which the significant trait is derived. R^2 and slope from linear regression are shown as colored bars on the right. Values in the right bar are slope values from linear regression. Red and black dashed lines show P-value cut-off of 0.001 and 0.05, respectively.

b) Frequencies of switched (top row) and naïve (bottom row) B cells of total B cells are shown. Plot on the left shows frequencies as boxplots for healthy subjects (grey) and individuals recovered from mild (purple), moderate (burgundy), severe (orange) or critical COVID-19 (yellow). The two plots on the right show the frequency of cells as a function of time between symptom onset and sample collection for individuals recovered from moderate and severe COVID-19. Far right plot shows the distribution of the traits in 173 healthy individuals. Similar to Fig. 2b, dynamics of **c)** $CD38^+HLA\text{-}DR^-$ (left) and $CD38^-HLA\text{-}DR^-$ of CD4 naïve T cells (right), **d)** frequencies of cDC1s of total DCs, **e)** CCR3 MFI of basophils and **f)** CD95 MFI of early NK and NK2 cells are shown.

Age-corrected residuals from linear regression were used for statistical analysis. For comparison between groups, one-way ANOVA was used on residuals to test for overall significant difference prior to Wilcoxon test with Bonferroni correction. Second and third plot show dot plots with linear regression (red line) and 95% confidence interval for individuals recovered from moderate and severe COVID-19, respectively. * $P < 0.05$, ** $P < 0.01$, *** $P < 0.001$, **** $P < 0.0001$

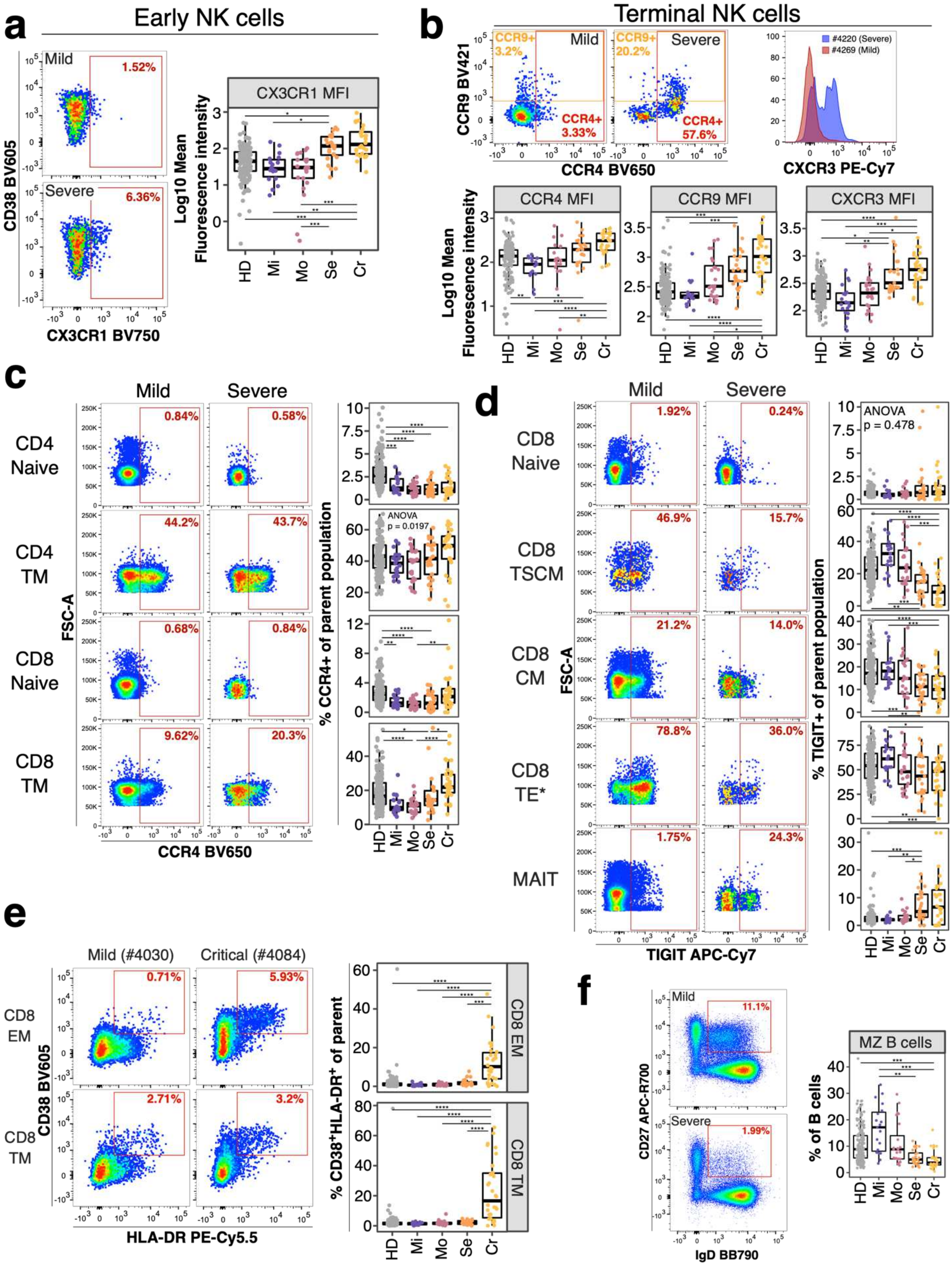
a
Early NK cells
Mild
1.52%
Severe
6.36%
CD38 BV605
CX3CR1 BV750
CX3CR1 MFI
Log10 Mean Fluorescence intensity
HD
Mi
Mo
Se
Cr
b
Terminal NK cells
CCR9+ 3.2%
Mild
CCR4+ 3.33%
CCR9+ 20.2%
Severe
CCR4+ 57.6%
CCR9 BV421
CCR4 BV650
#4220 (Severe)
#4269 (Mild)
CXCR3 PE-Cy7
CCR4 MFI
CCR9 MFI
CXCR3 MFI
Log10 Mean Fluorescence intensity
c
Mild
Severe
CD4 Naive
0.84%
0.58%
CD4 TM
44.2%
43.7%
ANOVA p = 0.0197
CD8 Naive
0.68%
0.84%
CD8 TM
9.62%
20.3%
FSC-A
CCR4 BV650
% CCR4+ of parent population
d
Mild
Severe
CD8 Naive
1.92%
0.24%
ANOVA p = 0.478
CD8 TSCM
46.9%
15.7%
CD8 CM
21.2%
14.0%
CD8 TE*
78.8%
36.0%
MAIT
1.75%
24.3%
FSC-A
TIGIT APC-Cy7
% TIGIT+ of parent population
e
Mild (#4030)
Critical (#4084)
CD8 EM
0.71%
5.93%
CD8 TM
2.71%
3.2%
CD38 BV605
HLA-DR PE-Cy5.5
% CD38+HLA-DR+ of parent
CD8 EM
CD8 TM
f
Mild
11.1%
Severe
1.99%
CD27 APC-R700
IgD BB790
MZ B cells
% of B cells

Figure 3: Potential immune features at baseline predicting COVID-19 severity

a) Flow cytometry data (left) depicts CX3CR1 expression on early NK cells from an individual recovered from mild (top) and severe (bottom) COVID-19. Quantification of mean fluorescence intensity (MFI) of CX3CR1 on early NK cells is shown as boxplot for all study groups.

b) Flow cytometry dot plots on top row (left and middle plot) depicts expression of CCR4 and CCR9 for a mild and severe COVID-19 case. Histogram overlay shows CXCR3 expression for the same cell subset and donors. MFI values for the same receptors are shown as boxplots for all groups (bottom row).

c) Flow cytometry plot depicts expression of CCR4 on $CD4^+$ naïve (top row), $CD4^+$ transitional memory (TM, second row), $CD8^+$ naïve (third row) and $CD8^+$ TM (bottom row) T cells from an individual recovered from mild (left column) or severe (right column) COVID-19. Quantification of these subsets in all study groups are shown as boxplots (right).

d) Flow cytometry plot depicts TIGIT expression on $CD8^+$ naïve (top row), $CD8^+$ stem-cell like memory (TSCM, second row), $CD8^+$ central memory (CM, third row), $CD8^+$ terminal effector* (TE*, fourth row) T cells and MAIT cells (bottom row) from an individual recovered from mild (left column) and severe (right column) COVID-19. Quantification of these subsets in all study groups are shown as boxplots (right).

e) Flow cytometry data (left) depicts CD38 and HLA-DR expression on CD8 effector (EM; top) and terminal (TM; bottom) memory T cells from an individual recovered from mild (left) and critical (right) COVID-19. The gate defines $CD38^+HLA\text{-}DR^+$ activated T cells. Quantification of these subsets in all study groups are shown as boxplots (right).

f) Flow cytometry example data (left) for gating of marginal zone (MZ) B cells from total B cells in an individual recovered from mild and severe COVID-19 is shown. Boxplot (right) shows frequencies of MZ B cells of total B cells in all study groups.

Residuals from linear regression between immune trait and age were used to calculate statistics on age-corrected data. ANOVA with subsequent Wilcoxon test and Bonferroni correction on residuals was performed for statistics highlighted in boxplots. * $P < 0.05$, ** $P < 0.01$, *** $P < 0.001$, **** $P < 0.0001$

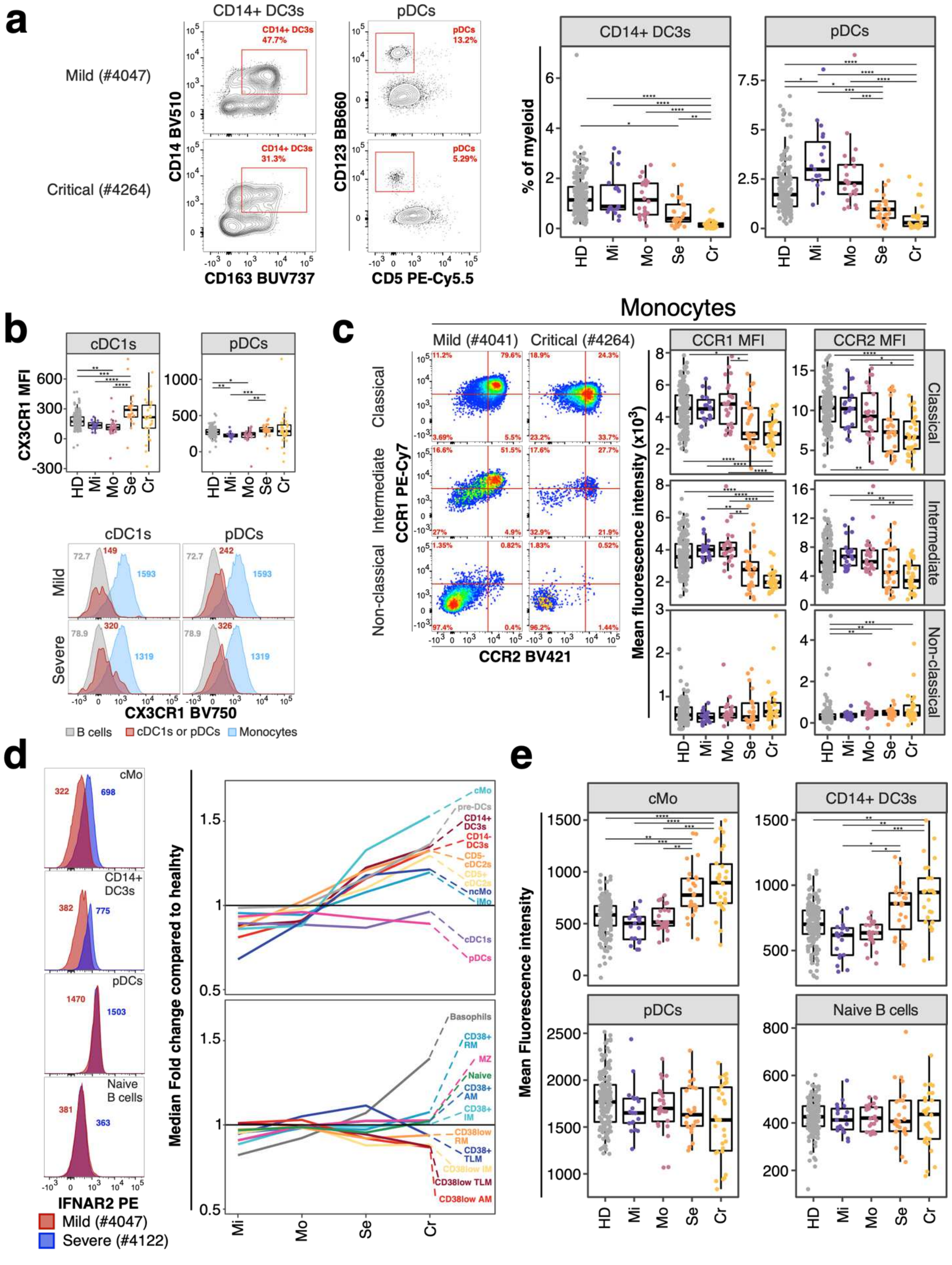
a
CD14+ DC3s
pDCs
Mild (#4047)
Critical (#4264)
CD14 BV510
CD163 BUV737
CD14+ DC3s 47.7%
CD14+ DC3s 31.3%
CD123 BB660
CD5 PE-Cy5.5
pDCs 13.2%
pDCs 5.29%
% of myeloid
HD
Mi
Mo
Se
Cr
b
cDC1s
pDCs
CX3CR1 MFI
cDC1s
pDCs
Mild
Severe
72.7
149
1593
242
78.9
320
1319
326
CX3CR1 BV750
B cells
cDC1s or pDCs
Monocytes
c
Monocytes
Mild (#4041)
Critical (#4264)
Classical
Intermediate
Non-classical
CCR1 PE-Cy7
CCR2 BV421
CCR1 MFI
CCR2 MFI
Mean fluorescence intensity (x10³)
d
cMo
322
698
CD14+ DC3s
382
775
pDCs
1470
1503
Naive B cells
381
363
IFNAR2 PE
Mild (#4047)
Severe (#4122)
Median Fold change compared to healthy
cMo
pre-DCs
CD14+ DC3s
CD14- DC3s
CD5- cDC2s
CD5+ cDC2s
ncMo
iMo
cDC1s
pDCs
Basophils
CD38+ RM
MZ
Naive
CD38+ AM
CD38+ IM
CD38low RM
CD38+ TLM
CD38low IM
CD38low TLM
CD38low AM
e
cMo
CD14+ DC3s
pDCs
Naive B cells
Mean Fluorescence intensity

Figure 4: Innate immune signatures predict COVID-19 severity

a) Example flow cytometry data for frequencies of pDCs from myeloid cells and inflammatory CD14$^+$ DC3s of total DC3s is shown from an individual recovered from mild (top) and critical (bottom) COVID-19. Corresponding enumeration for all subjects based on study group are shown as boxplots (right). Precise delineation of pDCs is shown in Supplementary Data 1.

b) Mean fluorescence intensity (MFI) of CX3CR1 on cDC1s (left) and pDCs (right) is shown for all study groups as boxplot (top row). Example flow cytometry data for CX3CR1 signal (red peak) on cDC1s (first column) and pDCs (second column) is shown as histogram for an individual recovered from mild (top row) and severe (bottom row) COVID-19. B cells (grey) and Monocytes (blue) are overlaid as reference populations known to lack and express CX3CR1, respectively. Numbers in histogram plots highlight MFI.

c) Flow cytometry data (left) depicts CCR1 and CCR2 expression on classical (top), intermediate (middle) and non-classical (bottom) monocytes from a patient recovered from mild (left column) and critical (right column) COVID-19. Boxplots (right) show MFI values of CCR1 (first column) and CCR2 (second column) on the same monocyte populations for all study groups.

d) Expression of IFNAR2 from an individual recovered from mild (red) and severe (blue) COVID-19 is shown as overlaid histogram (left) for classical monocytes (top), CD14$^+$ DC3s (second row), pDCs (third row) and naïve B cells (bottom). Plot on the right depicts fold change of median IFNAR2 expression of each disease severity group compared to median IFNAR2 expression of healthy individuals on all defined myeloid (top) and non-myeloid (bottom) subsets.

e) Boxplots show IFNAR2 MFI for all study groups for classical monocytes, CD14+ DC3s, pDCs and naïve B cells.

Residuals from linear regression between immune trait and age were used to calculate statistics on age-corrected data. ANOVA with subsequent Wilcoxon test and Bonferroni correction on residuals was performed for statistics highlighted in boxplots. * $P < 0.05$, ** $P < 0.01$, *** $P < 0.001$, **** $P < 0.0001$

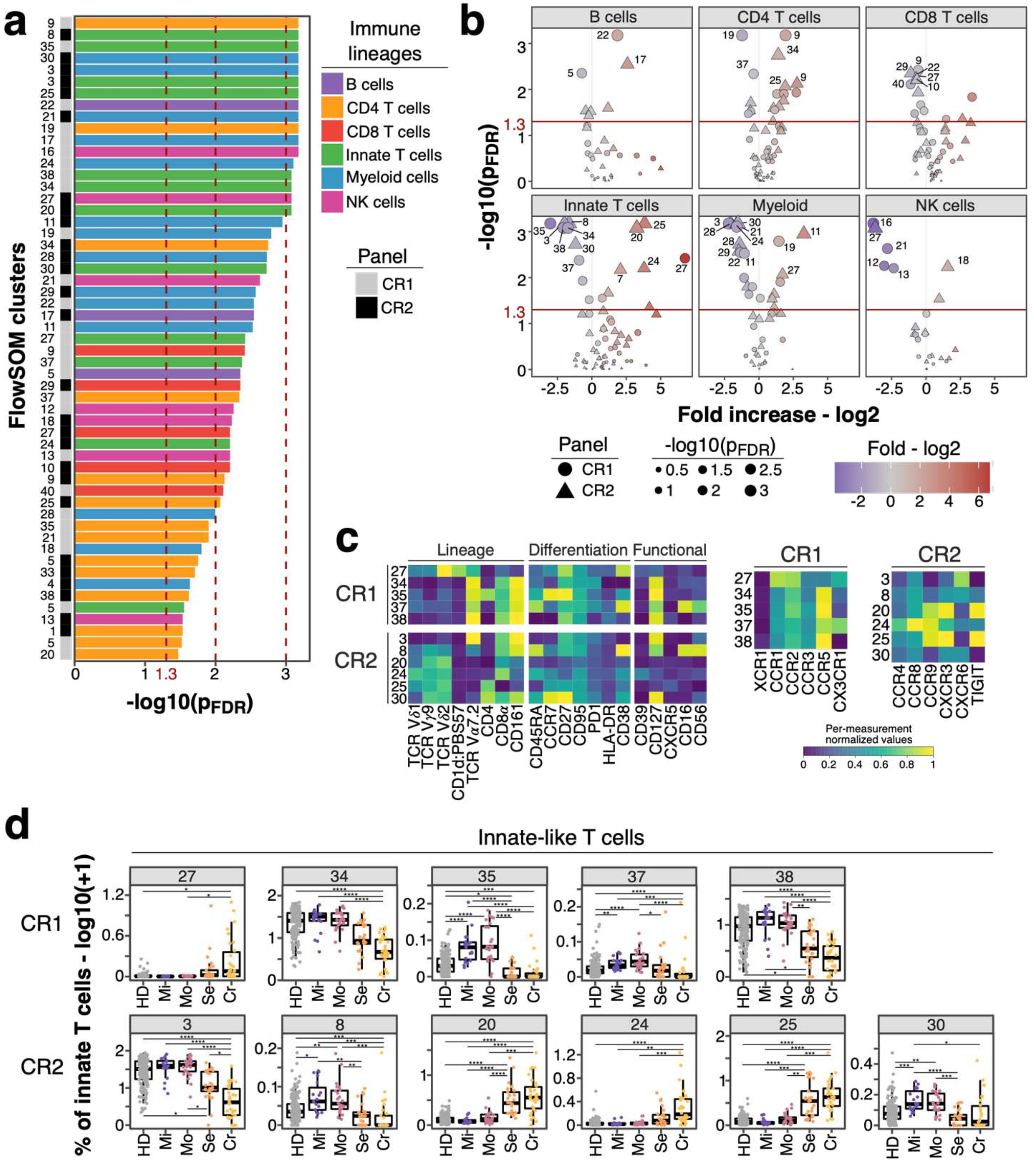
a
FlowSOM clusters
9
8
35
30
3
3
25
22
21
19
17
16
24
38
34
27
20
11
19
34
28
30
21
29
22
17
11
27
9
37
5
29
37
12
18
27
24
13
10
9
40
25
28
35
21
18
5
33
4
38
5
13
1
5
20
0
1
1.3
2
3
-log10(pFDR)
Immune lineages
B cells
CD4 T cells
CD8 T cells
Innate T cells
Myeloid cells
NK cells
Panel
CR1
CR2
b
B cells
CD4 T cells
CD8 T cells
Innate T cells
Myeloid
NK cells
-log10(pFDR)
1.3
Fold increase - log2
-2.5
0
2.5
5
Panel
CR1
CR2
-log10(pFDR)
0.5
1
1.5
2
2.5
3
Fold - log2
-2
0
2
4
6
c
Lineage
Differentiation
Functional
CR1
27
34
35
37
38
CR2
3
8
20
24
25
30
TCR Vδ1
TCR Vγ9
TCR Vδ2
CD1d:PBS57
TCR Vα7.2
CD4
CD8α
CD161
CD45RA
CCR7
CD27
CD95
PD1
HLA-DR
CD38
CD39
CD127
CXCR5
CD16
CD56
CR1
XCR1
CCR1
CCR2
CCR3
CCR5
CX3CR1
CR2
CCR4
CCR8
CCR9
CXCR3
CXCR6
TIGIT
Per-measurement normalized values
0
0.2
0.4
0.6
0.8
1
d
Innate-like T cells
CR1
CR2
% of innate T cells - log10(+1)
27
34
35
37
38
3
8
20
24
25
30
HD
Mi
Mo
Se
Cr

Figure 5: Unsupervised analysis of immune system in individuals recovered from non-severe and severe COVID-19

a) FDR-adjusted -log10 P-values of FlowSOM clusters (N = 55) which differ significantly ($P < 0.05$) between individuals recovered from non-severe (mild/moderate) and severe (severe/critical) COVID-19 are shown. Bars are colored based on lineage (B cells, purple; CD4 T cells, orange; CD8 T cells, red; innate-like T cells, green; myeloid cells, blue; NK cells, pink). Bar on the left indicates whether traits originate from chemokine receptor panel 1 (CR1, grey) or 2 (CR2, black).

b) Volcano plots show FDR-adjusted -log10 P-values and log2 fold change derived from comparison of FlowSOM clusters between individuals recovered from non-severe and severe COVID-19 cases. Main lineages are depicted in separated plots and contain FlowSOM clusters from both panels CR1 (circle) and CR2 (triangle). Data point size corresponds to -log10 P-values and color indicates log2 fold change.

c) Heatmap depicts normalized median fluorescence intensity (MFI) values for lineage, differentiation and functional markers from top significant innate-like T cell clusters (Fig. 5a, $P < 0.01$). Values derived from CR1 (top) and CR2 (bottom) panels are separated. Heatmaps on the right highlight expression of markers specific for CR1 and CR2 panels including chemokine receptors, co-stimulatory markers and IFNAR2. Values are normalized based on trimmed 1-99% percentile values. Complete heatmaps for all innate-like T cell clusters are shown in Supplementary Data 12.

d) Frequencies for same clusters described in Figure 5c are shown as boxplots based on study group. Values are log10(+ 1) transformed and plotted on linear scale.

Logistic regression with correction for age and experiment batch was used to identify significant clusters between non-severe and severe COVID-19. Only FlowSOM clusters (N = 291) which did not show temporal changes within moderate and severe COVID-19 cases are shown as described in the Online methods section and results (Extended Data Fig. 5a). Residuals from linear regression between immune trait and age were used to calculate statistics on age-corrected data. ANOVA with subsequent Wilcoxon test and Bonferroni correction on residuals was performed for statistics highlighted in boxplots. * $P < 0.05$, ** $P < 0.01$, *** $P < 0.001$, **** $P < 0.0001$

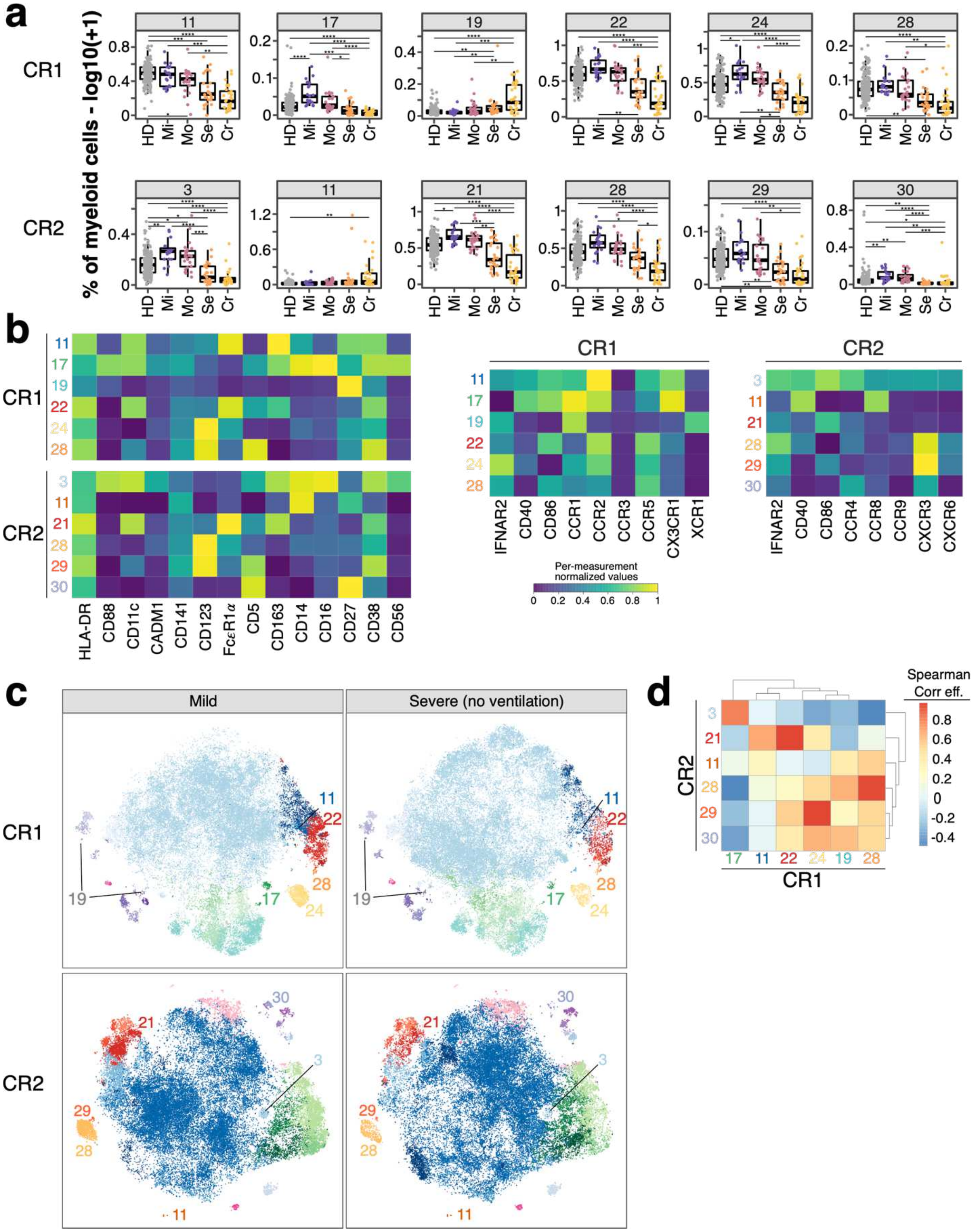
a
CR1
CR2
% of myeloid cells - log10(+1)
11
17
19
22
24
28
3
21
29
30
HD
Mi
Mo
Se
Cr
b
HLA-DR
CD88
CD11c
CADM1
CD141
CD123
FcεR1α
CD5
CD163
CD14
CD16
CD27
CD38
CD56
IFNAR2
CD40
CD86
CCR1
CCR2
CCR3
CCR5
CX3CR1
XCR1
CCR4
CCR8
CCR9
CXCR3
CXCR6
Per-measurement normalized values
0
0.2
0.4
0.6
0.8
1
c
Mild
Severe (no ventilation)
d
Spearman Corr eff.
0.8
0.6
0.4
0.2
0
-0.2
-0.4

Figure 6: Myeloid cell populations from FlowSOM analysis as potential predictor for disease outcome

a) Frequencies (log10 +1) of myeloid cell clusters among top hits ($P < 0.01$) described in Figure 5a are shown for CR1 (top row) and CR2 panel (bottom row). Values are log10(+ 1) transformed and plotted on linear scale. Residuals from linear regression between immune trait and age were used to calculate statistics on age-corrected data. ANOVA with subsequent Wilcoxon test and Bonferroni correction on residuals was performed for statistics highlighted in boxplots. * $P < 0.05$, ** $P < 0.01$, *** $P < 0.001$, **** $P < 0.0001$

b) Heatmaps showing normalized median fluorescence intensity (MFI) values for clusters described in Figure 6a are shown. Heatmaps on the left show markers used to delineate immune cell subsets. On the right, heatmaps depict CR panel-specific markers. Values are normalized based on trimmed 1-99% percentile values.

c) tSNE plots with myeloid cells from individuals recovered from mild (left column) or severe (right column) COVID-19 are shown. Data from panels CR1 and CR2 are shown in the top and bottom row, respectively. Each plot contains 50’000 subsampled myeloid cells (gating shown in Supplementary Data 1). Dots are colored based on FlowSOM cluster annotation and full data is shown in Supplementary Data 9. Clusters described in Figs. 6a and b are annotated and highlighted.

d) Spearman analysis of normalized MFI values between clusters described in Figure 6a is shown in order to estimate the phenotypic overlap between CR1 and CR2 panel. Heatmap depicts Spearman correlation coefficient.

Extended Data Figures

Title: Immune phenotypes that predict COVID-19 severity

Thomas Liechti[1], Yaser Iftikhar[1], Massimo Mangino[2,3], Margaret Beddall[1], Charles W. Goss[4], Jane A. O'Halloran[5], Philip Mudd[6], Mario Roederer[1]

[1]ImmunoTechnology Section, Vaccine Research Center, NIAID, NIH, USA
[2]Department of Twin Research & Genetic Epidemiology, King's College of London, London, UK
[3] NIHR Biomedical Research Centre at Guy's and St Thomas' Foundation Trust, London SE1 9RT, UK
[4]Division of Biostatistics, Washington University School of Medicine, St. Louis, MO, USA,
[5]Division of Infectious Diseases, Department of Internal Medicine, Washington University School of Medicine, St. Louis, MO, USA
[6]Department of Emergency Medicine, Washington University School of Medicine, St. Louis, MO, USA

Keywords

SARS-CoV2, COVID-19, Immunophenotyping, Chemokine Receptors, High-dimensional flow cytometry

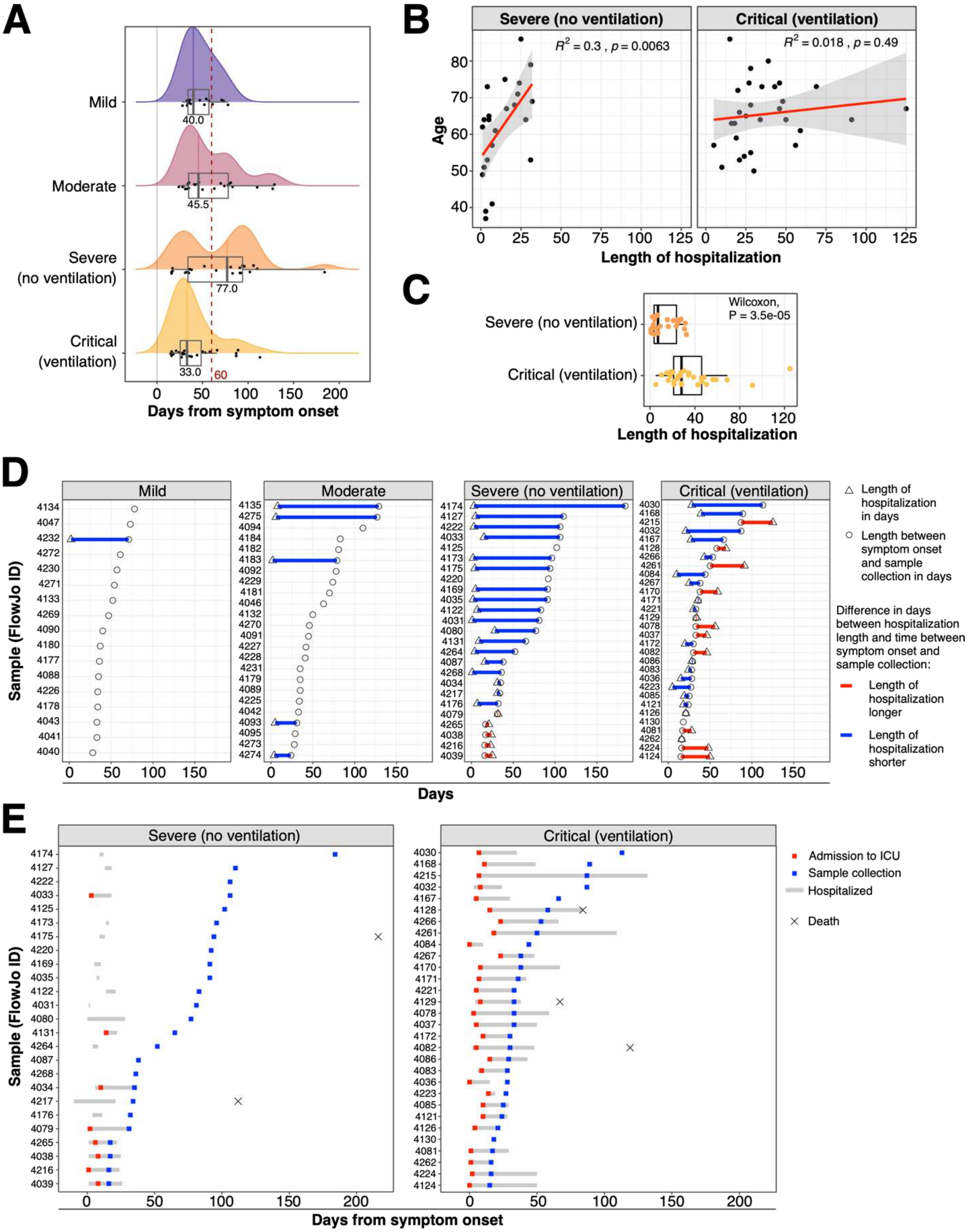
A
Mild
Moderate
Severe (no ventilation)
Critical (ventilation)
40.0
45.5
77.0
33.0
60
0
50
100
150
200
Days from symptom onset
B
Severe (no ventilation)
Critical (ventilation)
$R^2 = 0.3$, $p = 0.0063$
$R^2 = 0.018$, $p = 0.49$
Age
40
50
60
70
80
0
25
50
75
100
125
Length of hospitalization
C
Severe (no ventilation)
Critical (ventilation)
Wilcoxon, P = 3.5e-05
0
40
80
120
Length of hospitalization
D
Mild
Moderate
Severe (no ventilation)
Critical (ventilation)
Sample (FlowJo ID)
Days
0
50
100
150
△ Length of hospitalization in days
○ Length between symptom onset and sample collection in days
Difference in days between hospitalization length and time between symptom onset and sample collection:
Length of hospitalization longer
Length of hospitalization shorter
4134
4047
4232
4272
4230
4271
4133
4269
4090
4180
4177
4088
4226
4178
4043
4041
4040
4135
4275
4094
4184
4182
4183
4092
4229
4181
4046
4132
4270
4091
4227
4228
4231
4179
4089
4225
4042
4093
4095
4273
4274
4174
4127
4222
4033
4125
4173
4175
4220
4169
4035
4122
4031
4080
4131
4264
4087
4268
4034
4217
4176
4079
4265
4038
4216
4039
4030
4168
4215
4032
4167
4128
4266
4261
4084
4267
4170
4171
4221
4129
4078
4037
4172
4082
4086
4083
4036
4223
4085
4121
4126
4130
4081
4262
4224
4124
E
Severe (no ventilation)
Critical (ventilation)
Sample (FlowJo ID)
Days from symptom onset
0
50
100
150
200
Admission to ICU
Sample collection
Hospitalized
× Death

Extended Data Figure 1: Cohorts and timing of sample collection

a) Distribution of days between symptom onset and sample collection is shown as histograms and boxplots for individuals recovered from mild, moderate, severe and critical COVID-19 cases. Individuals are highlighted as dots within boxplot. Red dashed line indicates 60 days cutoff which was used for analysis shown in Figures 1b and 2a and Extended Data Figure 5a. Information about time between symptom onset and sample collection was unavailable for two samples from the mild COVID-19 group.

b) Linear regression between length of hospitalization in days and age is shown for severe and critical COVID-19 cases.

c) Boxplot shows length of hospitalization in days for severe and critical COVID-19 cases. Wilcoxon test was performed to determine significant difference between severe and critical COVID-19 cases.

d) Length of hospitalization in days (x-axis) is shown as triangle and circles highlight length in days between symptom onset and sample collection. Donors are depicted in rows (y-axis). Symbols from hospitalized individuals are connected by colored bar. Blue or red bars highlight if length of hospitalization is shorter or longer, respectively. COVID-19 study groups based on severity are shown separately.

e) Length of hospitalization (grey bar), admission to ICU (red symbol) and sample collection (blue symbol) based on days from symptom onset is shown for severe and critical COVID-19 cases. Death is indicated by cross.

	Healthy	Mild	Moderate	Severe (no ventilation)	Critical (ventilation)
Samples (N)	173	19	24	25	30
Age median (IQR)	50 (36-60)	39 (33.5-49)	50.5 (32-59)	64 (51-69)	64.5 (57.5-72.75)
Age range	18-70	26-59	22-77	37-86	43-86
Gender (F/M)	76 / 97	7 / 12	13 / 11	9 / 16	11 / 18*
Median days between symptom onset and sample collection (IQR)	NA	40 (34-57)	45.5 (34.75-78.25)	77 (34-94)	33 (25.5-48.5)
Range days between symptom onset and sample collection	NA	28-78	24-129	16-184	15-113
Hospitalized (N)	NA	1	5	23	30
Median days hospitalized (IQR)	NA	2	5 (4-6)	7 (3.5-23.5)	28 (21-46)
Range days hospitalized	NA	2	2-8	1-32	5-125
ICU (N)	NA	NA	NA	8	30

* Gender information not available for one individual.

Extended Data Figure 2: Demographics summary

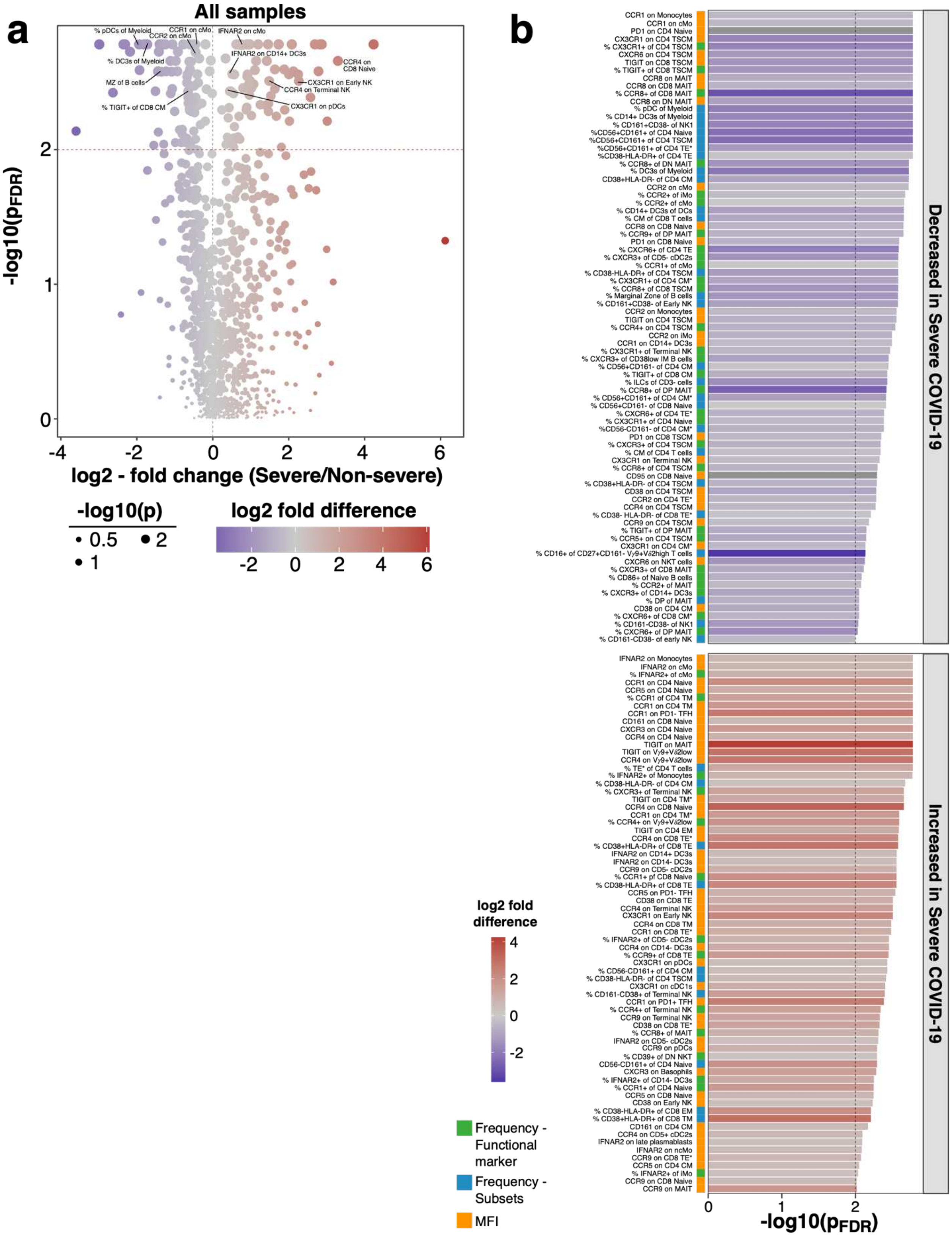
a
All samples
% pDCs of Myeloid
CCR1 on cMo
CCR2 on cMo
IFNAR2 on cMo
% DC3s of Myeloid
IFNAR2 on CD14+ DC3s
CCR4 on CD8 Naive
MZ of B cells
CX3CR1 on Early NK
CCR4 on Terminal NK
% TIGIT+ of CD8 CM
CX3CR1 on pDCs
-log10(pFDR)
2
1
0
-4
-2
0
2
4
6
log2 - fold change (Severe/Non-severe)
-log10(p)
0.5
1
2
log2 fold difference
-2
0
2
4
6
b
CCR1 on Monocytes
CCR1 on cMo
PD1 on CD4 Naive
CX3CR1 on CD4 TSCM
% CX3CR1+ of CD4 TSCM
CXCR6 on CD4 TSCM
TIGIT on CD8 TSCM
% TIGIT+ of CD8 TSCM
CCR8 on MAIT
CCR8 on CD8 MAIT
% CCR8+ of CD8 MAIT
CCR8 on DN MAIT
% pDC of Myeloid
% CD14+ DC3s of Myeloid
% CD161+CD38- of NK1
%CD56+CD161+ of CD4 Naive
%CD56+CD161+ of CD4 TSCM
%CD56+CD161+ of CD4 TE*
%CD38-HLA-DR+ of CD4 TE
% CCR8+ of DN MAIT
% DC3s of Myeloid
CD38+HLA-DR- of CD4 CM
CCR2 on cMo
% CCR2+ of iMo
% CCR2+ of cMo
% CD14+ DC3s of DCs
% CM of CD8 T cells
CCR8 on CD8 Naive
% CCR9+ of DP MAIT
PD1 on CD8 Naive
% CXCR6+ of CD4 TE
% CXCR3+ of CD5- cDC2s
% CCR1+ of cMo
% CD38-HLA-DR+ of CD4 TSCM
% CX3CR1+ of CD4 CM*
% CCR8+ of CD8 TSCM
% Marginal Zone of B cells
% CD161+CD38- of Early NK
CCR2 on Monocytes
TIGIT on CD4 TSCM
% CCR4+ on CD4 TSCM
CCR2 on iMo
CCR1 on CD14+ DC3s
% CX3CR1+ of Terminal NK
% CXCR3+ of CD38low IM B cells
% CD56+CD161- of CD4 CM
% TIGIT+ of CD8 CM
% ILCs of CD3- cells
% CCR8+ of DP MAIT
% CD56+CD161+ of CD4 CM*
% CD56+CD161- of CD8 Naive
% CXCR6+ of CD4 TE*
% CX3CR1+ of CD4 Naive
%CD56-CD161- of CD4 CM*
PD1 on CD8 TSCM
% CXCR3+ of CD4 TSCM
% CM of CD4 T cells
CX3CR1 on Terminal NK
% CCR8+ of CD4 TSCM
CD95 on CD8 Naive
% CD38+HLA-DR- of CD4 TSCM
CD38 on CD4 TSCM
CCR2 on CD4 TE*
CCR4 on CD4 TSCM
% CD38- HLA-DR- of CD8 TE*
CCR9 on CD4 TSCM
% TIGIT+ of DP MAIT
% CCR5+ on CD4 TSCM
CX3CR1 on CD4 CM*
% CD16+ of CD27+CD161- Vγ9+Vδ2high T cells
CXCR6 on NKT cells
% CXCR3+ of CD8 MAIT
% CD86+ of Naive B cells
% CCR2+ of MAIT
% CXCR3+ of CD14+ DC3s
% DP of MAIT
CD38 on CD4 CM
% CXCR6+ of CD8 CM*
% CD161-CD38- of NK1
% CXCR6+ of DP MAIT
% CD161-CD38- of early NK
Decreased in Severe COVID-19
IFNAR2 on Monocytes
IFNAR2 on cMo
% IFNAR2+ of cMo
CCR1 on CD4 Naive
CCR5 on CD4 Naive
% CCR1 of CD4 TM
CCR1 on CD4 TM
CCR1 on PD1- TFH
CD161 on CD8 Naive
CXCR3 on CD4 Naive
CCR4 on CD4 Naive
TIGIT on MAIT
TIGIT on Vγ9+Vδ2low
CCR4 on Vγ9+Vδ2low
% TE* of CD4 T cells
% IFNAR2+ of Monocytes
% CD38-HLA-DR- of CD4 CM
% CXCR3+ of Terminal NK
TIGIT on CD4 TM*
CCR4 on CD8 Naive
CCR1 on CD4 TM*
% CCR4+ on Vγ9+Vδ2low
TIGIT on CD4 EM
CCR4 on CD8 TE*
% CD38+HLA-DR+ of CD8 TE
IFNAR2 on CD14+ DC3s
IFNAR2 on CD14- DC3s
CCR9 on CD5- cDC2s
% CCR1+ pf CD8 Naive
% CD38-HLA-DR+ of CD8 TE
CCR5 on PD1- TFH
CD38 on CD8 TE
CCR4 on Terminal NK
CX3CR1 on Early NK
CCR4 on CD8 TM
CCR1 on CD8 TE*
% IFNAR2+ of CD5- cDC2s
CCR4 on CD14- DC3s
% CCR9+ of CD8 TE
CX3CR1 on pDCs
% CD56-CD161+ of CD4 CM
% CD38-HLA-DR- of CD4 TSCM
CX3CR1 on cDC1s
% CD161-CD38+ of Terminal NK
CCR1 on PD1+ TFH
% CCR4+ of Terminal NK
CCR9 on Terminal NK
CD38 on CD8 TE*
% CCR8+ of MAIT
IFNAR2 on CD5- cDC2s
CCR9 on pDCs
% CD39+ of DN NKT
CD56-CD161+ of CD4 Naive
CXCR3 on Basophils
% IFNAR2+ of CD14- DC3s
% CCR1+ of CD4 Naive
CCR5 on CD8 Naive
CD38 on Early NK
% CD38-HLA-DR+ of CD8 EM
% CD38+HLA-DR+ of CD8 TM
CD161 on CD4 CM
CCR4 on CD5+ cDC2s
IFNAR2 on late plasmablasts
IFNAR2 on ncMo
CCR9 on CD8 TE*
CCR5 on CD4 CM
% IFNAR2+ of iMo
CCR9 on CD8 Naive
CCR9 on MAIT
Increased in Severe COVID-19
0
1
2
-log10(pFDR)
log2 fold difference
4
2
0
-2
Frequency - Functional marker
Frequency - Subsets
MFI

Extended Data Figure 3: Comparison of individuals recovered from non-severe and severe COVID-19

a) Volcano plot shows comparison of individuals recovered from non-severe (mild/moderate) and severe (severe/critical) COVID-19. P-values were obtained from logistic regression, included correction for age and experiment and were corrected for multiple testing using Benjamini-Hochberg false discovery rate. Log2 fold change was calculated based on the mean of immune traits within non-severe and severe COVID-19 cases. P-values are shown as -log10.

b) Bar graph shows FDR-adjusted -log10 P-values for significant immune traits with P < 0.01 derived from Extended Data Figure 3a. Bars are colored based on log2 fold change and split based on decrease (top) or increase (bottom) in individuals recovered from severe COVID-19. Bar on the left indicates trait type.

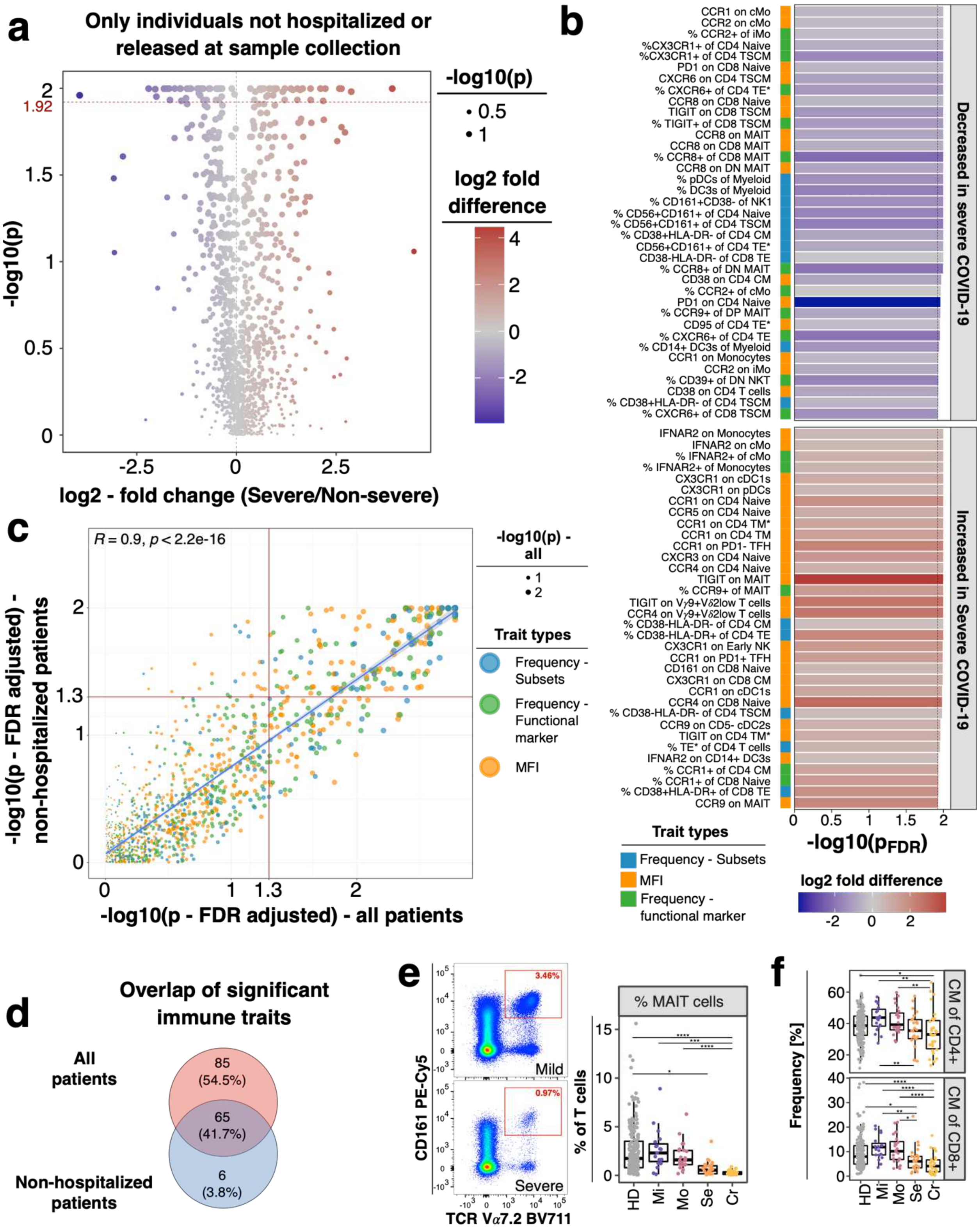
a
Only individuals not hospitalized or released at sample collection
-log10(p)
2
1.92
1.5
1
0.5
0
-2.5
0
2.5
log2 - fold change (Severe/Non-severe)
-log10(p)
0.5
1
log2 fold difference
4
2
0
-2
b
CCR1 on cMo
CCR2 on cMo
% CCR2+ of iMo
%CX3CR1+ of CD4 Naive
%CX3CR1+ of CD4 TSCM
PD1 on CD8 Naive
CXCR6 on CD4 TSCM
% CXCR6+ of CD4 TE*
CCR8 on CD8 Naive
TIGIT on CD8 TSCM
% TIGIT+ of CD8 TSCM
CCR8 on MAIT
CCR8 on CD8 MAIT
% CCR8+ of CD8 MAIT
CCR8 on DN MAIT
% pDCs of Myeloid
% DC3s of Myeloid
% CD161+CD38- of NK1
% CD56+CD161+ of CD4 Naive
% CD56+CD161+ of CD4 TSCM
% CD38+HLA-DR- of CD4 CM
CD56+CD161+ of CD4 TE*
CD38-HLA-DR- of CD8 TE
% CCR8+ of DN MAIT
CD38 on CD4 CM
% CCR2+ of cMo
PD1 on CD4 Naive
% CCR9+ of DP MAIT
CD95 of CD4 TE*
% CXCR6+ of CD4 TE
% CD14+ DC3s of Myeloid
CCR1 on Monocytes
CCR2 on iMo
% CD39+ of DN NKT
CD38 on CD4 T cells
% CD38+HLA-DR- of CD4 TSCM
% CXCR6+ of CD8 TSCM
Decreased in severe COVID-19
IFNAR2 on Monocytes
IFNAR2 on cMo
% IFNAR2+ of cMo
% IFNAR2+ of Monocytes
CX3CR1 on cDC1s
CX3CR1 on pDCs
CCR1 on CD4 Naive
CCR5 on CD4 Naive
CCR1 on CD4 TM*
CCR1 on CD4 TM
CCR1 on PD1- TFH
CXCR3 on CD4 Naive
CCR4 on CD4 Naive
TIGIT on MAIT
% CCR9+ of MAIT
TIGIT on Vγ9+Vδ2low T cells
CCR4 on Vγ9+Vδ2low T cells
% CD38-HLA-DR- of CD4 CM
% CD38-HLA-DR+ of CD4 TE
CX3CR1 on Early NK
CCR1 on PD1+ TFH
CD161 on CD8 Naive
CX3CR1 on CD8 CM
CCR1 on cDC1s
CCR4 on CD8 Naive
% CD38-HLA-DR- of CD4 TSCM
CCR9 on CD5- cDC2s
TIGIT on CD4 TM*
% TE* of CD4 T cells
IFNAR2 on CD14+ DC3s
% CCR1+ of CD4 CM
% CCR1+ of CD8 Naive
% CD38+HLA-DR+ of CD8 TE
CCR9 on MAIT
Increased in Severe COVID-19
0
0.5
1
1.5
2
-log10(pFDR)
Trait types
Frequency - Subsets
MFI
Frequency - functional marker
log2 fold difference
-2
0
2
c
R = 0.9, p < 2.2e-16
-log10(p - FDR adjusted) - non-hospitalized patients
2
1.3
1
0
0
1
1.3
2
-log10(p - FDR adjusted) - all patients
-log10(p) - all
1
2
Trait types
Frequency - Subsets
Frequency - Functional marker
MFI
d
Overlap of significant immune traits
All patients
85 (54.5%)
65 (41.7%)
6 (3.8%)
Non-hospitalized patients
e
CD161 PE-Cy5
TCR Vα7.2 BV711
3.46%
Mild
0.97%
Severe
% MAIT cells
% of T cells
15
10
5
0
HD
Mi
Mo
Se
Cr
f
Frequency [%]
60
40
20
CM of CD4+
40
30
20
10
0
CM of CD8+
HD
Mi
Mo
Se
Cr

Extended Data Figure 4: Comparison of analysis between all and non-hospitalized individuals at time of sample collection

a) Volcano plot shows comparison of individuals recovered from non-severe (mild/moderate) and severe (severe/critical) COVID-19. Only individuals not hospitalized or discharged at day of sample collection are included. P-values were obtained from logistic regression, included correction for age and experiment and were corrected for multiple testing using Benjamini-Hochberg false discovery rate. Log2 fold change was calculated based on the mean of immune traits within non-severe and severe COVID-19 cases. P-values are shown as -log10.

b) Bar graph shows FDR-adjusted -log10 P-values for immune traits significantly different between non-severe and severe COVID-19 cases (cut-off for P-value < 0.012). Plot is similar to Extended Data Figure 3b but depicts P-values obtained with only individuals not hospitalized or released at day of sample collection. Bar on the left indicates the immune trait type. Color of bars indicate log2 fold change between non-severe and severe COVID-19 cases calculated as the ratio between the mean of immune traits between the two severity groups.

c) Comparison of stable immune traits between non-severe and severe COVID-19 cases including either all individuals (x-axis) or only individuals not hospitalized or released at day of sample collection (y-axis) is shown. Plot shows FDR-adjusted -log10 P-values for manually gated immune traits (N = 801). P-values were obtained by logistic regression and corrected for age and experiment batch. Size of symbols is based on -log10 P-values from analysis including all individuals. Color depicts the type of trait.

d) Venn graph depicts overlap of immune traits which differed between non-severe and severe COVID-19 group obtained from analysis including all (red circle, traits from Extended Data Fig. 3b) or only non-hospitalized individuals (blue circle, traits from Extended Data Fig. 4b).

e) Example flow cytometry data and gating of MAIT cells is shown (left) for one donor recovered from mild and severe COVID-19. Boxplot (right) shows frequency of MAIT cells per group. More detailed gating information is shown in Supplementary Data 3.

f) Boxplots show frequencies of CD4 (top) and CD8 (bottom) central memory (CM) cells of conventional CD4 and CD8 T cells, respectively, from all study groups.

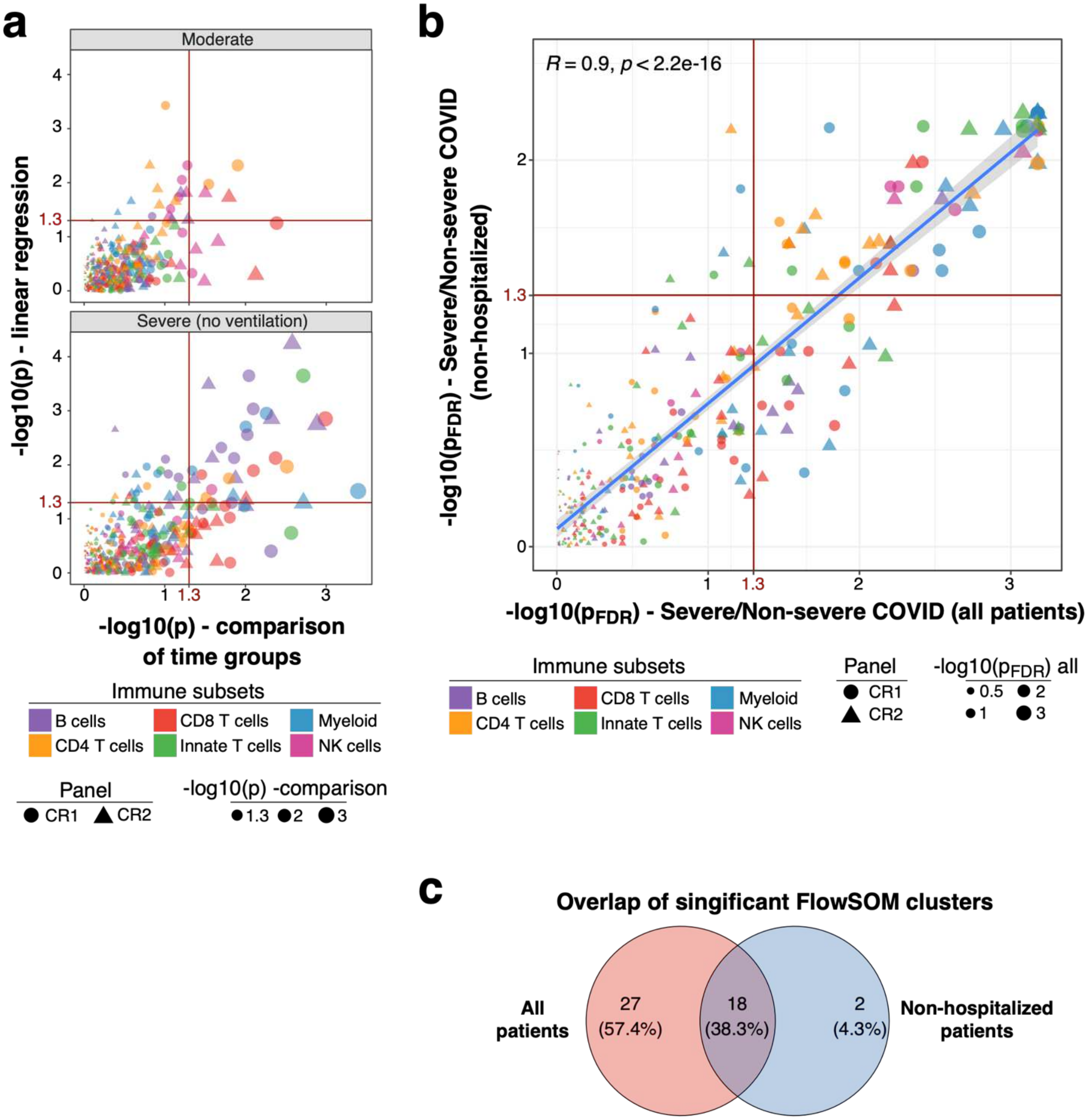
a
Moderate
Severe (no ventilation)
-log10(p) - linear regression
-log10(p) - comparison of time groups
0
1
1.3
2
3
4
Immune subsets
B cells
CD4 T cells
CD8 T cells
Innate T cells
Myeloid
NK cells
Panel
CR1
CR2
-log10(p) -comparison
1.3
2
3
b
R = 0.9, p < 2.2e-16
-log10(pFDR) - Severe/Non-severe COVID (non-hospitalized)
-log10(pFDR) - Severe/Non-severe COVID (all patients)
0
1
1.3
2
3
-log10(pFDR) all
0.5
1
2
3
c
Overlap of singificant FlowSOM clusters
All patients
27 (57.4%)
18 (38.3%)
2 (4.3%)
Non-hospitalized patients

Extended Data Figure 5: Dynamics of FlowSOM clusters in COVID-19

a) FlowSOM clusters affected by long-term perturbations were identified in individuals recovered from moderate (top) or severe COVID-19 (bottom) either by linear regression of cluster frequency and days between symptom onset and sample collection or Wilcoxon analysis of cluster frequency between early and late timepoints (cut-off >60 days between symptom onset and sample collection). -log10 P-values from both analyses are shown for All 388 FlowSOM clusters. P-value cutoff of 0.05 is shown by red line. Symbols are colored based on lineage and shaped based on CR1 (circle) or CR2 (triangle) panel. Symbol size is according to -log10 P-value from Wilcoxon analysis.

b) Graph shows FDR-adjusted -log10 P-values derived from comparison of stable FlowSOM cluster (N = 291) frequencies between individuals recovered from non-severe and severe COVID-19. Analyses included either all individuals (x-axis) and only individuals not hospitalized or released at day of sample collection (y-axis). P-values were obtained by logistic regression correcting for age and experiment batch. Symbols are colored based on lineage and shape corresponds to CR1 or CR2 panel. Symbol size is based on FDR-adjusted -log10 P-value derived from analysis with all individuals.

c) Venn graph shows overlap of significant FlowSOM clusters between individuals recovered from non-severe and severe COVID-19 from analysis including either all individuals (red circle) or only individuals not hospitalized or released at day of sample collection (blue circle).

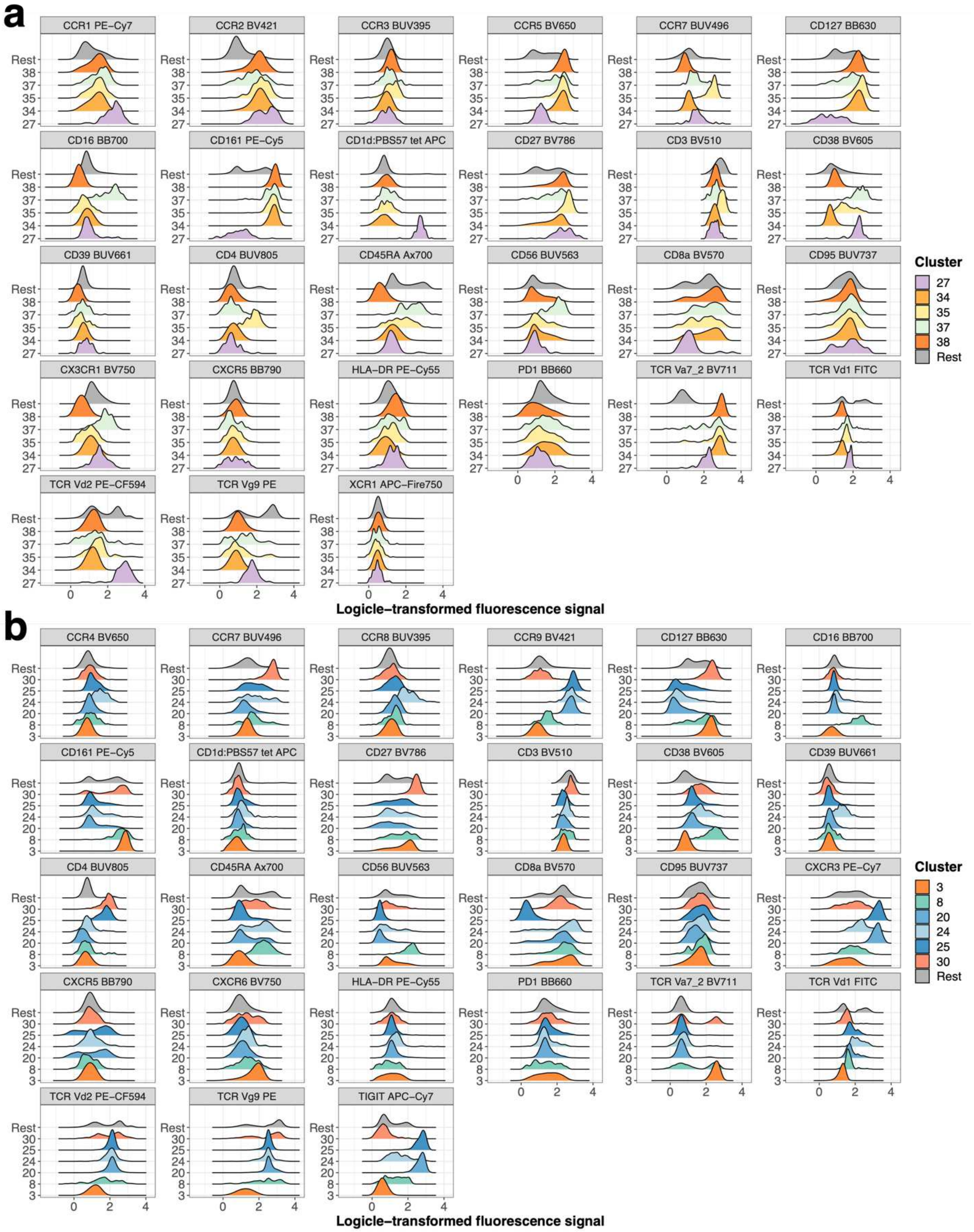
a
CCR1 PE−Cy7
CCR2 BV421
CCR3 BUV395
CCR5 BV650
CCR7 BUV496
CD127 BB630
CD16 BB700
CD161 PE−Cy5
CD1d:PBS57 tet APC
CD27 BV786
CD3 BV510
CD38 BV605
CD39 BUV661
CD4 BUV805
CD45RA Ax700
CD56 BUV563
CD8a BV570
CD95 BUV737
CX3CR1 BV750
CXCR5 BB790
HLA−DR PE−Cy55
PD1 BB660
TCR Va7_2 BV711
TCR Vd1 FITC
TCR Vd2 PE−CF594
TCR Vg9 PE
XCR1 APC−Fire750
Rest
38
37
35
34
27
Cluster
27
34
35
37
38
Rest
0
2
4
Logicle−transformed fluorescence signal
b
CCR4 BV650
CCR7 BUV496
CCR8 BUV395
CCR9 BV421
CD127 BB630
CD16 BB700
CD161 PE−Cy5
CD1d:PBS57 tet APC
CD27 BV786
CD3 BV510
CD38 BV605
CD39 BUV661
CD4 BUV805
CD45RA Ax700
CD56 BUV563
CD8a BV570
CD95 BUV737
CXCR3 PE−Cy7
CXCR5 BB790
CXCR6 BV750
HLA−DR PE−Cy55
PD1 BB660
TCR Va7_2 BV711
TCR Vd1 FITC
TCR Vd2 PE−CF594
TCR Vg9 PE
TIGIT APC−Cy7
Rest
30
25
24
20
8
3
Cluster
3
8
20
24
25
30
Rest
0
2
4
Logicle−transformed fluorescence signal

Extended Data Figure 6: Expression pattern of significant innate-like T cell clusters between non-severe and severe COVID-19

Expression (logicle-transformed fluorescence signal) of markers from CR1 (A) and CR2 (B) panel for innate-like T cell clusters are shown as overlaid histograms. T cell clusters are described in Figure 5c and d and are significantly different between individuals recovered from non-severe and severe COVID-19. All remaining clusters within innate-like T cells are depicted in grey and labeled as “Rest” as a reference population.

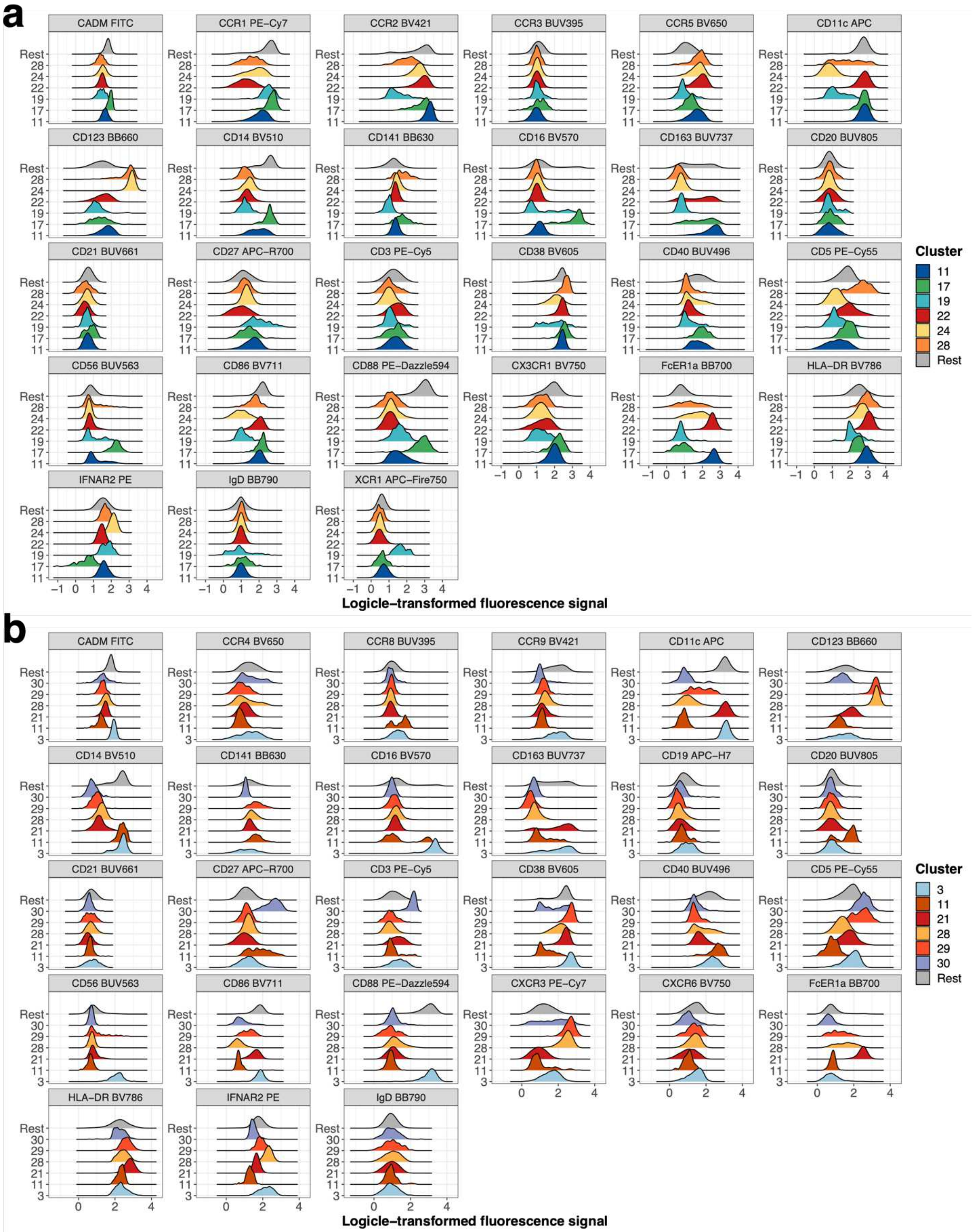
a
CADM FITC
CCR1 PE−Cy7
CCR2 BV421
CCR3 BUV395
CCR5 BV650
CD11c APC
CD123 BB660
CD14 BV510
CD141 BB630
CD16 BV570
CD163 BUV737
CD20 BUV805
CD21 BUV661
CD27 APC−R700
CD3 PE−Cy5
CD38 BV605
CD40 BUV496
CD5 PE−Cy55
CD56 BUV563
CD86 BV711
CD88 PE−Dazzle594
CX3CR1 BV750
FcER1a BB700
HLA−DR BV786
IFNAR2 PE
IgD BB790
XCR1 APC−Fire750
Rest
28
24
22
19
17
11
−1 0 1 2 3 4
Cluster
11
17
19
22
24
28
Rest
Logicle−transformed fluorescence signal
b
CADM FITC
CCR4 BV650
CCR8 BUV395
CCR9 BV421
CD11c APC
CD123 BB660
CD14 BV510
CD141 BB630
CD16 BV570
CD163 BUV737
CD19 APC−H7
CD20 BUV805
CD21 BUV661
CD27 APC−R700
CD3 PE−Cy5
CD38 BV605
CD40 BUV496
CD5 PE−Cy55
CD56 BUV563
CD86 BV711
CD88 PE−Dazzle594
CXCR3 PE−Cy7
CXCR6 BV750
FcER1a BB700
HLA−DR BV786
IFNAR2 PE
IgD BB790
Rest
30
29
28
21
11
3
0 2 4
Cluster
3
11
21
28
29
30
Rest
Logicle−transformed fluorescence signal

Extended Data Figure 7: Expression pattern of significant myeloid cell clusters between non-severe and severe COVID-19

Expression (logicle-transformed fluorescence signal) of markers from CR1 (A) and CR2 (B) panel for myeloid cell clusters are shown as overlaid histograms. Myeloid cell clusters are described in Figure 6 and are significantly different between individuals recovered from non-severe and severe COVID-19. All remaining clusters within myeloid cells are depicted in grey and labeled as “Rest” as a reference population.

Supplementary Data

Title: Immune phenotypes that predict COVID-19 severity

Thomas Liechti[1], Yaser Iftikhar[1], Massimo Mangino[2,3], Margaret Beddall[1], Charles W. Goss[4], Jane A. O'Halloran[5], Philip Mudd[6], Mario Roederer[1]

[1]ImmunoTechnology Section, Vaccine Research Center, NIAID, NIH, USA
[2]Department of Twin Research & Genetic Epidemiology, King's College of London, London, UK
[3] NIHR Biomedical Research Centre at Guy's and St Thomas' Foundation Trust, London SE1 9RT, UK
[4]Division of Biostatistics, Washington University School of Medicine, St. Louis, MO, USA,
[5]Division of Infectious Diseases, Department of Internal Medicine, Washington University School of Medicine, St. Louis, MO, USA
[6]Department of Emergency Medicine, Washington University School of Medicine, St. Louis, MO, USA

Keywords

SARS-CoV2, COVID-19, Immunophenotyping, Chemokine Receptors, High-dimensional flow cytometry

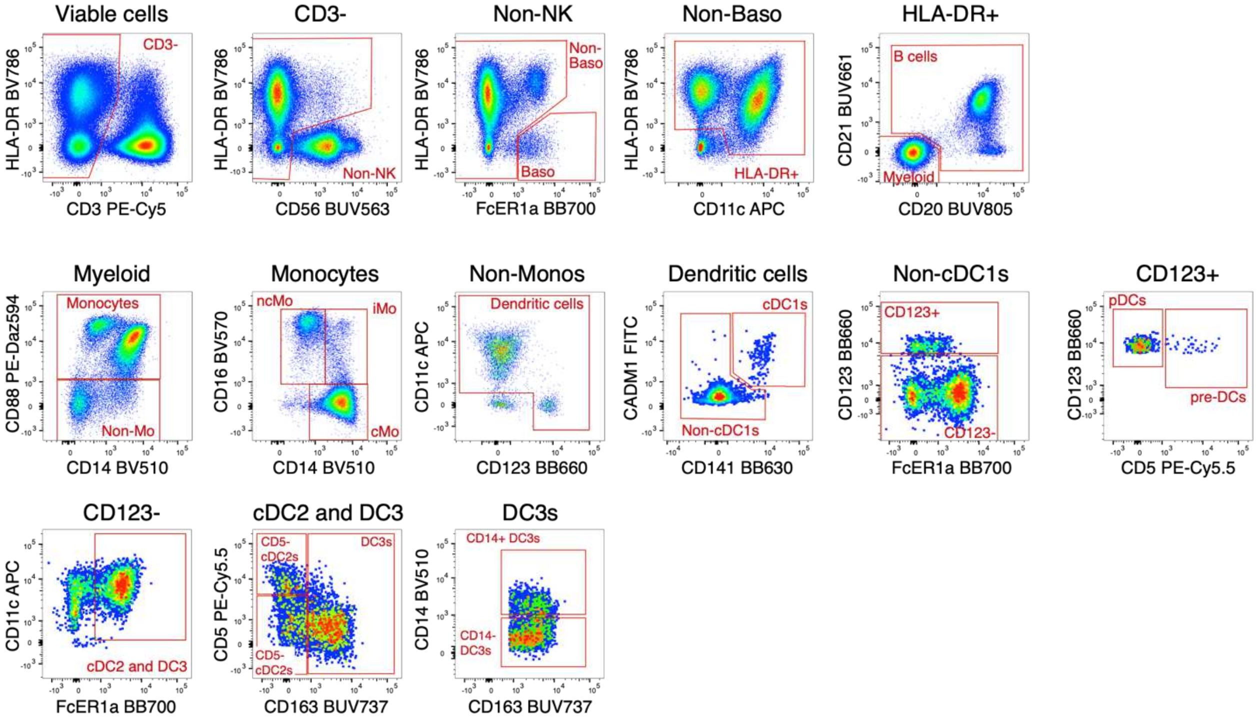

Supplementary Data 1: Gating of myeloid cells (Monocytes/Dendritic cells)

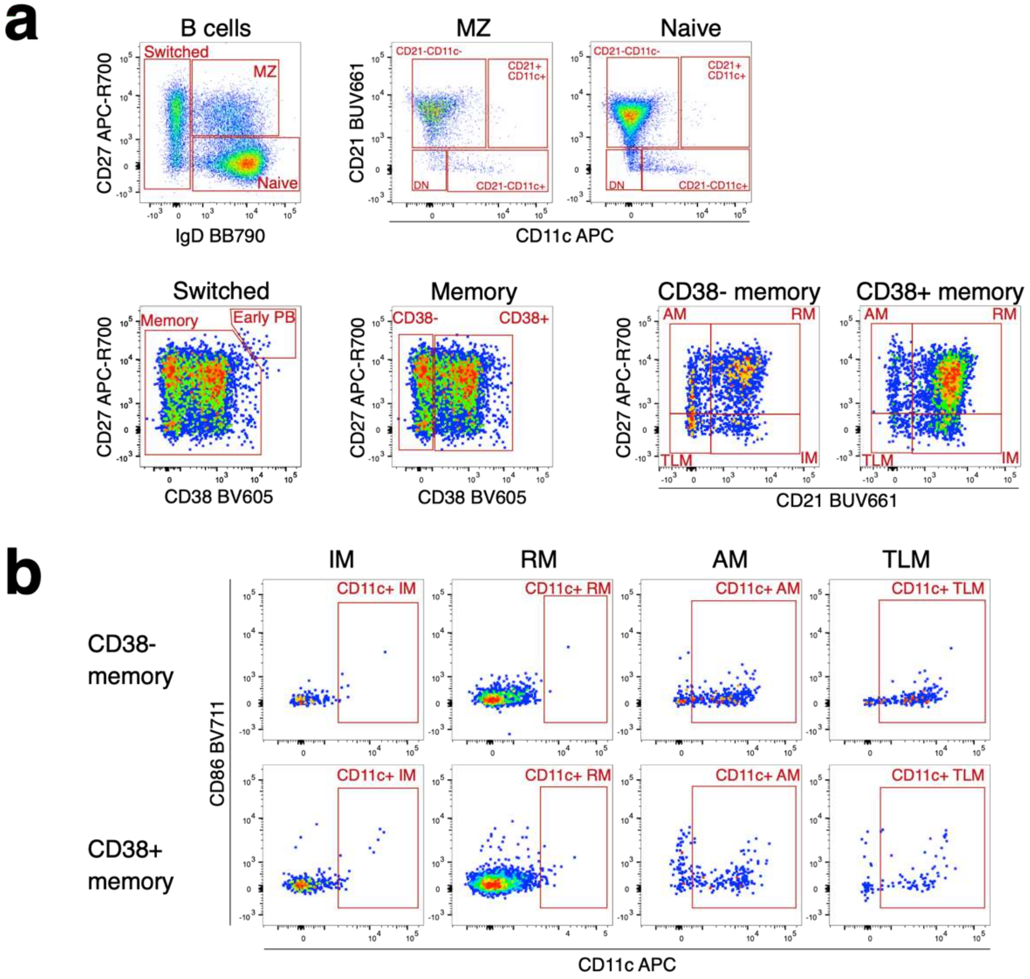

Supplementary Data 2: Gating of B cell subsets

Gating of **a)** B cell subsets and **b)** CD11c$^+$ B cells within memory B cell subsets (Intermediate memory, IM; Resting memory, RM; Activated memory, AM; Tissue-like memory, TLM) of CD38$^-$ (top row) and CD38$^+$ (bottom row) memory B cells is depicted.

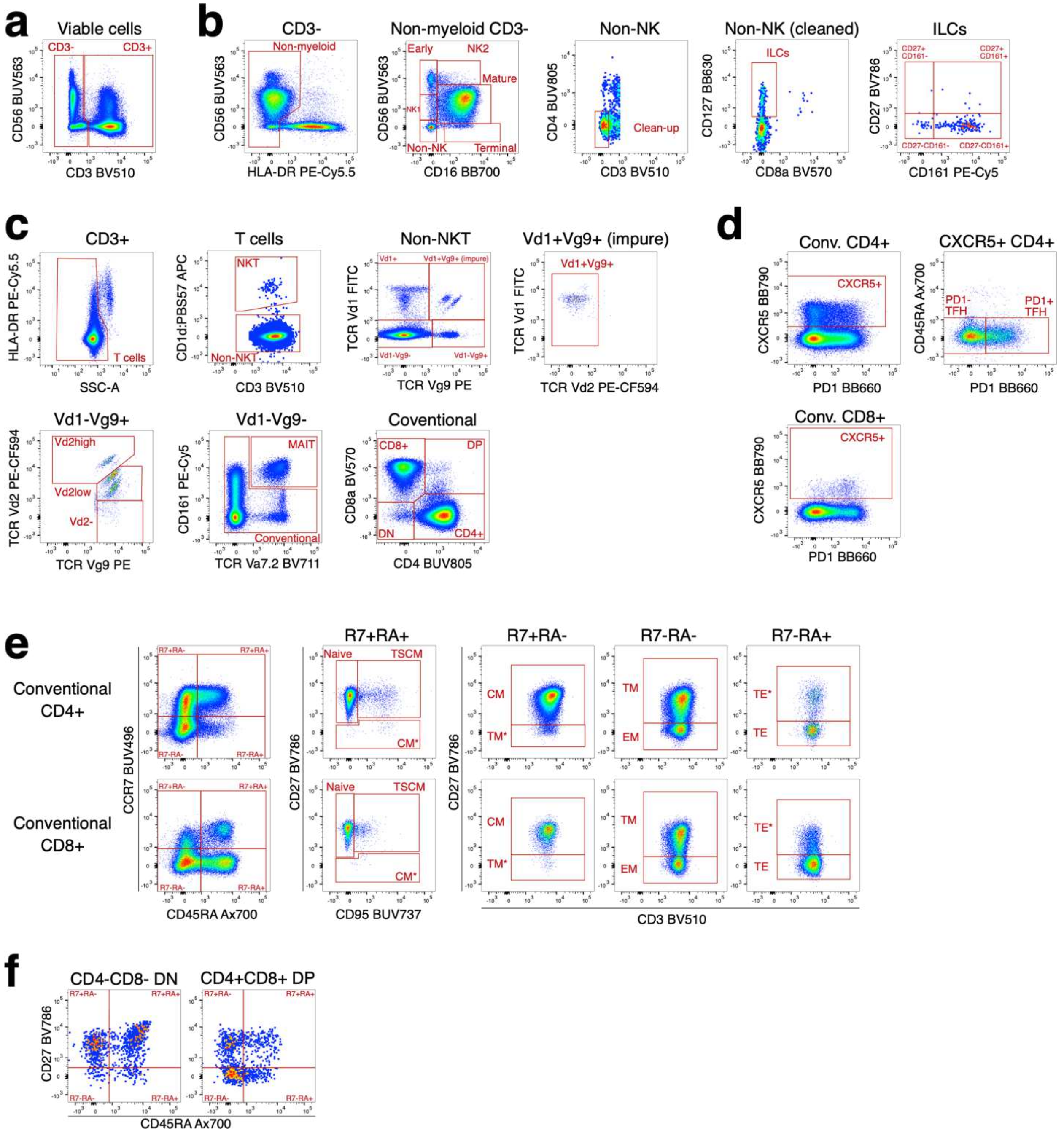

Supplementary Data 3: Gating of innate-like and conventional T cell subsets and NK cells

a) Definition of CD3- and CD3+ cells is shown. **b)** Gating of NK cells and innate lymphoid cells (ILCs) is depicted. HLA-DR expressing cells were excluded prior to defining NK cells based on CD56 and CD16. We further removed residual contaminating cells within CD56$^-$CD16$^-$ cells based on CD4 and CD8 prior to defining CD127 expressing ILCs and subsets of ILCs based on CD27 and CD161 expression. **c)** Definition of unconventional and conventional T cells is shown after excluding residual myeloid cells based on SSC-A and expression of HLA-DR. **d)** Definition of CD4$^+$ and CD8$^+$ T cell memory subsets is depicted. **f)** We further defined subsets from CD4$^-$CD8$^-$ double-negative (DN) and CD4$^+$CD8$^+$ double-positive (DP) T cells based on expression of CD27 and CD45RA.

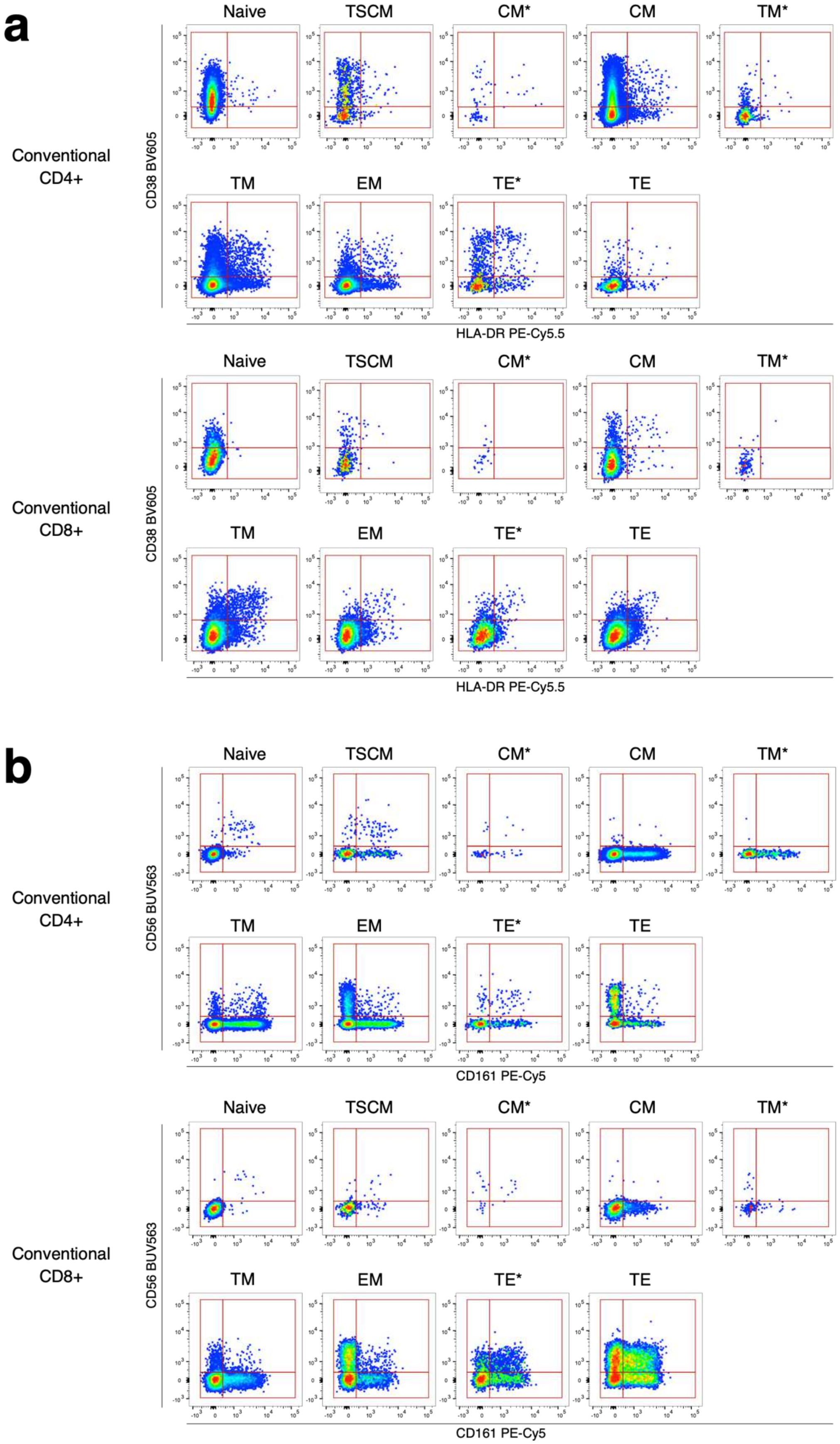
a
Naive
TSCM
CM*
CM
TM*
Conventional CD4+
CD38 BV605
TM
EM
TE*
TE
HLA-DR PE-Cy5.5
Naive
TSCM
CM*
CM
TM*
Conventional CD8+
CD38 BV605
TM
EM
TE*
TE
HLA-DR PE-Cy5.5
b
Naive
TSCM
CM*
CM
TM*
Conventional CD4+
CD56 BUV563
TM
EM
TE*
TE
CD161 PE-Cy5
Naive
TSCM
CM*
CM
TM*
Conventional CD8+
CD56 BUV563
TM
EM
TE*
TE
CD161 PE-Cy5

Supplementary Data 4: Gating conventional T cell subsets based on CD38, HLA-DR, CD56 and CD161

Definition of subsets within conventional CD4$^+$ and CD8$^+$ naïve and memory T cell populations based on **a)** CD38 and HLA-DR or **b)** CD56 and CD161 expression.

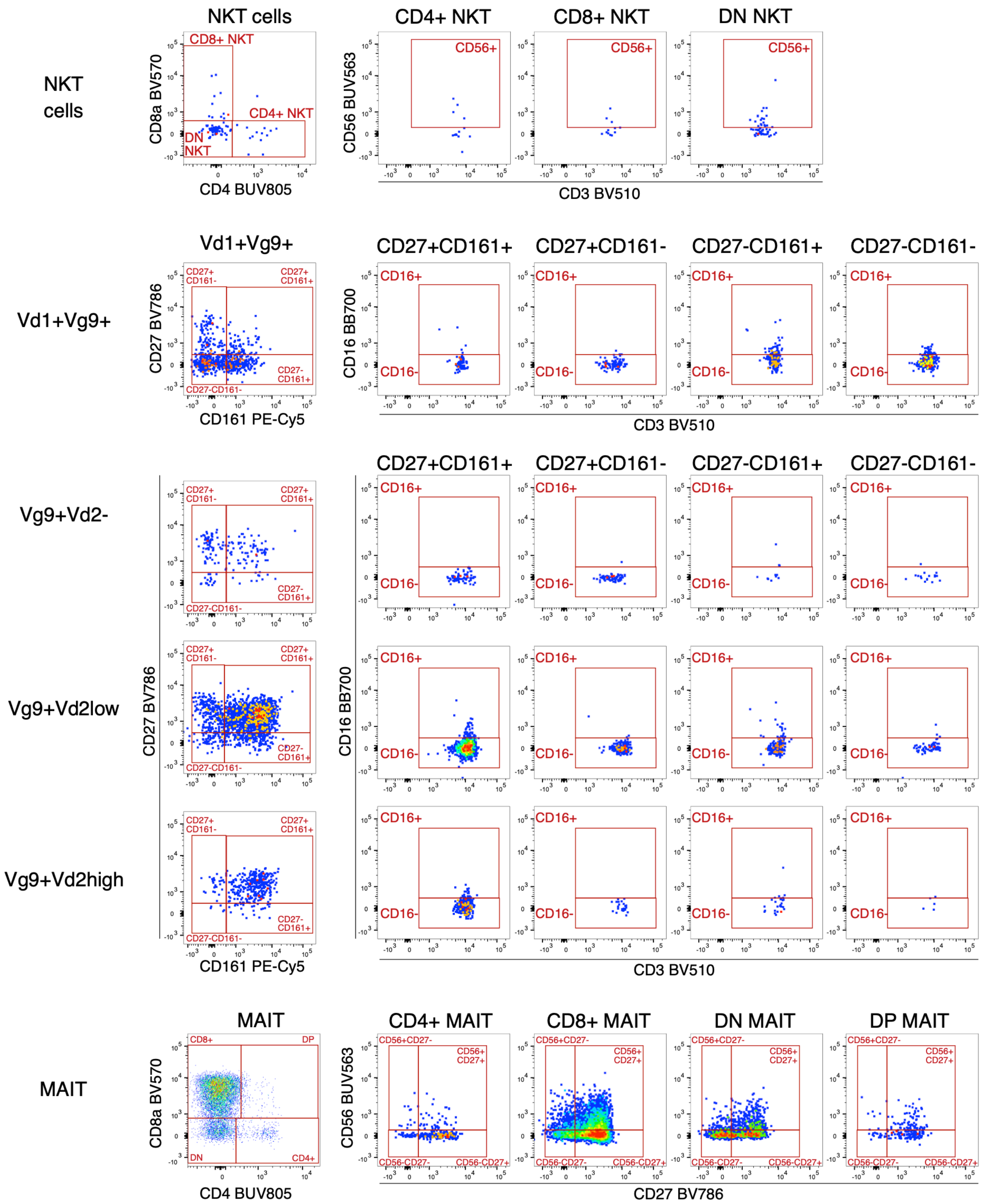

Supplementary Data 5: Gating of several differentiation stages within innate-like T cell subsets

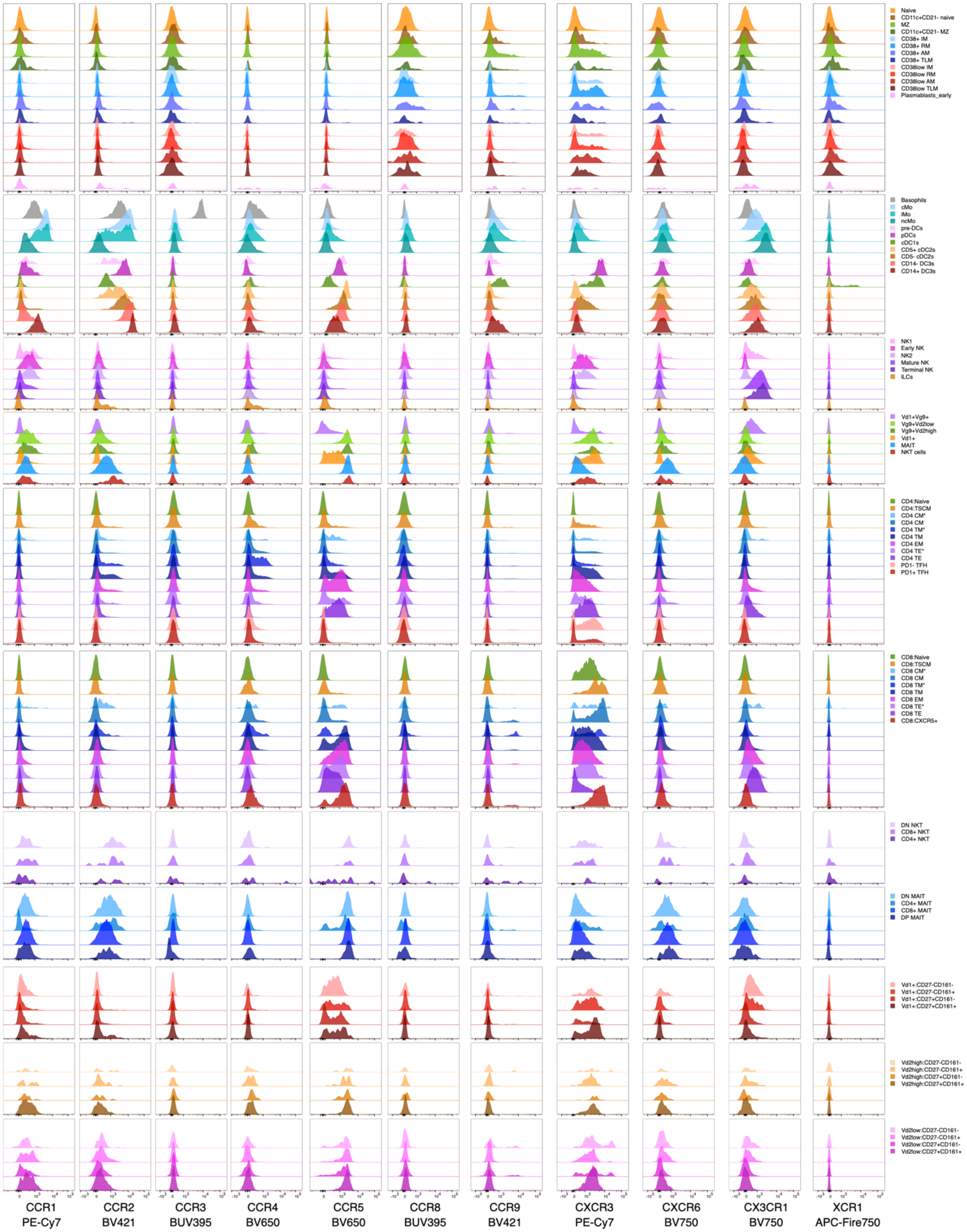
Naive
CD11c+CD21- naive
MZ
CD11c+CD21- MZ
CD38+ IM
CD38+ RM
CD38+ AM
CD38+ TLM
CD38low IM
CD38low RM
CD38low AM
CD38low TLM
Plasmablasts_early
Basophils
cMo
iMo
ncMo
pre-DCs
pDCs
cDC1s
CD5+ cDC2s
CD5- cDC2s
CD14- DC3s
CD14+ DC3s
NK1
Early NK
NK2
Mature NK
Terminal NK
ILCs
Vd1+Vg9+
Vg9+Vd2low
Vg9+Vd2high
Vd1+
MAIT
NKT cells
CD4:Naive
CD4:TSCM
CD4 CM*
CD4 CM
CD4 TM*
CD4 TM
CD4 EM
CD4 TE*
CD4 TE
PD1- TFH
PD1+ TFH
CD8:Naive
CD8:TSCM
CD8 CM*
CD8 CM
CD8 TM*
CD8 TM
CD8 EM
CD8 TE*
CD8 TE
CD8:CXCR5+
DN NKT
CD8+ NKT
CD4+ NKT
DN MAIT
CD4+ MAIT
CD8+ MAIT
DP MAIT
Vd1+:CD27-CD161-
Vd1+:CD27-CD161+
Vd1+:CD27+CD161-
Vd1+:CD27+CD161+
Vd2high:CD27-CD161-
Vd2high:CD27-CD161+
Vd2high:CD27+CD161-
Vd2high:CD27+CD161+
Vd2low:CD27-CD161-
Vd2low:CD27-CD161+
Vd2low:CD27+CD161-
Vd2low:CD27+CD161+
CCR1 PE-Cy7
CCR2 BV421
CCR3 BUV395
CCR4 BV650
CCR5 BV650
CCR8 BUV395
CCR9 BV421
CXCR3 PE-Cy7
CXCR6 BV750
CX3CR1 BV750
XCR1 APC-Fire750

Supplementary Data 6: Expression of chemokine receptors

Shown is the expression of chemokine receptors on all main lineages/immune subsets as overlaid histograms. Data derives from one healthy donor.

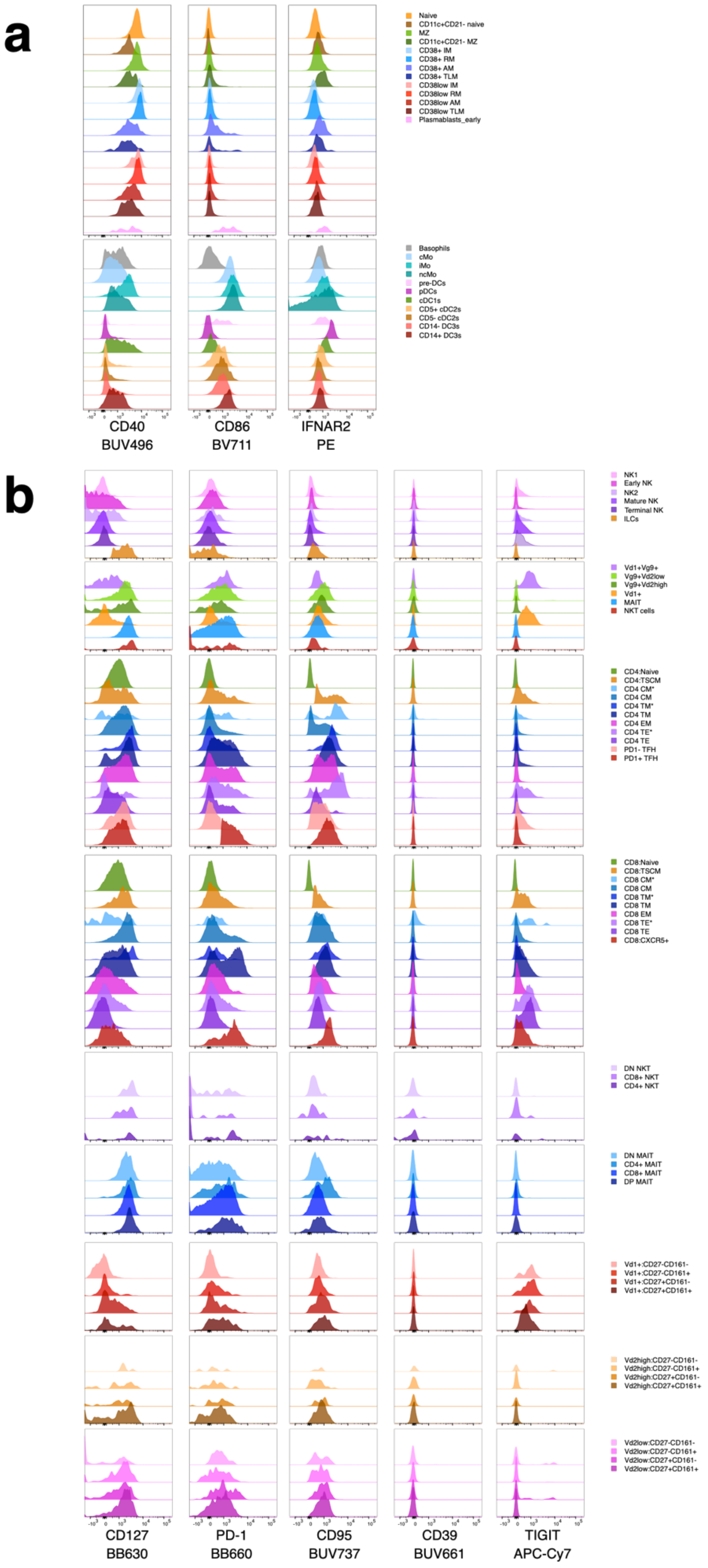
a
Naive
CD11c+CD21- naive
MZ
CD11c+CD21- MZ
CD38+ IM
CD38+ RM
CD38+ AM
CD38+ TLM
CD38low IM
CD38low RM
CD38low AM
CD38low TLM
Plasmablasts_early
Basophils
cMo
iMo
ncMo
pre-DCs
pDCs
cDC1s
CD5+ cDC2s
CD5- cDC2s
CD14- DC3s
CD14+ DC3s
CD40
BUV496
CD86
BV711
IFNAR2
PE
b
NK1
Early NK
NK2
Mature NK
Terminal NK
ILCs
Vd1+Vg9+
Vg9+Vd2low
Vg9+Vd2high
Vd1+
MAIT
NKT cells
CD4:Naive
CD4:TSCM
CD4 CM*
CD4 CM
CD4 TM*
CD4 TM
CD4 EM
CD4 TE*
CD4 TE
PD1- TFH
PD1+ TFH
CD8:Naive
CD8:TSCM
CD8 CM*
CD8 CM
CD8 TM*
CD8 TM
CD8 EM
CD8 TE*
CD8 TE
CD8:CXCR5+
DN NKT
CD8+ NKT
CD4+ NKT
DN MAIT
CD4+ MAIT
CD8+ MAIT
DP MAIT
Vd1+:CD27-CD161-
Vd1+:CD27-CD161+
Vd1+:CD27+CD161-
Vd1+:CD27+CD161+
Vd2high:CD27-CD161-
Vd2high:CD27-CD161+
Vd2high:CD27+CD161-
Vd2high:CD27+CD161+
Vd2low:CD27-CD161-
Vd2low:CD27-CD161+
Vd2low:CD27+CD161-
Vd2low:CD27+CD161+
CD127
BB630
PD-1
BB660
CD95
BUV737
CD39
BUV661
TIGIT
APC-Cy7

Supplementary Data 7: Expression of functional receptors

Shown is the expression of functional receptors on main lineages/immune subsets as overlaid histograms. Markers are panel specific. Markers only measured with the **a)** B cell/myeloid cell or **b)** T cell/NK cell panel backbone are shown as highlighted in supplementary table 2. Data derives from one healthy donor.

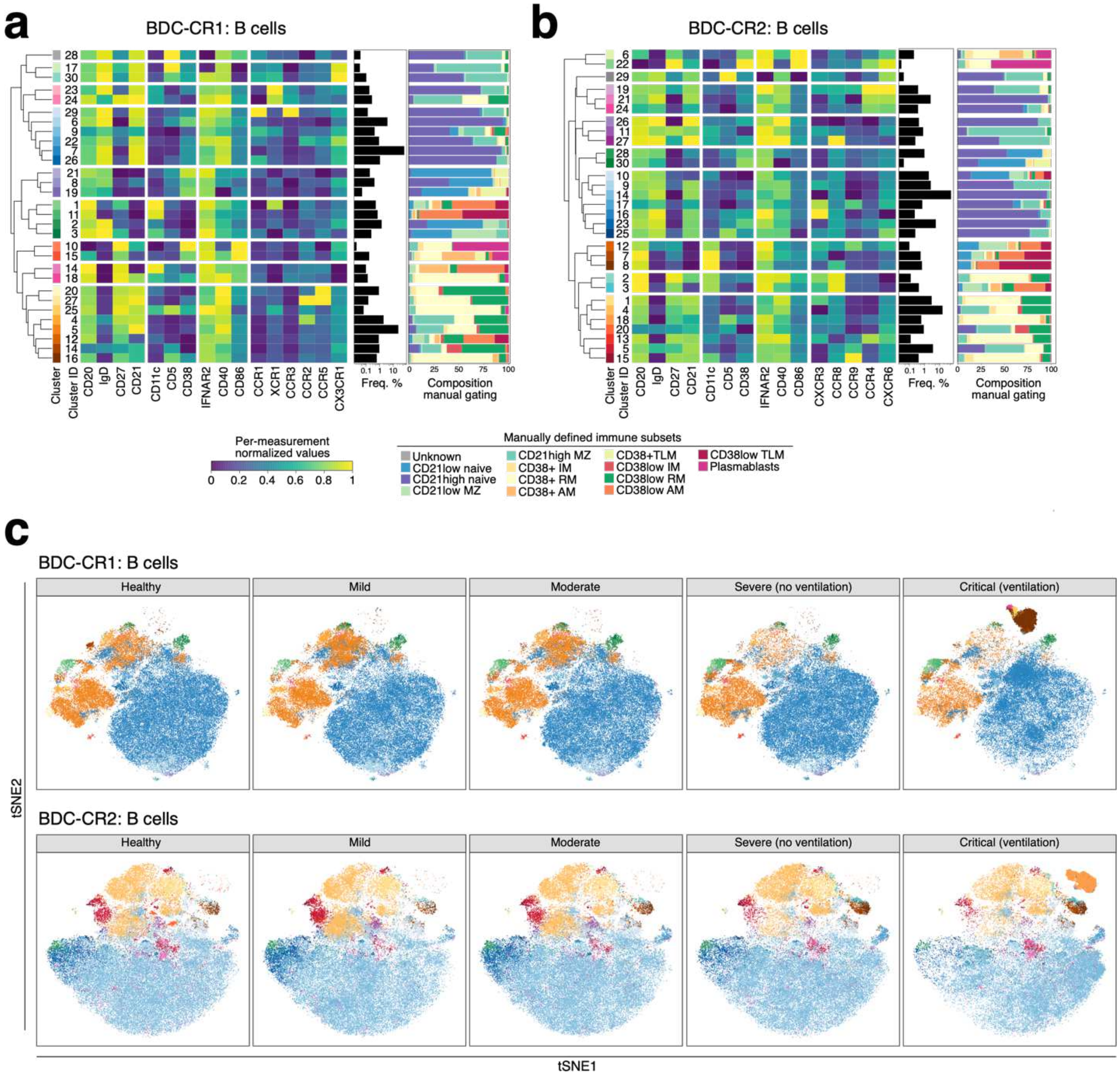

Supplementary Data 8: FlowSOM analysis for B cells

Heatmaps show per-measurement normalized median fluorescence intensity based on trimmed 1-99% percentile values for each FlowSOM cluster (rows). Only markers included in clustering (columns) are sown. Bar on left shows coloring of each FlowSOM cluster and FlowSOM clusters were clustered based on similarity of MFI values using hierarchical clustering (indicated by dendrogram and gap between rows). Bar graph in the middle shows the frequency of each cluster and bar graph on the right the composition of each cluster based on manual gating annotation. Heatmaps for panels **a)** CR1 and **b)** CR2 are shown. **c)** tSNE plots for CR1 (top) and CR2 (bottom) panel are shown delineated based on COVID-19 severity group. Dots are colored based on FlowSOM cluster annotation. Each tSNE plot contains 50’000 randomly subsampled cells and not equally distributed across each individual sample.

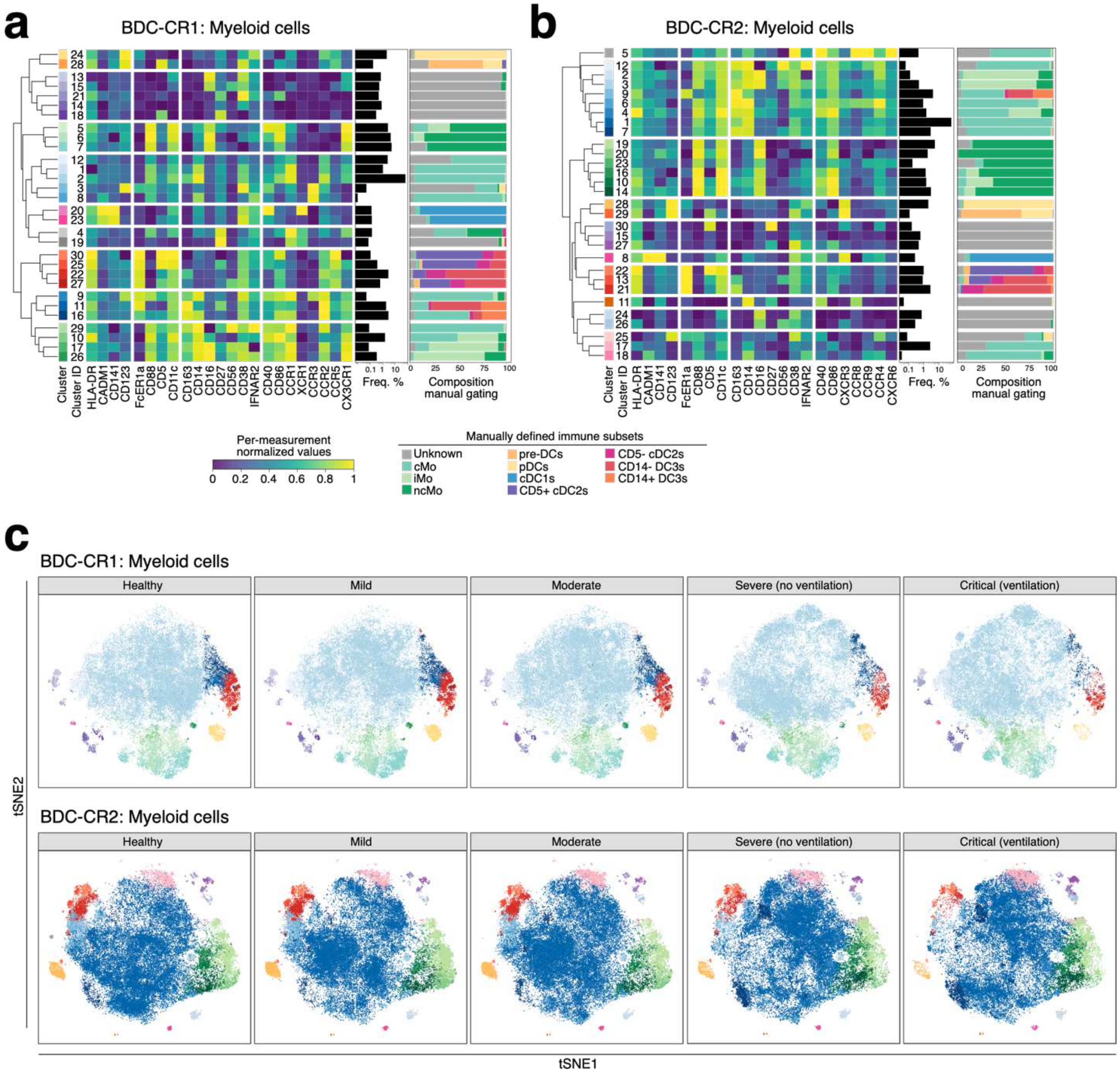

Supplementary Data 9: FlowSOM analysis for myeloid cells

Same as Supplementary Data 8.

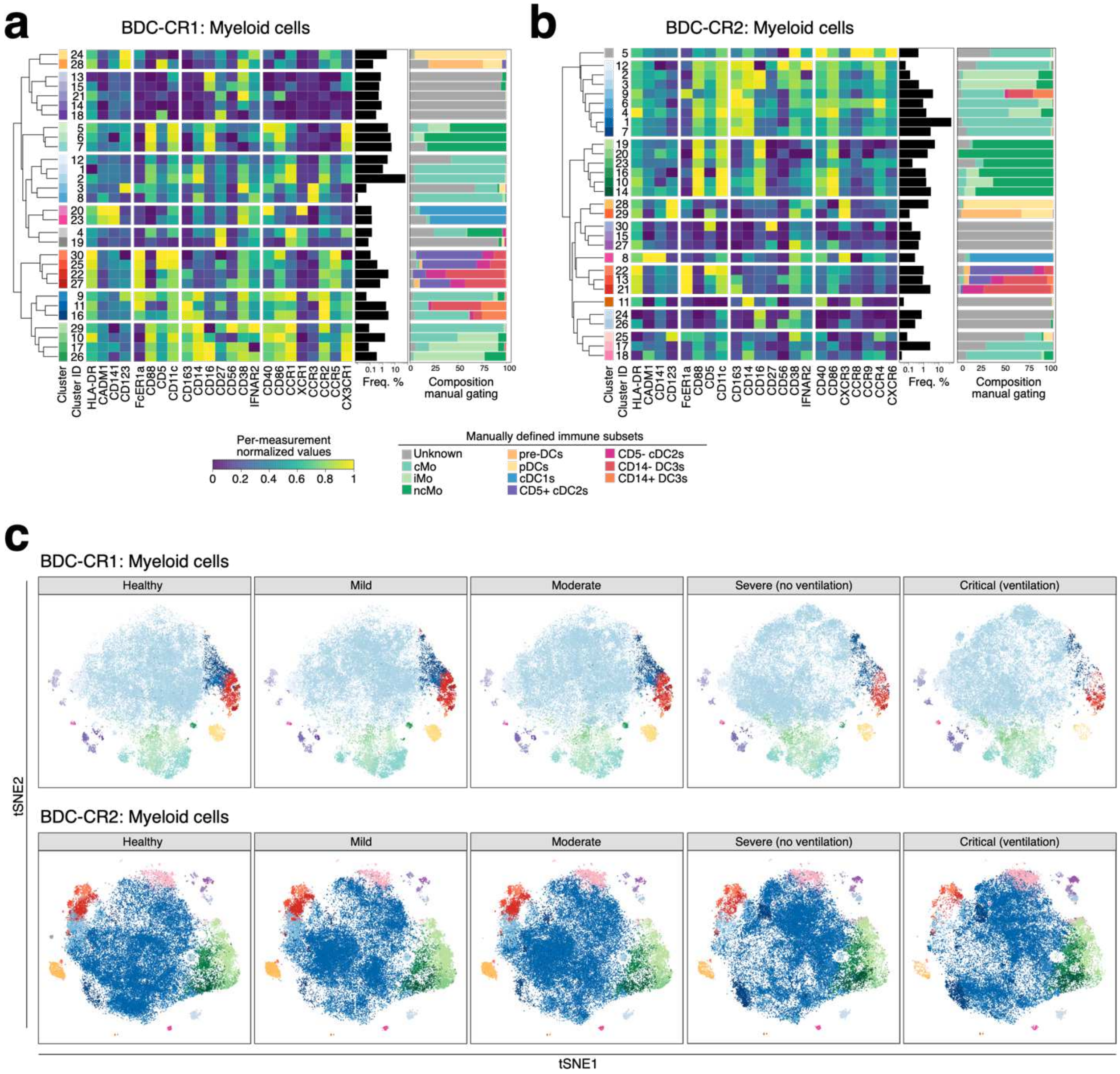

Supplementary Data 10: FlowSOM analysis for CD4 T cells

Same as Supplementary Data 8.

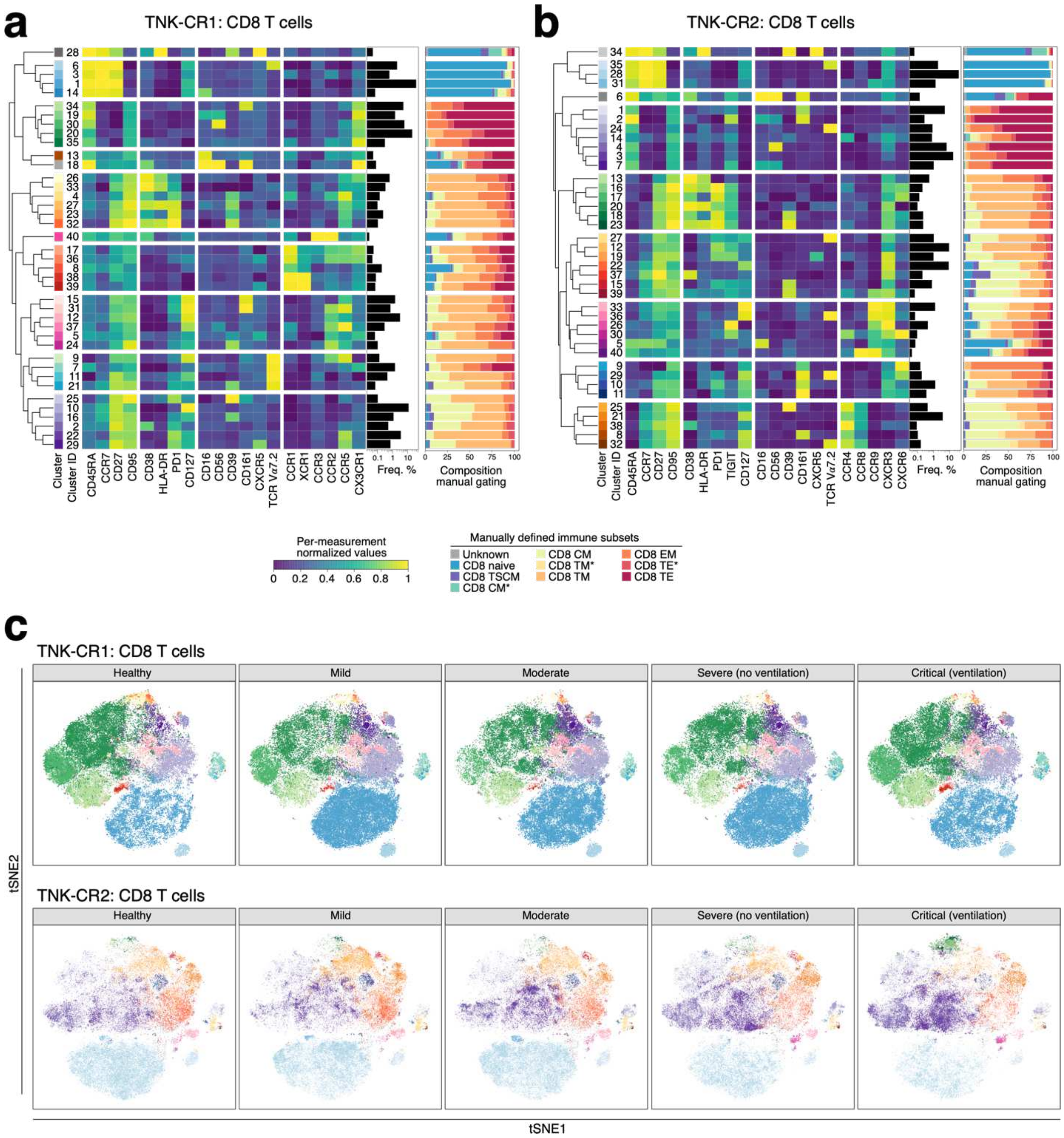

Supplementary Data 11: FlowSOM analysis for CD8 T cells

Same as Supplementary Data 8.

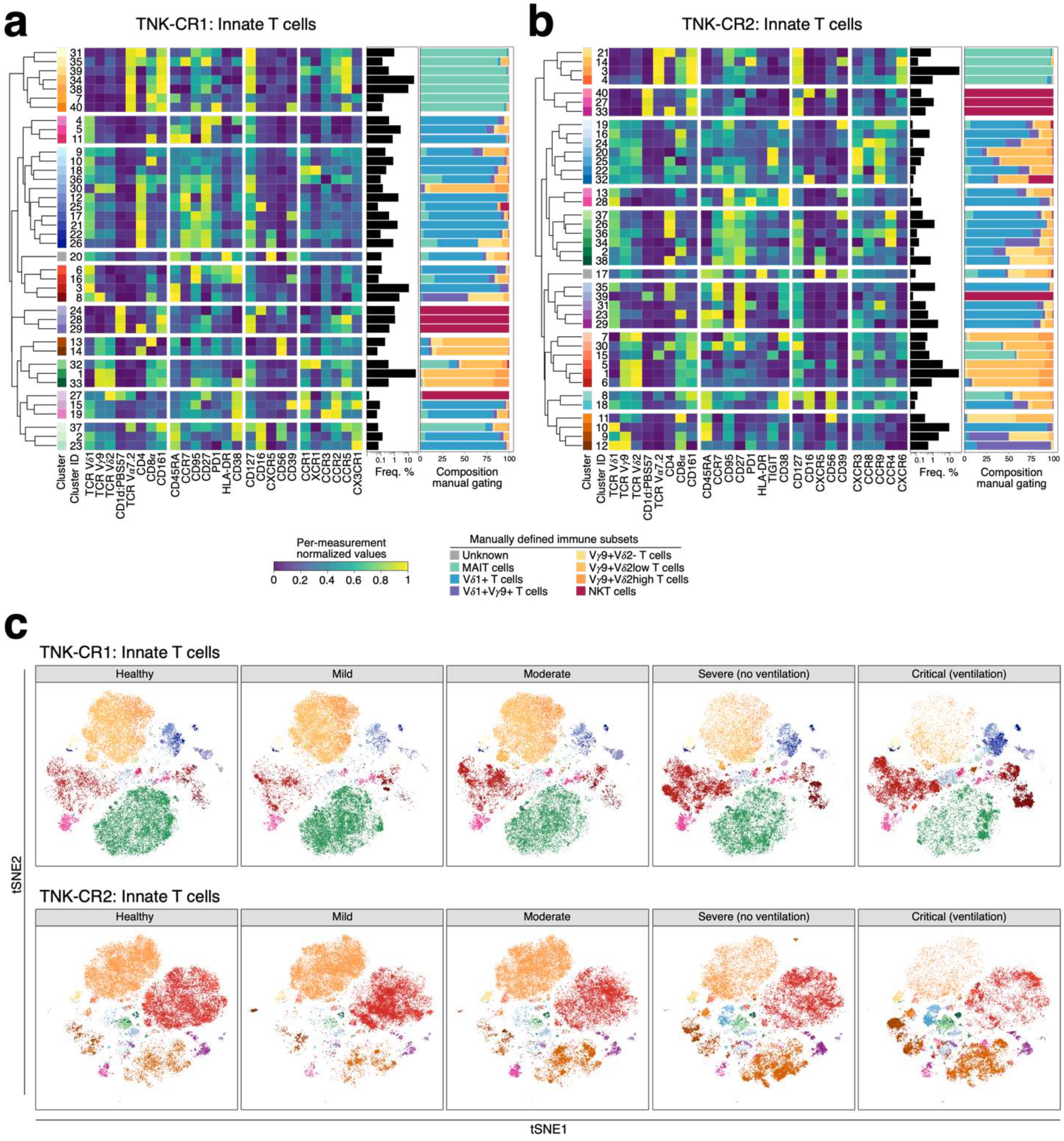

Supplementary Data 12: FlowSOM analysis for innate-like T cells

Same as Supplementary Data 8. From each group 27583 cells were included for tSNE computation.

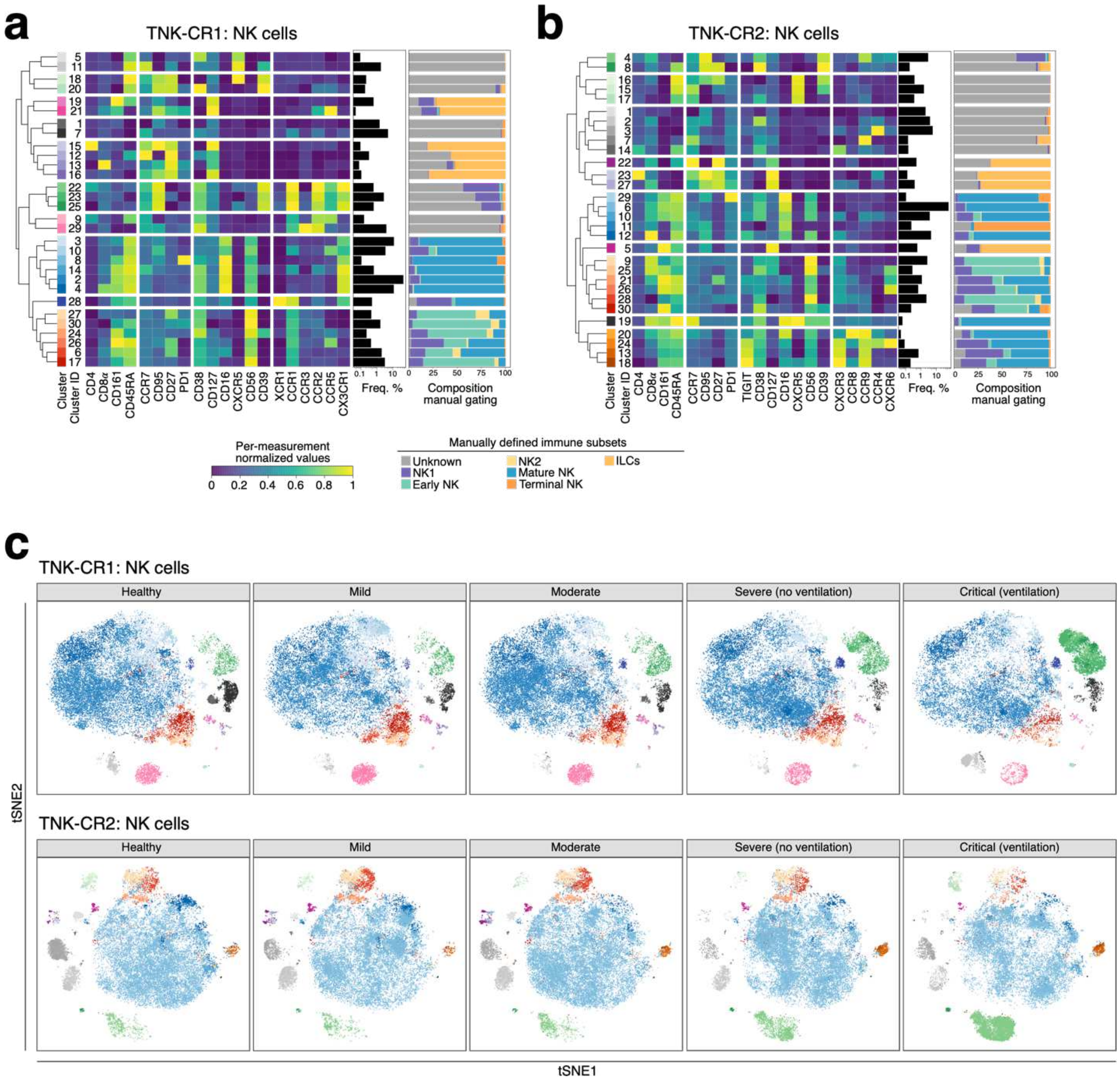

Supplementary Data 13: FlowSOM analysis for NK cells

Same as Supplementary Data 8. From each group 25000 cells were included for tSNE computation.

Supplementary Files

This is a list of supplementary files associated with this preprint. Click to download.

- 220218Supplementarytables.pdf